Doctoral dissertation
Prepared in the Institute of Physics
of the Jagiellonian University
Submitted to the Faculty of Physics,
Astronomy and Applied Computer Science
of the Jagiellonian University

Double-strip prototype of polymer time-of-flight positron emission tomograph based on multi-level analog electronics

Szymon Witold Niedźwiecki

Supervised by:
prof. dr hab. Paweł Moskal

Cracow, 2019

ABSTRACT

The aim of this work was to construct and perform tests of a prototype Positron Emission Tomography (PET) scanner consisting of two detection modules. Each module consisted of a long plastic scintillator strip and was read-out from both sides by fast vacuum tube photomultipliers. Two dimensions of strips were tested: 5 x 19 x 300 mm^3 and 7 x 19 x 500 mm^3. It was shown, that one can successfully utilise plastic scintillators for 511 keV gamma quanta registration and determination of e^+e^- annihilation position.

The research presented in this thesis was conducted in the framework of the J-PET collaboration, whose aim is the elaboration of the cost-effective method for construction of total-body PET.

In the course of this work a R9800 Hamamatsu photomultiplier is selected for the first prototype of the total-body J-PET scanner and a multi-threshold constant threshold board design is decided to be used for time of interaction and energy loss measurement. An optimisation method of detector parameters: voltage supplied and threshold for front end-boards is provided.

The main comparison with commercial scanners was performed for a 30 cm long prototype. The fractional energy resolution is determined to be 9% at 340 keV - which is equal to the Compton edge for 511 keV gamma quanta. The Coincidence Resolving Time (CRT) is determined to be 280 ps and Point Spread Function (PSF) at 1 cm off the center of tested prototype was equal to 9.8 mm and 6.7 mm for transaxial and axial resolutions, respectively.

Result of this thesis constituted the basis for the project of the full scale prototype with diamater of 85 cm and axial field of view of 50 cm. The author of this thesis was taking part in the costruction of the first full scale whole-body prototype from the stage of mechanical assembly to assistance in performing measurements similiar to the ones as described in the thesis.

STRESZCZENIE

Celem tej pracy było skonstruowanie i wykonanie testów prototypu skanera PET składającego się z dwóch modułów detekcyjnych. Każdy z modułów zbudowany był z długich plastikowych pasków scyntylacyjnych oraz odczytywany był z dwóch stron za pomocą szybkich fotopowielaczy próżniowych. Zostały przetestowane dwa wymiary pasków: 5 x 19 x 300 mm^3 oraz 7 x 19 x 500 mm^3. Zostało pokazane, że można z sukcesem wykorzystać scyntylatory plastikowe do detekcji kwantów gamma o energii 511 keV oraz wyznaczenia miejsca anihilacji e^+e^-.

Badania przedstawione w tej dysertacji wykonane zostały w ramach pracy w zespole badawczym J-PET, której celem jest opracowanie metody na budowę opłacalnego skanera PET pozwalającego na badanie całego ciała pacjenta.

W pracy, do konstrukcji prototypu skanera J-PET na całe ciało, zostaje wybrany fotopowielacz R9800 firmy Hamamatsu oraz projekt wielo-poziomowej, stało progowej płyty do wyznaczenia czasu oddziaływania i pomiaru strat energii. Zostały również przedstawione metody optymalizacji parametrów detektora: napięcia zasilania oraz progów dla płyt odczytu.

Główne porównanie z komercyjnymi skanerami, zostało wykonane dla prototypu o długości 30 cm. Rozdzielczość energetyczna wyniosła 9% dla 340 keV - to jest dla energii odpowiadającej zboczu Comptona dla kwantów gamma o energii 511 keV. Rozdzielczość czasowa (z ang. CRT) została ustalona na 280 ps, a rozdzielczość przestrzenna (z ang. PSF) w 1 cm poza centrum testowanego prototypu, wyniosła 9.8 mm i 6.7 mm dla odpowiednio rozdzielczości poprzecznej do osi detektora i osiowej.

Wyniko tej pracy były podstawą do zaprojektowania prototypu tomograpu J-PET o średnicy pola obrazowania wynoszącej 85 cm i szerokości 50 cm. Autor pracy brał udział w konstrukcji prototypu na całe ciało od etapu montażu do pomiarów podobnych do opisanych w tej pracy.

ACKNOWLEDGEMENTS

During my long journey for PhD I had extraordinary luck to encounter many experienced and patient colleagues who helped me with both perfroming research and teaching how to do things properly. Without this support and encouragement this thesis would not be completed. I would like to thank everyone whom I worked with for the time they have spent with me and for the unending stream of remarks they gave me everyday.

First I would like to give my deepest gratitude and appreciation to Professor Paweł Moskal, supervisor of both my PhD and Master theses. I started my adventure with J-PET thanks to Him just after third year of studies. It is mainly due to his extraordinary teaching talents and patience that I managed to finish my task.

I am grateful to Professor Bogusław Kamys for allowing me to join research under the wing of Nuclear Physics Department and to Professors: Lucjan Jarczyk, Andrzej Magiera, Janusz Brzychczyk, Jerzy Smyrski, Kazimierz Bodek, Zbigniew Rudy, Tomasz Kozik, Piotr Salabura and Piotr Białas for unrelenting storm of remarks and questions which always showed me that there is more to learn and to know.

I want to also give thanks to the current and former members of the J-PET group: Eryk Czerwiński, Michał Silarsi, Marcin Zieliński, Alek Gajos, Neha Gupta-Sharma, Łukasz Kapłon, Sushil Sharma, Wojciech Krzemień, Dominika Alfs, Shivani, Kamil Dulski, Daria Kamińska, Ewelina Kubicz, Muhsin Mohammed, Juhi Raj, Oleksandr Rundel, Bartosz Głowacz, Teresa Gucwa-Ryś, Izabela Pytko, Michał Smolis, Sławomir Tadeja, Tomasz Twaróg, Anna Wieczorek, Jarosław Zdebik and Natalia Zoń, Bożena Jasińska, Bożena Zgardzińska, Marek Gorgol and Konrad Wysogląd, Iryna Ozierianska, Wojciech Migdał and Bartłomiej Korzeniak. It was a pleasure to work in such big and diverse group. Thank you for the great atmosphere during lab work, official and unofficial meetings.

A lot of thanks to Kacper Topolnicki and Magda Skurzok for asking, when I will finish my thesis and for always going for coffee with me when I needed it.

Andrzej Kaczmarski and Janusz Konarski - thank you for all the talks we have had during first laboratory classes.

Grzegorz Korcyl spend infinite amount of hours with me testing different front-end boards in electronic laboratory, it is thanks to him that I somehow can tell apart the input channels from output ones.

Many thanks to Krzysztof Kacprzak for sharing flat, scientific curiosity and a cat with me.

Tomasz Bednarski helped me a lot during both PhD and Master studies, his friendship and encouragements gave me a lot of determination to move forward, especially, when nothing seemed to work in laboratory.

I thank my friends from PhD studies, especially Grzegorz Rut, Karol Dąbrowski, Dawid Dul and Maciej Majka for always having the time to listen to my nagging when I was depressed.

Dziękuję bardzo ukochanym rodzicom, byliście pierwszymi, którzy uwierzyli w mój sukces i nic nie potrafiło was z tej wiary wybić. Bez waszego wsparcia nie udałoby mi się dotrzeć tu gdzie jestem.

Last, but not least I would like to express my thanks to my wife Monika for being able to stay with me despite my prolonged stays at J-PET laboratories and weird sense of humor and to my son Filip for sharing with me unlimited cheerfullness and optimism. I love you both from the bottom of my heart.

Even if I omitted someone I still hold a lot of gratitude to all of You.

DECLARATION

Wydział Fizyki, Astronomii i Informatyki Stosowanej
Uniwersytet Jagielloński

Oświadczenie

Ja niżej podpisany Szymon Witold Niedźwiecki, doktorant Wydziału Fizyki Astronomii i Informatyki Stosowanej Uniwersytetu Jagiellońskiego, oświadczam, że przedłożona przeze mnie rozprawa doktorska pt. "Double-strip prototype of polymer time-of-flight positron emission tomograph based on multi-level analog electronics" jest oryginalna i przedstawia wyniki badań wykonanych przeze mnie osobiście, pod kierunkiem prof. dr. hab. Pawła Moskala. Pracę napisałem samodzielnie.

Oświadczam, że moja rozprawa doktorska została opracowana zgodnie z Ustawą o prawie autorskim i prawach pokrewnych z dnia 4 lutego 1994 r. (Dziennik Ustaw 1994 nr 24 poz. 83 wraz z późniejszymi zmianami).

Jestem świadom, że niezgodność niniejszego oświadczenia z prawdą ujawniona w dowolnym czasie, niezależnie od skutków prawnych wynikających z ww. ustawy, może spowodować unieważnienie stopnia nabytego na podstawie tej rozprawy.

Kraków, dnia ....

CONTENTS

1 INTRODUCTION 15

I STATE OF THE ART OF PET 19
2 PET PERFORMANCE CHARACTERISTICS 21
3 TIME OF FLIGHT METHOD 26

II JAGIELLONIAN PET 29
4 GENERAL CONCEPT 31
5 FIGURE OF MERIT 35
6 SCATTER FRACTION 37

III J-PET DOUBLE STRIP PROTOTYPE 43
7 SCINTILLATORS 47
8 PHOTOMULTIPLIERS 49
9 RADIOACTIVE SOURCES AND COLLIMATOR 51
10 SERIAL DATA ANALYSER 56
11 EXPERIMENTAL SETUP 58
12 J-PET FRAMEWORK SOFTWARE 61

IV DATA ANALYSIS 63
13 PEDESTAL VALUE CALCULATION 65
14 CHARGE CALCULATION 68
15 ENERGY DEPOSITION 70
16 TIME AT THRESHOLD ESTIMATION 75
17 TIME OVER THRESHOLD 75
18 CONVERSION FROM THE TIME TO THE VOLTAGE DOMAIN 82

V TIME AND CHARGE MEASUREMENT METHODS . . . 85
19 MULTI-LEVEL CONSTANT FRACTION BOARD PROTOTYPE 89
20 MULTI-LEVEL CONSTANT THRESHOLD BOARD PROTOTYPES 91

VI OPTIMISATION OF THE J-PET PARAMETERS 95
21 THRESHOLD OPTIMISATION AT THE CENTER POSITION 97
22 OPTIMISATION OF SUPPLY VOLTAGE 99
23 IMPACT OF ENERGY DEPOSITION ON TIME RESOLUTION 103

VII TIME CALIBRATION 105
24 TIME OFFSET 107
25 TOF OFFSET 108
26 WALK EFFECT 110
26.1 Time walk correction based on charge 110

26.2 Time walk correction based on TOT 112

VIII IMAGE RECONSTRUCTION 115
27 HIT POSITION ESTIMATION 117
28 NAIVE RECONSTRUCTION 119
29 MLEM ALGORITHM 123
30 MLEM ITERATION STUDIES 125

IX RESULTS FOR DIFFERENT SCINTILLATOR LENGTHS 127
31 ENERGY RESOLUTION 131
32 COINCIDENCE RESOLVING TIME 133
33 POINT SPREAD FUNCTION 135

X COMPARISON TO COMMERCIAL SCANNERS 137
34 SUMMARY AND PERSPECTIVES 141

ACRONYMS

AFOV Axial Field Of View

ASIC Application-Specific Integrated Circuits

CRT Coincidence Resolving Time

CT Computed Tomography

FDG Fludeoxyglucose (^{18}F)

FOM Figure Of Merit

FOV Field Of View

FPGA Field-Programmable Gate Arrays

J-PET Jagiellonian PET

LOR Line Of Response

MR Magnetic Resonance

MLEM Maximum Likelihood Expectation Maximization

PET Positron Emission Tomography

PSF Point Spread Function

SDA Serial Data Analyser

SiPM Silicon Photomultiplier

TOF Time of Flight

TOF-PET Time of Flight PET

TOT Time Over Threshold

TRB Trigger Readout Board

TTS Transit Time Spread

1

INTRODUCTION

PET scanners have come a long way from one of the first prototypes, built in 1975 [1] to the current state of the art devices.

First scanners consisted of crystals gathered together in hexagonal arrays. Their output was analysed by invidual sets of electronic systems which provided information about signal amplitude in a given coincidence window. For image reconstruction a fast Fourier transform was used [2]. Through thirthy years of developement, a lot of crucial improvements were introduced, which enabled the improvement of the spatial resolution of scanners from 1.2 cm [2] to even 1.4 mm [3]. Such an improvement was possible with the usage of the Time of Flight (TOF) method [4], continuous developement of reconstruction algorithms [5, 6] and the application of new front end electronics such as Application-Specific Integrated Circuits (ASIC) [7] or Field-Programmable Gate Arrays (FPGA) [8].

Main goal of PET measurements is to find where a radioative substance, radiopharmaceutical, injected into patients body is accumulated. Since the radiopharmaceutical is $\beta+$ radioactive, positrons are being produced from accumulation places. In case of the human body the positron can travel a few milimeters [9], during which it is interacting with electrons and after slowing down either annihilates with the electrons producing at least two gamma quanta or forms positronium - an unstable bound state similiar to the hydrogen atom [10]. Since both electron-positron annihilation and positrionium decay occur almost at rest, the total energy available to the decay products is equal to twice the electron mass. In the case of two gamma quanta production, each of them has 511 keV.

A variety of possible radiopharmaceuticals give opportunities to monitor different biological functions of the examined subject. Most commonly, PET scanners are used for seeking tumor cells and monitoring tumor relapses [11].

PET provides a functional (metabolic) image of process selected by a proper marker. The information is complementary to the data obtained from Computed Tomography (CT) and Magnetic Resonance (MR) scanners. These two techniques (CT, MR) produce structural and morphological images, giving insight into placement of tissues, bones etc. inside the patients body, they do not provide information about metabolic activity.

One of the challenges in the PET tomography is the simultaneous imaging of the whole human body. Scanners capable of performing such a task, called total-body PETs [12], are still under developement. Due to the high cost of crystal scintillators, a commercial production of the commonly available total-body scanner based on crystals seems implausible. Currently only about 20 cm along the body can be simultanousely examined at single bed position [4]. In the case of a whole-body scan, several overlapping bed positions are necessary. Currently only 1% of γ quanta emitted from patien's body are collected [13]. The extension of the scanned part from around 20 cm to 200 cm would improve the sensitivity and signal-to-noise ratio. The radiation dose needed for a whole body scan can be also reduced and the usage of shorter living tracers will be simplified. To address this problem several different designs of total-body scanners were introduced, their design based on detection by resistive plate chambers (RPCs) [14], straw tubes [15, 16] and crystal scintillators [13].

The aim of this work was to construct a PET scanner prototype, consisting of detection modules with a much larger Field Of View (FOV), built out of less expensive materials based on the ideas described in [17]. Each module consists of a plastic scintillator strip covered with reflective foil and a light tight material. To each of its end a photomutliplier is connected via optical gel. To reconstruct an annihilation event inside the scanner one needs to register two gamma quanta originating from the electron-positron annihilation. The smallest version of a PET scanner thus consists of two detection modules laying on a single plain and parallel to each other. In this work studies of the performance of such a scanner version are performed. The characteristics such as, TOF resolution and spatial resolution, for a point like source placed in the middle of scanner FOV will be determined.

In nuclear and particle physics time resolution is usually expressed as the single standard deviation value (σ) of the TOF spectrum. In literature [4] concerning a PET scanners, a Coincidence Resolving Time (CRT), defined as the full width at half maximum of the time difference distribution, is used. Therefore the CRT value of TOF will be used in this work as a way of expressing scanner time resolution.

In the first part of this thesis, a brief desription of modern scanners is provided along with a comparison to the new approach, which uses different scintillating material and annihilation place reconstruction method. The second part presents the Jagiellonian PET (J-PET) scanner, starting from the general concept and going through its estimated performance.

Both of the aforementioned parts are based on literature studies performed by the author. The discussion of gamma quantum with 511 keV scattering in scintillator is based on Monte-Carlo simulations performed by the author.

The third part describes a two strip prototype of J-PET, its components, the experimental setup and measurements performed to determine the spatial and time resolution of the scanner, as well as short introduction to the chain of data processing. The selection of elements for the two strip prototype was done in the scope of working with J-PET group, author took active part in all measurements, mechanical assembly of equipment and decisions on the final version of the experimental setup.

In the fourth part, a data analysis is presented. Beginning at low level, with raw acquired, fully sampled signals from photomultipliers and ending with conversion of signals to the voltage domain. Data analysis was written in the C++ language by the author using J-PET Framewrok architecture [18].

The fifth part contains considerations and tests of two possible approaches to the multi-threshold measurement of time: constant fraction and constant thresholds. Capabilities of each of the tested boards are discussed and a final decision on the type of design is presented. The measurements were performed in cooperation with board designers as well as colleagues from the J-PET group responsible for the data acquisition system [19].

The sixth part shows how one can optimise J-PET parameters such as the voltage supplied to the photomultipliers and the threshold on which time should be measured.

The seventh and eight parts contain methods for determination of time calibration, the hit position along detection modules, the annihilation position and obtain the image reconstruction.

In the ninth part results for different scintillator lengths are compared to simulated ones.

The four beforementioned parts contain an analysis of data performed by the author of the thesis, based on the measurements from part three.

Finally in the tenth part, a comparison of the performance of the two strip prototype with commercial scanners is presented. Their energy, time and spatial resolutions are provided. The comparison is based on data obtained in previous parts and literature studies performed by the author.

This work ends with a summary and perspectives on how to progress with the project into the stage of full body scanner.

Part I

STATE OF THE ART OF PET

2

PET PERFORMANCE CHARACTERISTICS

Many cancer diseases can currently be treated much more effectively if the disease is detected at the initial stage. To perform such detection one needs a noninvasive examination method, capable of pinpointing diseased locations with very high accurancy. The PET scanner arose from this need and since the goal of scanning whole body at once is not yet acomplished, its technology is still being developed [1].

In principle to detect cancerous cells one has to know how do they differ from normal body cells. The difference which has been exploited in cancer diagnosis, is that cancer cells need much more energy due to their faster growth rate [20]. This implies that regions of higher glucose uptake can correspond to clusters of cancerous cells. To trace such places a radioactive marker, radiopharmaceutical, is injected into the patients body - in most cases Fludeoxyglucose (^{18}F) (FDG), labeled with ^{18}F isotopes connected to it. There are many other markers, each used to monitor different metabolical changes inside human body [21, 22].

The connected isotope is $\beta+$ radioactive. This means that during its decay, a positrion is ejected. The kinetic energy of the positron upon its production is larger than zero. After it tranverses through the matter for few mm it slows down and may annihilate with the electrons from the body of the patient. The most probable is the annihilation into a pair of gamma rays and this phenomenon is the one used in PET tomography.

By injecting the patient with a radioactive marker and detecting pairs of gamma quanta, one is able to find the location of the annihilation. This in turn, is relatively close to the place of $\beta+$ decay and the discrepancy between those two places is a natural limitation of PET scan resolution.

A typical markers, radioactive isotopes used with them and mean free paths of positrions in matter are presented in Tabs. 1 and 2. Beacause of fairly low half-times of most isotopes the time needed for production of radiopharmaceutiacals and the whole examination has to be as short as possible.

To detect gamma quanta, crystal scintillators are currently used. Their high density and high atomic (Z) number result in very high

1 At the stage of completion of this thesis a first generation total-body PET scanner from crystals is still under construction [12, 13]

Table 1: Radioactive markers used in PET scans and information about their $\beta+$ emitting isotopes [23].

Radiopharmaceutical	Isotope	Half lifetime [min.]	Average / Max range of positron in water [mm]
^{18}F-FDG	^{18}F	110	0.46 / 2.2
^{11}C-palmitate	^{11}C	20.4	0.85 / 3.8
$^{13}NH_3$	^{13}N	10	1.15 / 5.0
$C^{15}O$	^{15}O	2	1.80 / 8.0

Table 2: Comparison of usage of radioactive markers for examination of different diseases [23].

Radiopharmaceutical	Imaging purpose
^{18}F-FDG	Metabolism in the brain and heart
^{11}C-palmitate	Myocardial metabolic
$^{13}NH_3$	Myocardial perfusion
$C^{15}O$	Pulmonary and cardiac malfunctions

probability of detection. Crystals are cut into small pieces, few by few milimiters, and formed in an array. The front of each array is pointed at the examined patients body. A few photomultipliers are connected to the back of each array (see Fig. 1). Such a configuration is currently applied in most of PET scanners used in hospitals [24, 25]. Recently a new solution with Silicon Photomultiplier (SiPM) read-out was developed, where a dense matrix of small photomultipliers is connected to scintillation crystals (see Fig. 2) [24] .

Since crystal scintillators are expensive, typical PET chambers do not cover the entire body of the patient, their length ranges from 10 cm (for old scanners) to 30 cm [12, 24]. This makes a full body scan rather problematic and time consuming which in conjuction with short isotope lifetimes, requires a correction for decreasing radiopharmaceutical concetration. In Tab. 3 properties for a few most commonly used crystal scintillators are gathered. Note that they excel at high light output and efficiency of detection with respect to the plastic scintillators but possess long decay times and high attenuation lengths. Properties of typical photomultipliers used for readout from an array of crystals in PET scanners are gathered in Tab. 4. They are characterized by quantum efficiency of about 30 % and timing of about 1-4 ns.

Detection modules formed from arrays of crystal scintillators and photomutlipliers are merged together into a detection ring as depicted in Fig. 3.

Table 3: Scintillators used in PET devices, a one of the fastest created crystal scintillator ($LaBr_3$) and typical plastic scintillators [23, 26, 27, 28, 29].

Name	Density [g/cm^3]	Scintillation rise / decay time [ns]	Light output [per keV]	Light attenuation lenght [cm]
Used in PET scanners				
BGO	7.13	- / 300	6	22.8
LYSO	7.2	-/ 50	25	20.9
GSO	6.71	- / 50	10	22.2
Fast crystal				
$LaBr_3$	5.3	9 / 16	63	16.0
Plastic scinitllators				
BC-420	1.023	0.5 / 1.5	11	110
BC-404	1.023	0.7 / 1.8	12	160
BC-408	1.023	0.9 / 2.1	11	380

Table 4: General types of photomultipliers used in PET devices [30].

Photomultiplier type	Rise Time [ns]	Fall time [ns]	Transit time jitter [ns]	Quantum efficiency [%]
Conventional	2	3	0.7	28
High QE	2	3	0.7	32-45
Fast	0.7	1	0.2	28

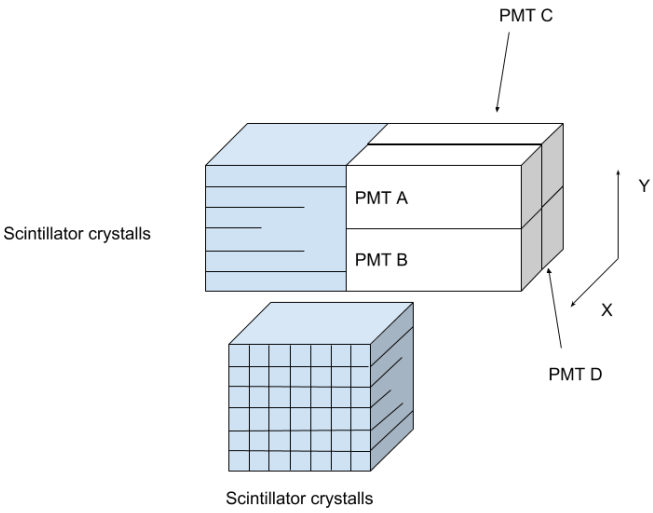

Figure 1: Scheme of how crystal scintillators are cut into pieces and connected to form a matrix of photomutlipiers. Based on [23].

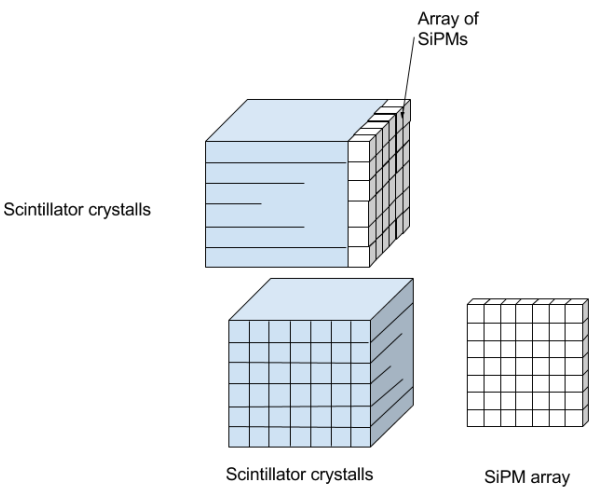

Figure 2: Scheme of how crystal scintillators are connected to a matrix of SiPM.

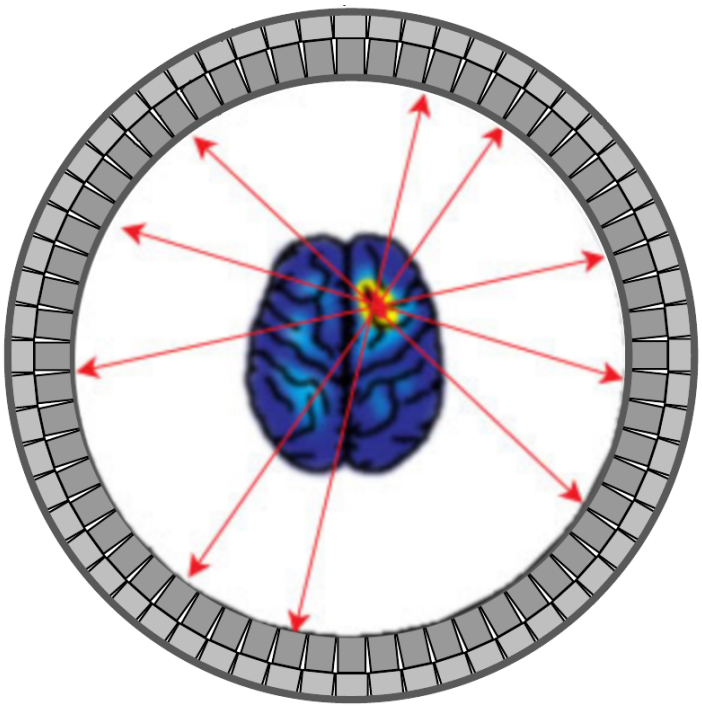

Figure 3: Example of ring surrounding a patient and a pictorial illustration of reconstruction in PET scanners. When coincident detection occurs an information about the line connecting two coincident modules is recorded. The reconstructed Line Of Response (LOR) constitute the basis for the image reconstruction.

The only information available from the scanner, is the time, the energy deposition and the position of gamma quanta interaction within the dection module. The exact gamma quanta interaction position in module segment, denoted as X and Y, shown in Fig. 1 can be calculated by measuring signal amplitudes from each photomultiplier optically connected to the side of the module [31]:

$$X = \frac{A + B - C - D}{A + B + C + D} * C_x, \tag{1}$$

$$Y = \frac{A + C - B - D}{A + B + C + D} * C_y, \tag{2}$$

where A, B, C, D denote signal amplitudes from respective photomultipliers while C_x and C_y stand for calibration constants. Then one can look for events when there was a coincident detection on both sides of a patients body (see Fig. 3) within a fixed time window. In very simplistic approach one can then draw lines connecting modules in which gamma quanta interacted, called Line Of Response (LOR). A source position can be then determined from a point of crossing of LOR lines.

3

TIME OF FLIGHT METHOD

In a standard PET examination, whole LORs are taken into account in order to perform a reconstruction. With such an approach the signal to noise ratio is low due to the determination of artificial annihilation points (see Fig. 4), worsening the overall image quality. To cope with this, the Time of Flight (TOF) of each gamma quanta can be measured for each detection (see Fig. 6) and based on the TOF the position of annihilation point along the LOR can be determined. This reduces noise in image reconstruction [4], because one is not using crossings from whole LORs, but only from a part of them as in Figs. 4 and 5. LOR length, taken into account, is proportional to the timing resolution of two detection modules. Scanners utilising this technique are called Time of Flight PET (TOF-PET) [25, 32, 33].

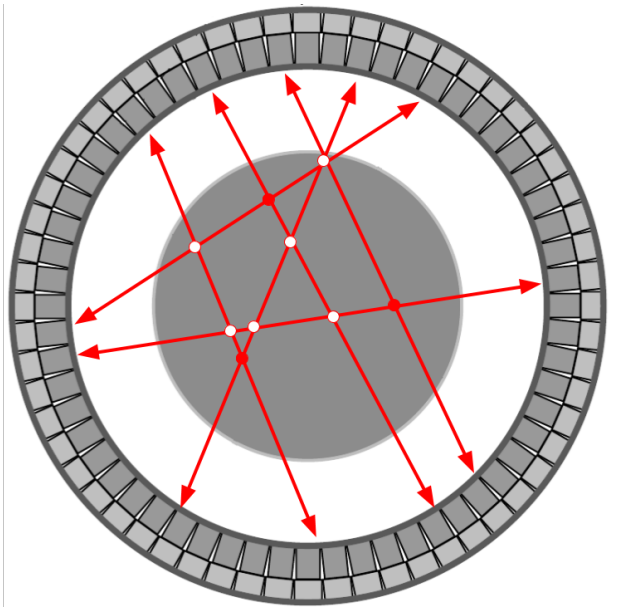

Figure 4: Pictorial representation of LOR (red lines with arrows) originating from three concentration points of $\beta+$ radioactive marker (red dots). When the whole LOR length is taken into account, false crossings are produced (white dots).

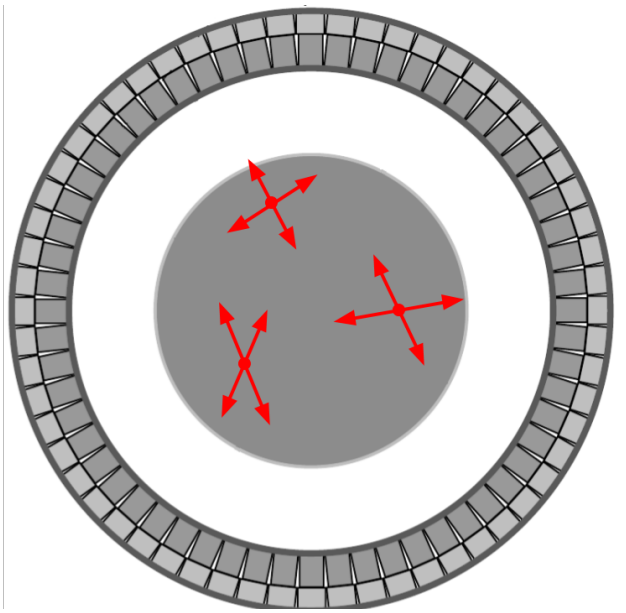

Figure 5: Pictorial representation of LOR (red lines with arrows) originating from three concentration points of $\beta+$ radioactive marker (red dots), after aplication of TOF method. As one can see it shortens LOR length, thus improving signal to noise ratio.

As can be seen from Tab. 3 the decay times of crystal scintillators used in PET are quite long, nontheless the best state of the art PET scanners can achieve very good CRT resolutions of about 400 ps [24]. This implies that if one can successfully use detectors with better timing properties than currently used, applying the TOF method would improve image quality even further.

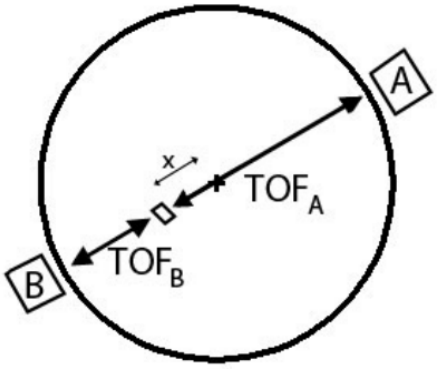

Figure 6: TOF-PET geometrical model. When annihilation takes place at distance X from the center of scanner (denoted by +) and one measures time of flight to detectors A and B, the difference between those times is proportional to the distance X.

Part II

JAGIELLONIAN PET

4

GENERAL CONCEPT

The main difference between J-PET and TOF-PET scanners lies in the detection material and method of gamma quantum position of interaction reconstruction. The J-PET scanner is built out of plastic scintillators which are less dense but possess better timing properties (Tab. 3). Plastics are easily manufactured and molded into different shapes and lengths and their production costs are lower than crystals by at least one order of magnitude.

Additionally, the attenuation length of plastic scintillators is much longer [34, 35] - in the order of 100 cm or larger, when comapred to crystal scintillators - in the order of 20 cm for LYSO and 23 cm for BGO [36, 37]. Therefore, using plastic scintillators, one can produce detectors few meters long, with a much lower absorption of light inside the detector material compared to the crystals. This makes producion of total body PETs possible in a cost effective way. The placement of photomultipliers at the ends of scintillators, enables the placement of additional layers around the patient, which results in an increased efficiency of annihilation quanta detection (see Fig. 7 for a pictorial representation).

With such design, light will be read out by photomultipliers not pointing to the center of the scanner, but placed at both ends of the scanner chamber. This implies that each interaction in the scintillator will be measured twice, once per each photomultiplier.

Plastic scintillators produce much faster scintillating signals (decay time $\sim$1.5 ns) than crystals (decay time $\sim$50 ns) (see Fig. 8 for comparison). Time information about a detected event is connected with rising flank of scintillating signals. The faster the signal rises, the smaller is the error for the determination of the time when photomultiplier signal crosses a specific voltage threshold. This difference makes improving time resolution possible for plastics since rise time of their signals are much faster (Tab. 3).

Plastic scintillators were not considered as a viable detection material for PET scanners due to their much lower detection efficiency. From Tab. 3 one can infer that, with currently known scintillators in PET scanners, one has to work with a tradeoff between short signals and probability of detection. However, with plastics, arranged axially as shown in Fig. 7 it is possible to make the detection ring longer and

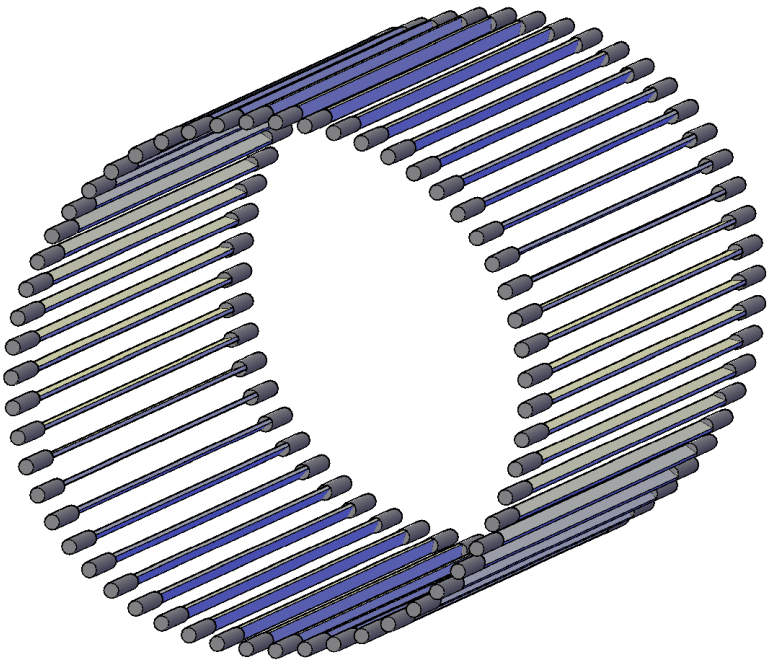

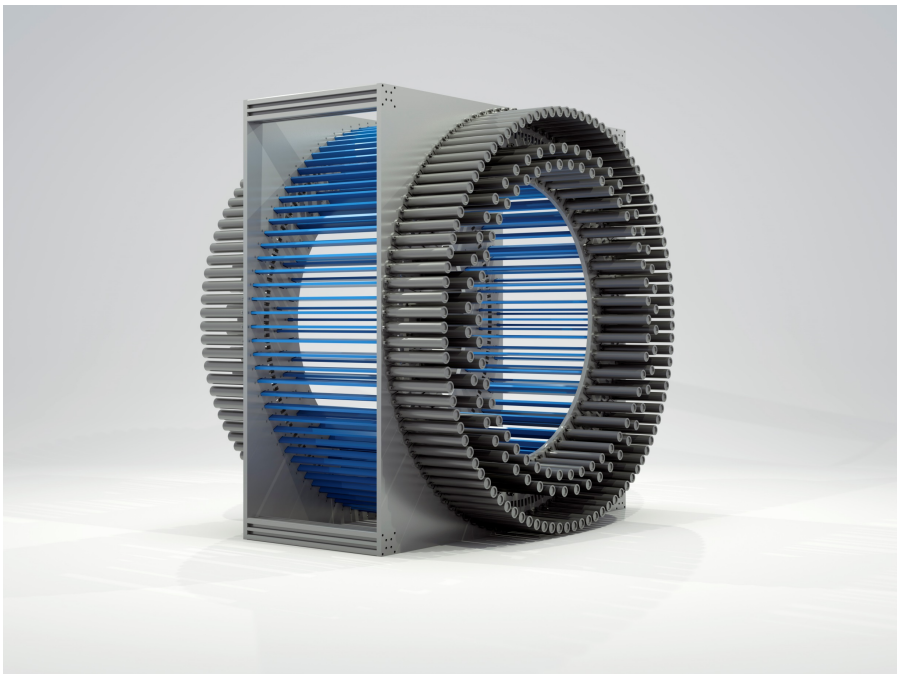

Figure 7: J-PET scanner pictures. (Top) Schematic illustration of a single layer of J-PET scanner. (Bottom) 3D rendered illustration of a first, 3 layer, full scale prototype of the J-PET tomograph [38].

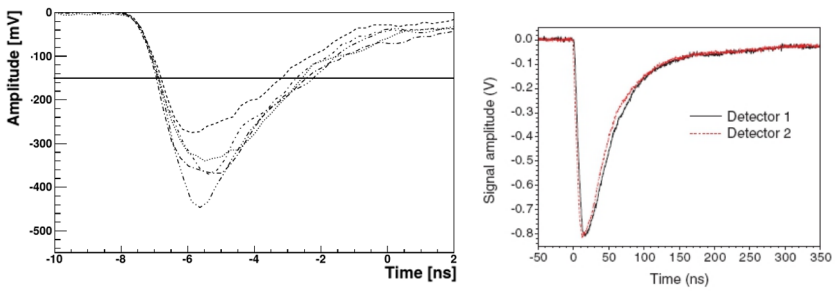

Figure 8: (Left) Signals from plastic scintillator BC420, coupled with a fast photomultiplier, with rise time of about 0.7 ns. (Right) Signals from crystal scintillator $LaBr_3$, one of the fastest crystal scintillators, with rise time of about 9 ns. Right figure is adapted from [39].

to add more layers than one. This will effectively make up for lower detection efficiency.

To reconstruct the position of annihilation one needs to measure the interaction of annihilation gamma quanta with two separate modules. The place of interaction along a module can be determined from time difference of light arrival at the edges of scintillator, while the LOR and the annihilation point along the LOR are determined using times of interaction from two detector modules - see Fig. 9.

In order to not diminish the time resolution a new type of front end electronics is needed, one that can probe signals at a few different thresholds. This will allow better estimation of a time of light arrival at the photomultipliers photocathode [8].

Since the geometry and principle of annihilation position reconstruction in J-PET scanner are utterly different from other scanners a new version of reconstruction algorithm was developed, which is capable of reconstructing gamma quantum interaction points and times [42, 43] and 3D image reconstruction, using the axial geometry of the J-PET tomograph [6, 44].

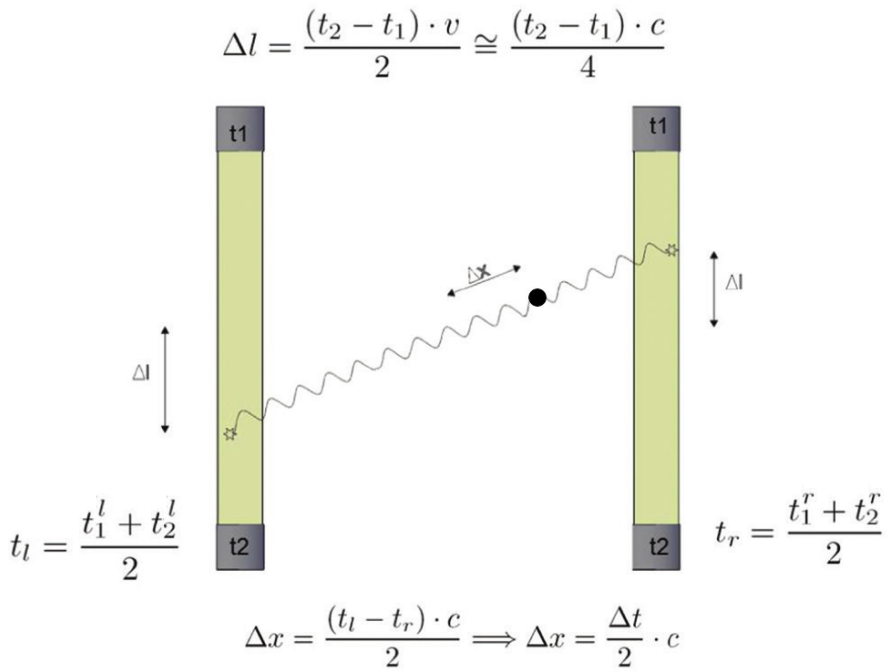

Figure 9: Principles of annihilation position reconstruction in the J-PET scanner. The time of gamma quanta interaction with a strip can be determined as an arithmetic mean of times measured by two photomutlipliers connected to its ends analogously as e.g. in the COSY-11 detectors [40]. t_l and t_r denote interaction times in the left and right strip, respectively. $t_1^{l,r}$ and $t_2^{l,r}$ stand for times measured by upper and lower photomultipliers. Position of annihilation can then be calculated from the difference of interaction times between two strips. A position of interaction along a single strip is proportional to the time difference of the signals at both its ends. Δl denotes a distance between the center of the scintillator strip and the place of interaction of the gamma quantum, v stands for effective velocity of light in scintillator strips, while c for speed of light. The dot points to the place of annihilation and Δx indicates the distance of the place of annihilation from the center of LOR. The Figure is adapted from [41].

5

FIGURE OF MERIT

The main purpose of constructing the J-PET scanner is to find a cost-effective way of performing whole-body scans. One can compare the Figure Of Merit (FOM) of available scanners by using following formula [45]:

$$FOM_{whole\ body} = \epsilon^2_{detection}\epsilon^2_{selection}\frac{A}{(CRT\ N_{steps})} \tag{3}$$

where $\epsilon_{detection}$ denotes detection efficiency of a single annihilation gamma quantum, $\epsilon_{selection}$ indicates the selection efficiency, A denotes a geometrical acceptance, CRT indicates the coincidence resolving time and N_{steps} denotes amount of measurements needed for whole body scan.

Using this formula one can compare the FOM ratio for the J-PET scanner with different scintillator lengths to state of the art scanners as presented in Fig. 10.

Since one layer of 50 cm long scintillators is enough to match the FOM value of commercial scanners, only scintillators up to 50 cm long will be investigated in the course of this work.

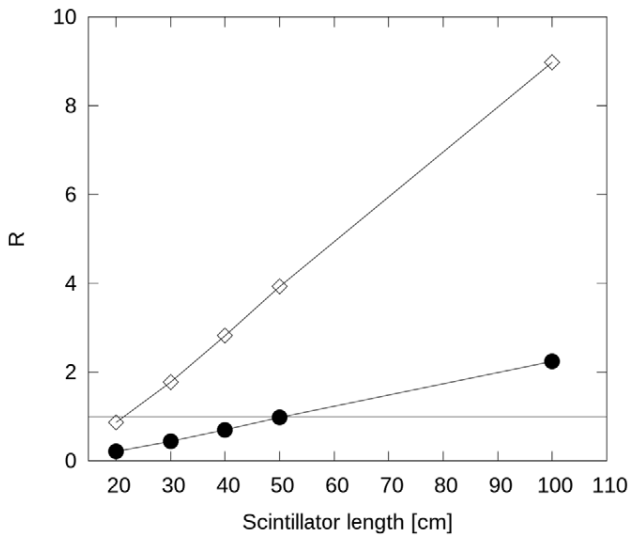

Figure 10: A ratio of figure of merits for the whole body imaging with J-PET and LSO based scanners. The horizontal axis refers to J-PET scintillator length, whereas the LSO based scanner AFOV was fixed at 20 cm. Diameters of both scanners were set to 80 cm. Full dots show results for a single layer of scintillators in the J-PET scanner, while open squares present the result for two layers. The figure was adapted from [45]. R denotes the ratio of figure of merits defined as $\frac{FOM_{J-PET}}{FOM_{LSO}}$, where FOM is defined in Eq. 3. The horizontal line is marking the R value equal to 1.

6

SCATTER FRACTION

Gamma quanta originating from the annihilation of the positron and the electron can interact with the detector material either by the Compton or the photoelectric effect. In the case of plastic scintillators, the probability of the photelectric effect is negligible due to the low Z value of its material. Thus in practice, the J-PET scanner can only detect gamma radiation by means of Compton scattering, while crystal based scanners can also detect gamma quanta through the photoelectric effect. The differential cross-section for the Compton effect has been calulated by Klein and Nishina [46]:

$$\frac{d\sigma}{d\Omega} = r_c^2 P(E_\gamma, \theta)^2 [P(E_\gamma, \theta) + P(E_\gamma, \theta)^{-1} - \sin^2(\theta)]/2, \tag{4}$$

where $\frac{d\sigma}{d\Omega}$ is the differential cross section of gamma quantum scattering into the solid angle $d\Omega$, r_c stands for the Compton wavelength of the electron, E_γ denotes initial gamma energy, θ represents scattering angle and $P(E_\gamma, \theta)$ is a the ratio of gamma energy after and before scattering:

$$P(E_\gamma, \theta) = \frac{E'_\gamma(\theta)}{E_\gamma}. \tag{5}$$

The energy of gamma quanta after scattering is connected to the scattering angle by the relation:

$$E'_\gamma = \frac{E_\gamma}{1 + \frac{E_\gamma}{m_e c^2}(1 - \cos\theta)}. \tag{6}$$

Using Eq. 4 one can derive the differential cross section $\frac{d\sigma}{dT}$, where T denotes energy gained by electron (i.e. energy deposited in detector material).

To do this one first needs to find the Jacobian needed when changing the scattering angle variable into energy gained through scattering by electron:

$$|\frac{d\theta}{dT}| = |\frac{m_e c^2}{(E_\gamma - T)^2} \frac{1}{\sin\theta}|, \tag{7}$$

where, T denotes the energy gained by electron, E_γ stands for the initial energy of gamma quantum and θ is the gamma quantum scattering angle, m_e is the mass of the electron and c is the speed of

light. Taking into acount that $d\Omega = \sin\theta d\theta d\phi$ the resulting differential crossection $\frac{d\sigma}{dT}$ reads:

$$\frac{d\sigma}{dT} = \pi r_c^2 * P(E_\gamma, T)^2[P(E_\gamma, T) + P(E_\gamma, T)^{-1} - \sin^2(\theta)]\frac{m_e c^2}{(E-T)^2}. \quad (8)$$

Note that, $\sin(\theta)$ can be expressed as a function of T and E_γ as $T = E_\gamma - E'_\gamma$ utilising Eq. 6.

When a gamma quanta originating from the annihilation scatters inside the patients body it will produce a false LOR line as presented in Fig. 11. Such events blur the reconstructed image. Depending on the scanner type, the scatter fraction can differ from 21% [47] to 36% [48]. The value of scatter fraction for the J-PET scanner was studied using GATE software and for 50 cm long plastic scintillators it amounts to 36 % [49].

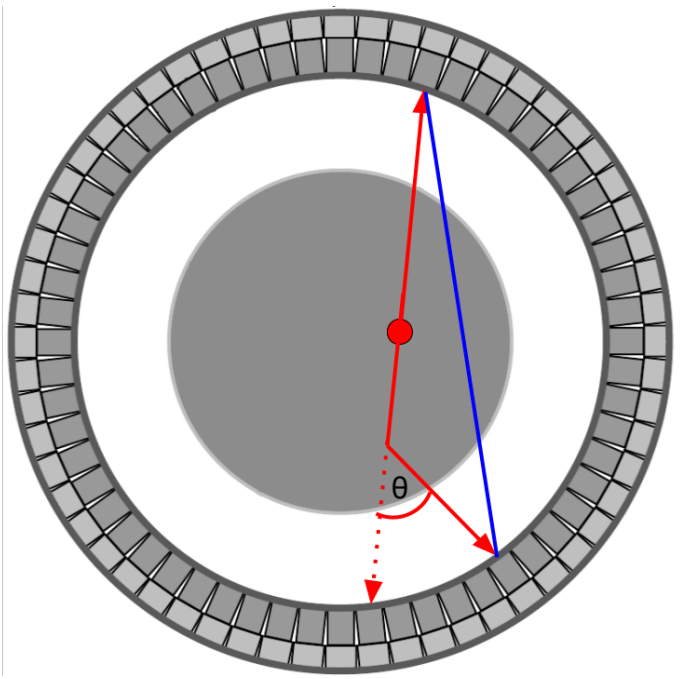

Figure 11: Pictorial presentation of scattering of gamma quanta in the patient, and its impact on the reconstruced LOR. Though the real LOR should be plotted along red and dashed red lines due to the scattering a blue LOR line will be reconstructed.

Eq. 6 gives insight on how scattering of gamma quanta under angle θ changes its energy, while it is still in the patients body. In Fig. 12 a comparison of energy deposition spectra for different gamma quanta energies interacting with the crystal scintillator, are presented. These energies where chosen assuming that annihilation gamma quantum (511 keV) undergoes Compton scattering in the patients body under 30° and 60° degrees. As expected, if the gamma quantum scatters

before reaching the detector, its energy will be smaller and thus the Compton spectrum will be narrower (see Fig. 13) and photoelectric peak will move to lower energies.

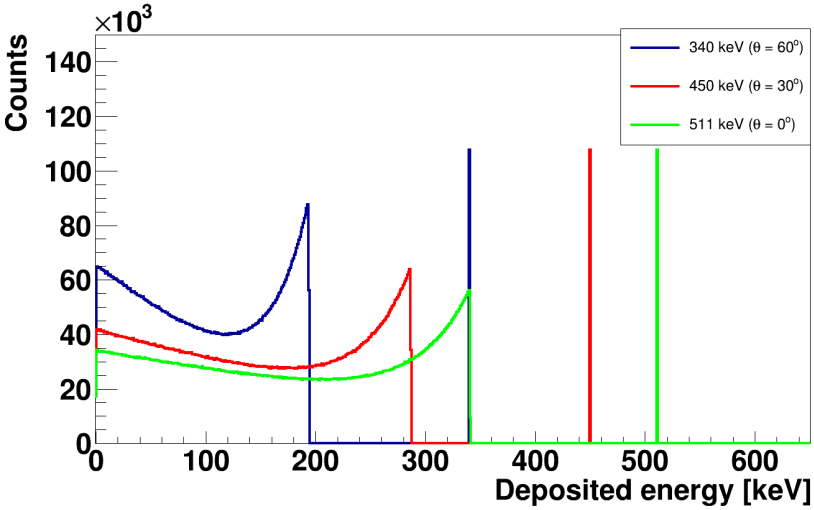

Figure 12: Simulated distributions of energy deposited in the scintillator by gamma quanta scattered in the patient under different angles θ (denoted in the plot legend). The area under the photoelectric peak was scaled to fit to the picture. A 511 keV gamma quantum after scattering under 30° (60°) degrees has energy equal to 450 (340) keV. Note that the photopeak for 340 keV gamma quanta overlaps with the Compton edge for 511 keV gamma. The Compton distributions were calculated according to Eq. 8.

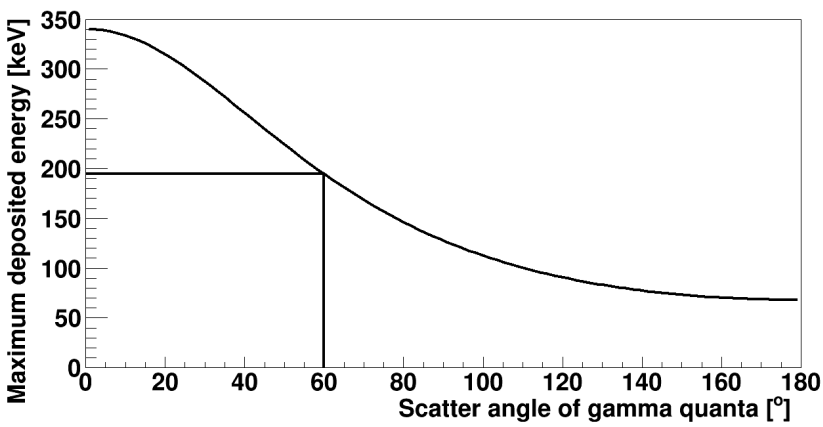

Figure 13: Maximum energy deposited by qamma quanta as a function of gamma scatter angle.

After receiving energy from impinging gamma quanta, the electron is traversing through the detector material and ionising its molecules,

which in turn produce light. The amount of light produced by the scintillator is thus proportional to the amount of energy which the electron gained through scattering with gamma quanta. Due to the fact that light production in the scintillator has a statistical origin one cannot measure spectra as in Fig. 12 but ones which are smeared as presented in Fig. 14. The smearing factor is determined as:

$$E_{exp} = E_{true} + G(0,1) * B * \sqrt{(E_{true})}, \tag{9}$$

where, E_{true} is the energy deposited in scintillator, $G(0,1)$ denotes a random number from the gaussian distribution with mean value equal to 0 and the sigma value equal to 1, B is an energy resolution factor and E_{exp} is the energy measured with the detector due to its finite resolution.

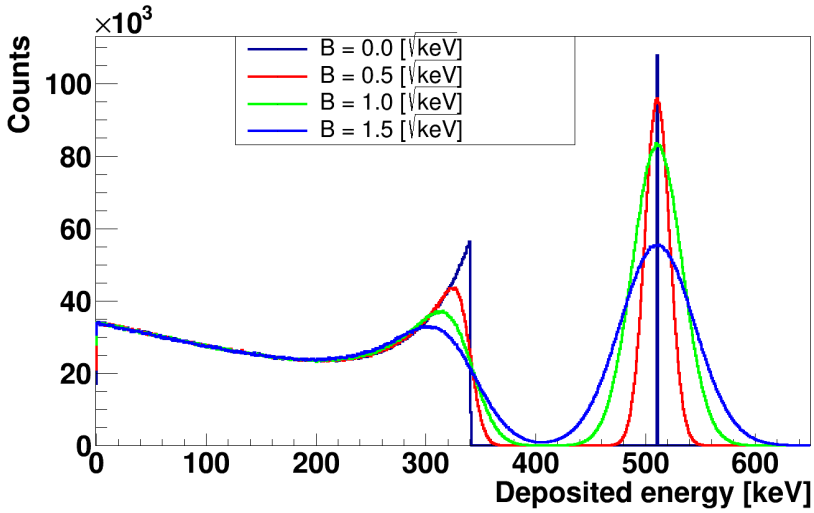

Figure 14: Simulated distributions of energy deposited by 511 keV gamma quanta in the scintillator for different energy resolutions indicated in the plot legend. Parameter B is defined in Eq. 9. Due to finite resolution one observes that the Compton maximum is suppressed and the middle of the Compton spectrum is shifted to larger values, while the photopeak maximum decreases and starts to overlap with the Compton part of the spectrum. The area under the photopeak was scaled to fit to the figure.

Scattered gamma quanta have less than 511 keV of energy. Therefore by selecting an energy loss around the 511 keV photoelectric maximum, reduces signals from the scattered gamma quanta, as it is illustrated in Fig 15. The size of the energy window used, depends on the energy resolution of the scanner. The energy resolution of detection modules ranges from 10% to even 25% at 511 keV [50]. In case of worse energy resolutions a energy window in the range of 300 -

650 keV [50] is used, which means, that gamma quantum scattering under angles larger than about 60° degrees are mostly rejected. Even with a more restrictive cut around 435 keV [50] scattering angles up to 30° degrees are accepted (see Fig. 12).

In plastic scintillators the probability for the photoelectric effect is negligible and thus one can only use the Compton spectrum in order to decrease the amount of scattered quanta. Applying an energy cut at 200 keV will be comparable to the same cut which is done in crystal-based PET scanners which use energy windows of 300 - 650 keV. In principle, this will lead to the rejection of certain scattering angles - e.g. energy cut on 200 keV would reject gamma quanta scattered into angles larger than 60 degrees. This relation is presented in Fig. 13. Note that the energy deposition is varying between 0 and the maximal value presented on the plot as governed by Klein-Nishima Eq. 4. A cut on 200 keV implies that the initial energy had to be equal to at least 340 keV which is comparable to the lower energy thresholds used in state of the art scanners.

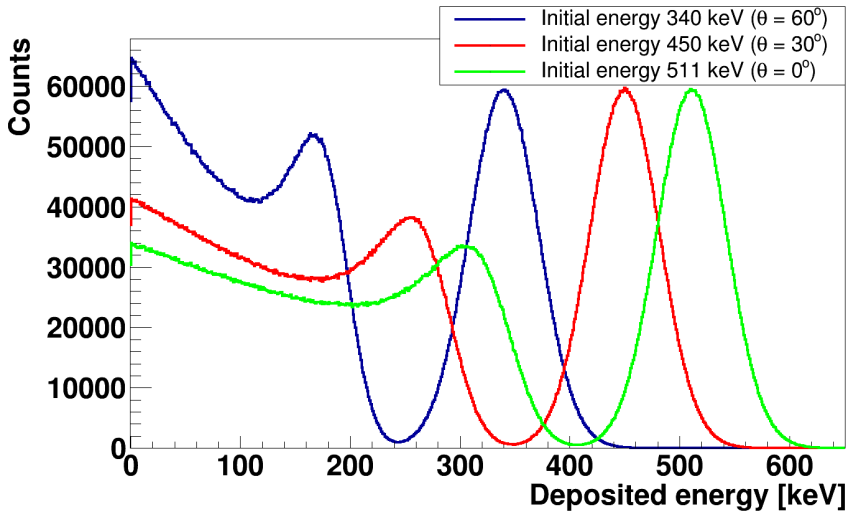

Figure 15: Simulated energy deposition inside the LSO crystal scintillator (single interaction), for gamma quanta with energies 340 keV, 450 keV and 511 keV. The spectra are smeared experimentally as in Eq. 9. Since the probability for the photoelectic effect is equal to 32% [51], the integral for the photopeak was set to the same amount.

In order to estimate how many events will be discarded due to the deposited energy cut, a Compton spectrum was simulated using a Monte Carlo method. The energy loss distribution was simulated as a convolution of Eq. 8 and the experimental resolution given in Eq. 9. As one can see from Fig. 16, about half of the registered events will be cut off when requiring energy loss larger than 200 keV.

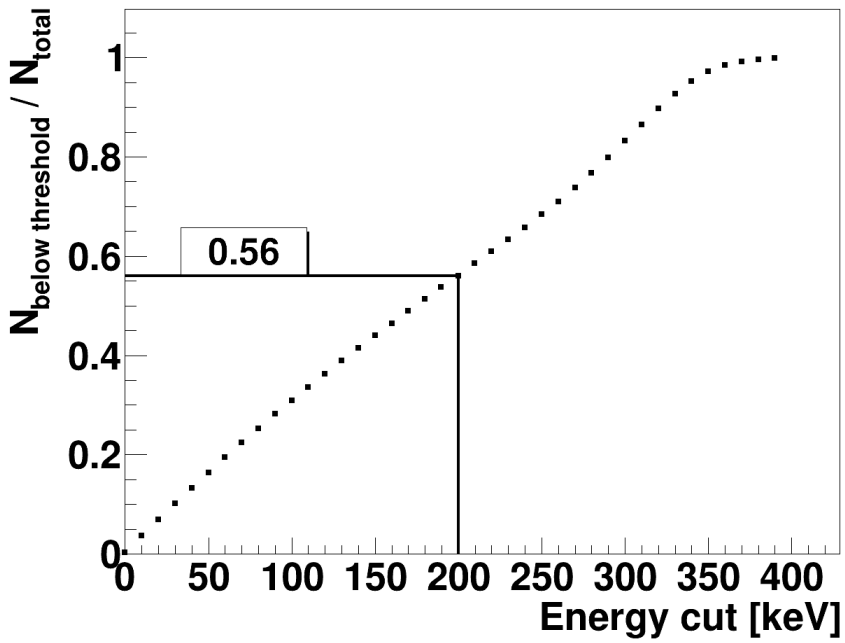

Figure 16: Simulated fraction of events discarded due to the energy cut as its function. Energy resolution was taken into account based on experimental data from 5x19x300 m^3 long scintillators [52].

Part III

J-PET DOUBLE STRIP PROTOTYPE

In this part tools used to investigate properties of the J-PET scanner are described. The simplest representation of scanner are two detection modules lying on the same plane. Such a setup is able to provide information about the spatial resolution in the 2D plane only, but it is sufficient to compare the resolution parameters with those of currently used PET scanners. A schematic representation of a two strip setup is presented in Fig. 17.

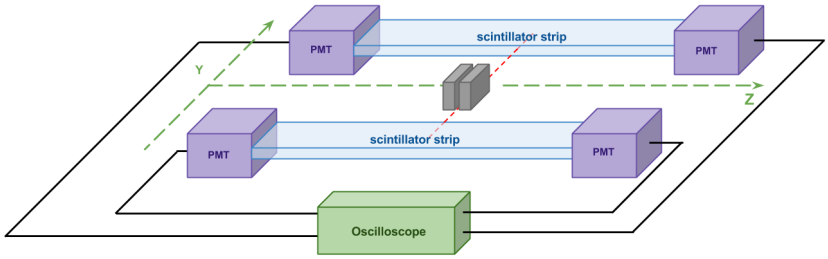

Figure 17: A two strip J-PET prototype. The setup consists of two detection modules placed on Y-Z plane. Each module is constructed from a plastic scintillator wrapped in reflective and light-tight foils and to each end of the scintillator a photomultiplier is connected via optical grease. Signals from photomultipliers are readout by a digital oscilloscope, probed in the time domain with 100 ps intervals and stored in the form of ASCII files. A lead collimator with a $\beta+$ radioactive source is moved along the Z-axis to irradiate a selected part of both scintillators.

Not only does this simplified setup give an opportunity to test energy, time and spatial resolutions but it is fairly easy to control. Additionally one does not have to suppress events scattered from other detection modules.

In the following chapters one can find a detailed description of the scintillators and photomultipliers used in the prototype as well as details on the lead collimator used for the collimation of gamma quanta from a ^{22}Na source irradiating only selected parts of prototype, the Serial Data Analyser (oscilloscope) [53] used to probe signals generated by photomutlipliers and the Framework software used for the analysis of gathered data.

7

SCINTILLATORS

Gamma quanta can deposit energy inside scintillating material via Compton effect, photoelectric effect or pair production. Due to the small energy 511 keV of the annihilation gamma quanta, the latter effect is not possible in the case of PET and its discussion will be omitted.

The photoelectric effect cross-section depends highly on the Z number ($\sim Z^4$ [54]) of the used material and thus in case of plastic scintillators (composed from hydrogen and carbon atoms), its probability is negligible.

Thus, energy deposition can only be measured via Compton scattering. After scattering, the electron from the material ionises and excites other molecules inside the scintillator. This leads to the production of photons in the visible wavelength region. The emission spectrum as well as the time parameters of the produced light signals depend on the composition of material used. In general, scintillators made from polymers have fast signals ($\sim$ 0.5 ns rise and 1.5 ns decay times), while crystal based scintillators tend to produce more light per interaction but are characterized by longer decay times (50 ns for LYSO and 300 ns for BGO).

In Tab. 3 a comparison between crystal and plastic scintillators is presented. Note that in principle, both kind of scintillators have short rise times. The plastics have a smaller light output and density, but much shorter decay times.

The general requirements for scintillators useful for TOF-PET scanners are as follows [33]:

1. short rise and decay times;
2. high light output;
3. high density and Z number;
4. low photons attenuation length;
5. emission spectrum compatible with the quantum efficiency of the photomultiplier;
6. good energy resolution;

Although plastic scintillators lack the quality from point 3., as already mentioned in Chapter 4, the efficiency of detection can be overcome by providing more detection layers and extending the AFOV. In principle, they do not fulfill point 6. as well, because the lack of photelectric effect does not allow the measurement of the energy of interacting gamma quanta. However one can measure its energy loss. When one compares actual energy loss resolutions achieved by PET scanners - from 10% to 25% [50] to the one achievable by plastic scintillators [52] - 17.6% the comparison does not show big discrepancy.

Scintillators used for tests in the two strip prototype were EJ230 [55] and BC420 [27], which are equivalent in terms of composition and timing properties. To improve light transport, scintillators were wrapped in 3M Vikuiti Enhanced Specular Reflector [56] and to ensure that they are light tight, Kapton 100B [57] foil was used.

8

PHOTOMULTIPLIERS

A photomultiplier technology is based on the concept of the photoelectric effect. Light photons traversing through the scintillator have a specific emission spectrum which depends on the material composition. The first part of the photomultiplier is called a photocathode. It is made out of a material, which can absorb photons and then knock out electrons. The second part, the electron multiplier, is composed of series of plates called dynodes, which have a positive potential. The further from the photocathode the dynode is, the higher the potential it is supplied with. This leads to the acceleration of electron from the photocathode window to the first dynode, on which it smashes with enough energy to free more electrons from dynode material. Those electrons are then accelerated to the second dynode. With each dynode the amount of electrons is increased and upon reaching the last plate called the anode, there are already enough to form an electronic pulse. The shape of the pulse depends on the dynode configuration as well as on the time distribution of light photons arriving at the photomultipliers photocathode window.

As mentioned before photomultipliers used in TOF-PET scanners have good timing properties. This means that the following properties are desired:

1. fast rising and falling times of produced signals;
2. small Transit Time Spread (TTS);
3. high quantum efficiency.

Because of that, for the J-PET scanner, state of the art timing photomutlipliers were selected for tests: R4998 and R9800. The latter photomultiplier exhibits slightly worse timing properties, but it is more affordable (see details in Tab. 5).

Table 5: Comparison of R4998 and R9800 Hamamatsu photomultipliers' properties [58]. The determination of energy and time resolutions is explained in Chapters 15 and 21, respectively. Two photomultipliers of the same type were connected to the same scintillator with dimensions 20 x 14 x 14 mm^3 irradiated at the center by 511 gamma quanta.

Photomultiplier type	Rise Time [ns]	Transit time spread [ps]	Quantum efficiency [%]
R4998	0.7	160	26
R9800	1.0	270	26

Photomultiplier type	Energy resolution at 340 keV [%]	Time difference resolution [ps]
R4998	$7.59^{+0.54}_{-0.60}$	109.8 ± 5.0
R9800	$7.71^{+0.43}_{-0.54}$	115.2 ± 2.9

9

RADIOACTIVE SOURCES AND COLLIMATOR

Annihilation quanta used in PET tomography come from $\beta+$ radioactive markers injected into the human body. In the case of a laboratory experiment a source of $\beta+$ emitter is sufficient. Two main candidates for acting as source of 511 keV gamma quanta are ^{22}Na (2.602 years half-life) and ^{68}Ge (270.95 days half-life). The main advantage of the sodium source is its lifetime, which makes prolonged series of test possible, before source activity goes down so much that measurements will be too time consuming. The drawback of ^{22}Na is that after emitting a positron, the newly formed neonium nucleus is excited and will deexcite by the emission of gamma quantum (see Fig. 18).

To understand the interaction between annihilation gamma quanta and the scintillators, an irradiation of a small portion along the strip is required in series of steps. This demand is fullfiled by collimating gamma rays by a lead collimator. A schematic representation of such device is presented in Fig. 19 and photo in Fig. 20.

A measurement of the profile of gamma quanta going out of the collimator was performed to test if the irradiated part of scintillator is significantly smaller than the desired position resolution (see Fig. 19). The number of measured events as a function of the beam position when there is a lead brick ("shadow") placed between scintillator and the collimated source can be expressed as a convolution of the beam profile $h(x)$ and the detector acceptance $g(x)$:

$$M(x) = h(x) * g(x) = \int_{-\infty}^{+\infty} h(x - x')g(x')dx'. \tag{10}$$

The acceptance of the detector can be assumed to be 0 when gamma rays are hitting the lead block and 1 when they are not:

$$g(x) = \begin{cases} 0 & \text{if x} \in [x_0, +\infty], \\ 1 & \text{if x} \notin [-\infty, x_0]. \end{cases} \tag{11}$$

Inserting Eq. 11 into Eq. 10 and derivating one gets:

$$\frac{d}{dx}M(x) = h(x - x_0). \tag{12}$$

This means that by measuring counts at different positions of the collimator one can get information about the beam profile function $h(x)$ of gamma quanta from the collimator.

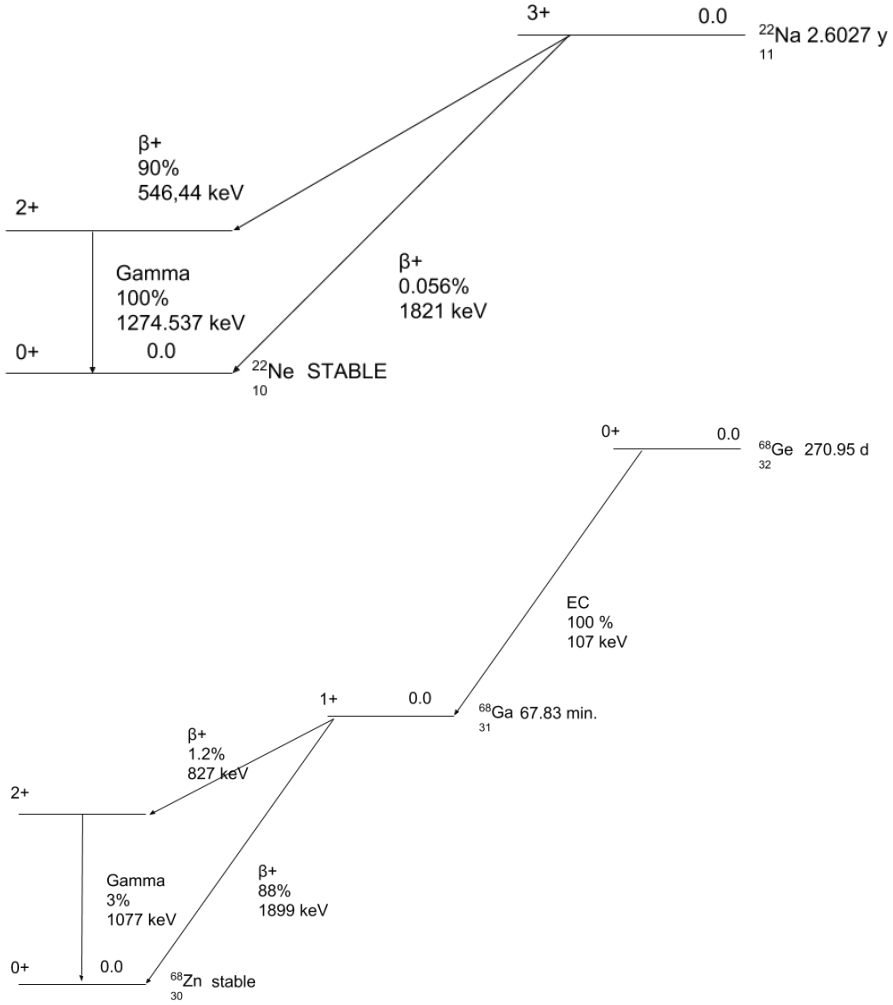

Figure 18: Decay schemes of β^+ radioactive sources used in measurements. Note that germanium decays only by electron capture into galium 68, then in $\sim$ 89 % of cases galium decays by positrion emission into zincum which, in turn, is in an excited state in about $\sim$1% of cases, from this state it can emit a 1077 keV gamma quantum. In comparison, most of the sodium decays contain gamma quanta from neonium deexcitation. Only the most probable β^+ transitions are shown in the Figure.

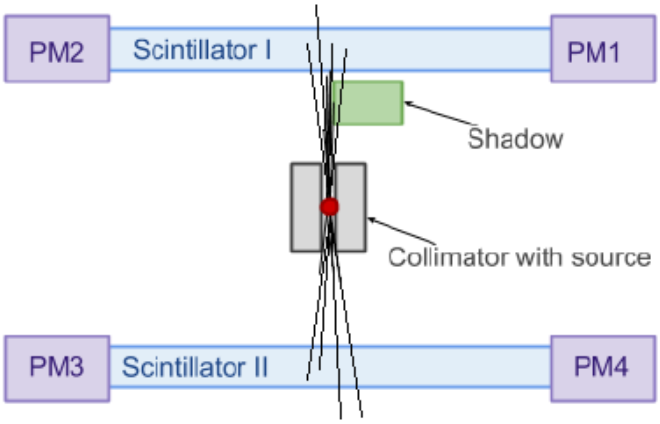

Figure 19: Experimental setup for the beam profile measurement. Between the collimator with a ^{22}Na source (slit 1.3 mm) and one of the 5 x 19 x 300 mm ^{3} scintillators a 50x70x70 mm ^{3} lead brick ("shadow") is placed. Number of events was measured as the number of coincident signals in both scintillator detectors. Figure is not to scale. [59]

In Fig. 21 the dependence of measured counts in fixed time intervals for different positions of the collimator is presented, while in Fig. 22 a derivative of the same graph is presented with a gauss function used to estimate the profile of the beam. The collimator slit was set to 1.3 mm and the width of the beam after transversing 12.7 cm was measured to be about 1.6 mm. This beam spread is smaller than the expected position resolution so no further adjustments to the collimator were performed.

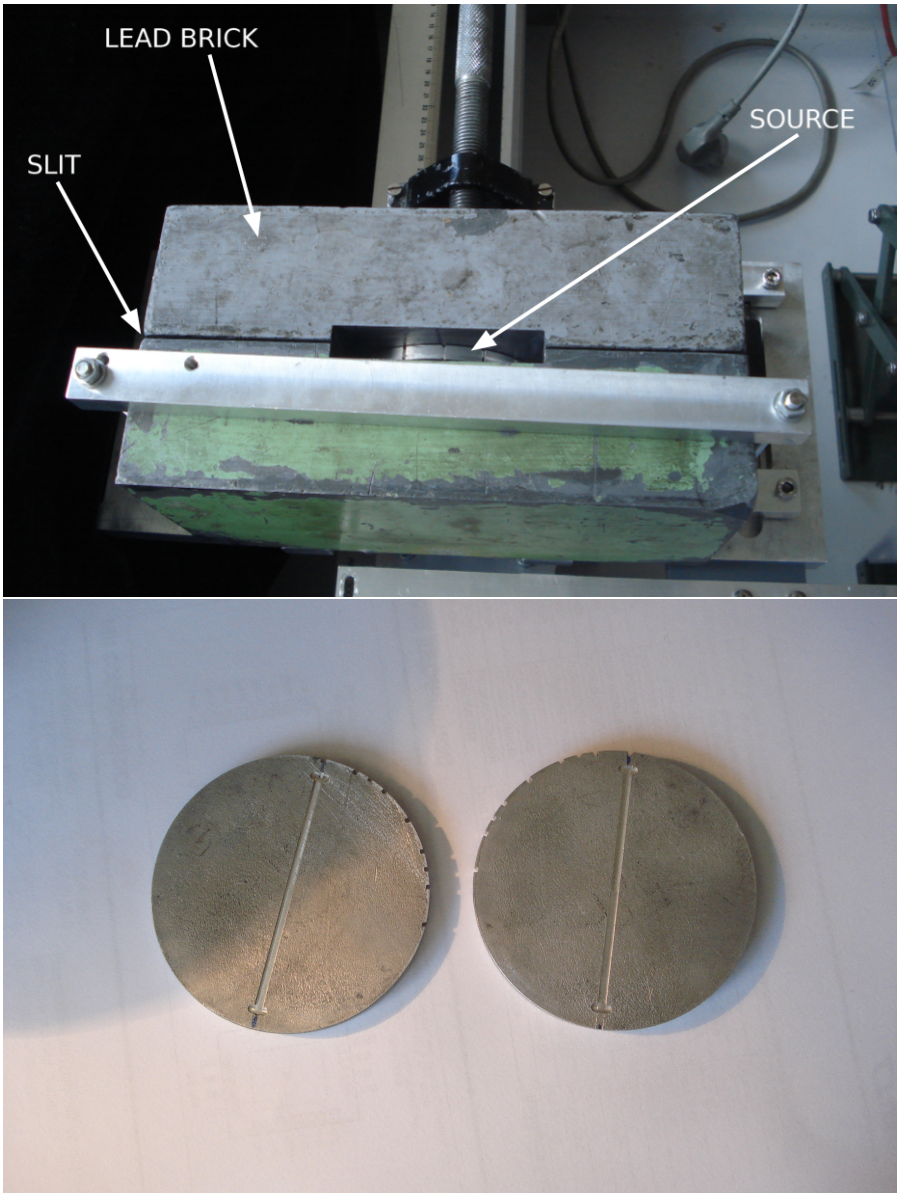

Figure 20: (Top) Lead collimator used to irradiate only small portions of the scintillator strip. The slit width can be changed and the whole collimator can be tilted as well as moved along the plastic strip with very high precision (1 deg for tilt and 0.1 mm for movement). (Bottom) aluminium disk used for placing the radioactive germanium source inside the collimator.

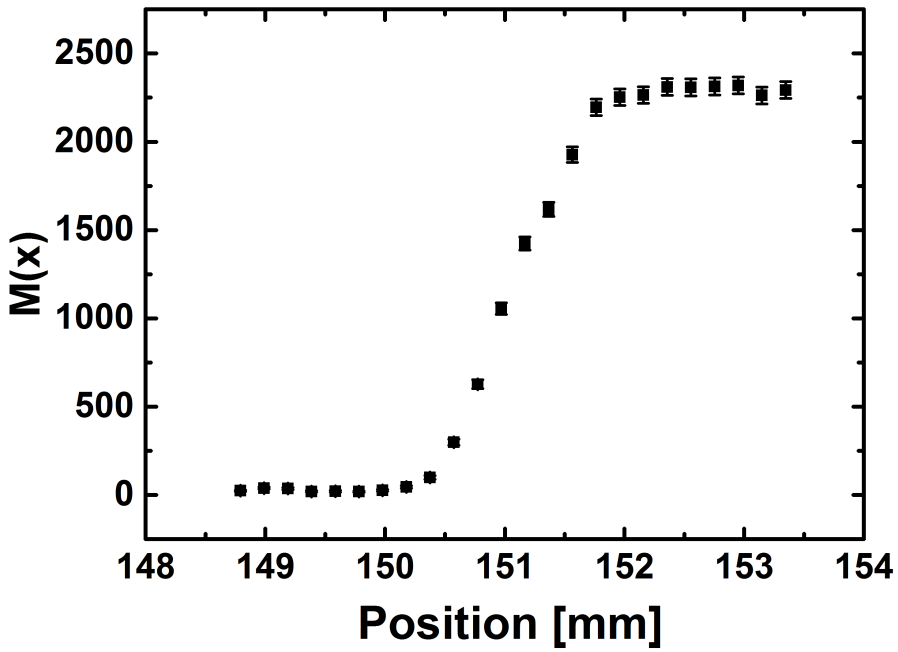

Figure 21: Measured counts as a function of the collimator position.

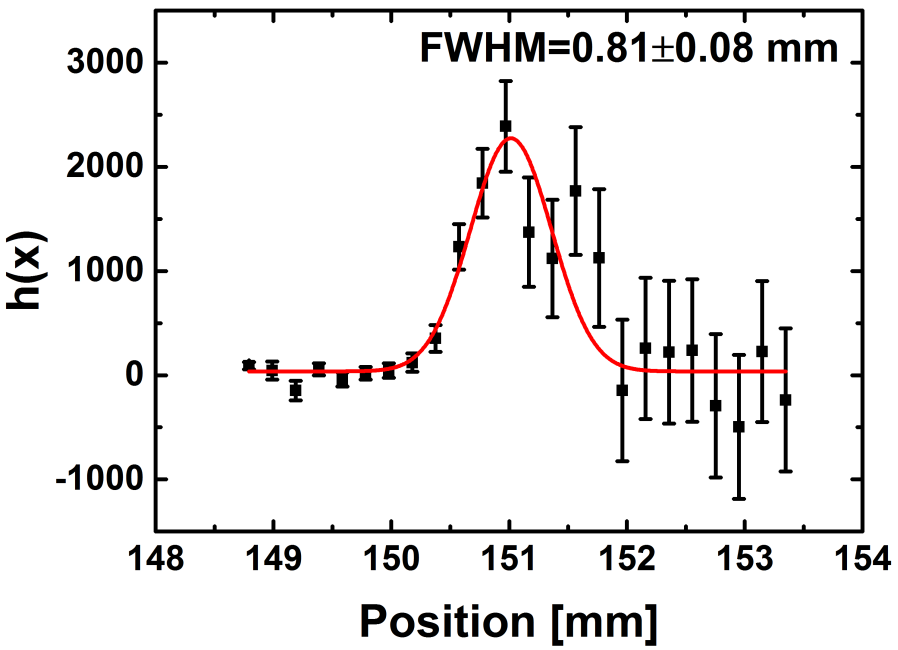

Figure 22: Derivative of $M(x)$ defined in Eq. 10, using data from Fig. 21. The superimposed line indicates the gaussian function fit to the experimental points.

10

SERIAL DATA ANALYSER

Signal acqusition from the two strip J-PET prototype was performed using a Serial Data Analyser (SDA). Such device makes it possible to acquire full waveform of signals from photomultipliers.

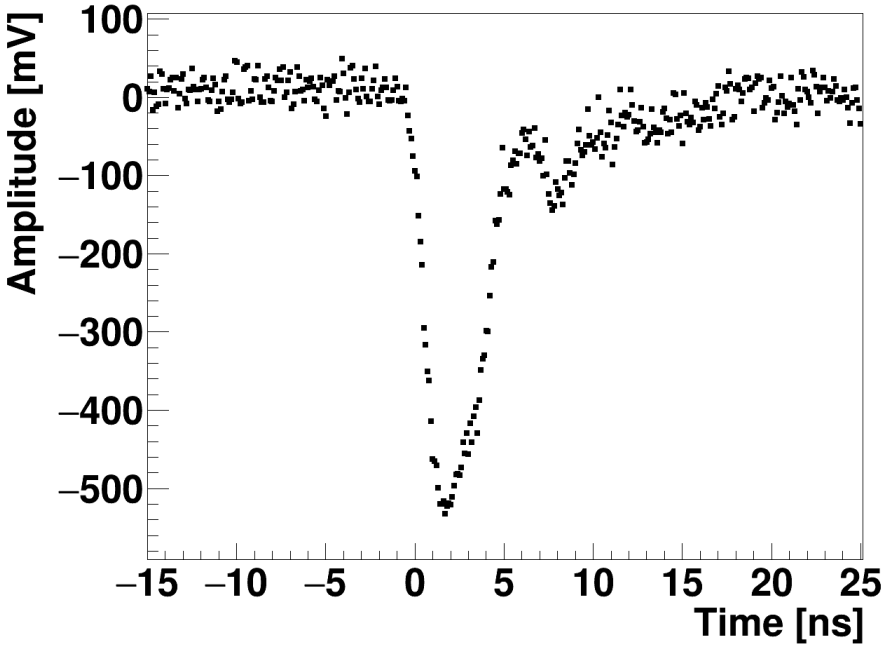

Figure 23: Scintillation signal from one of the tested modules, acquisited by the SDA device. Each signal consists of 500 points measured in 100 ps time intervals. The ragged falling edge of the signal results from the photons arriving as the last ones at the photomultipliers surface.

An exemplary signal is presented in Fig. 23. Since the whole shape of the signal is available, studies of scanner performance can be realized as well as different approaches to signal analysis and extraction of physical information can be tested.

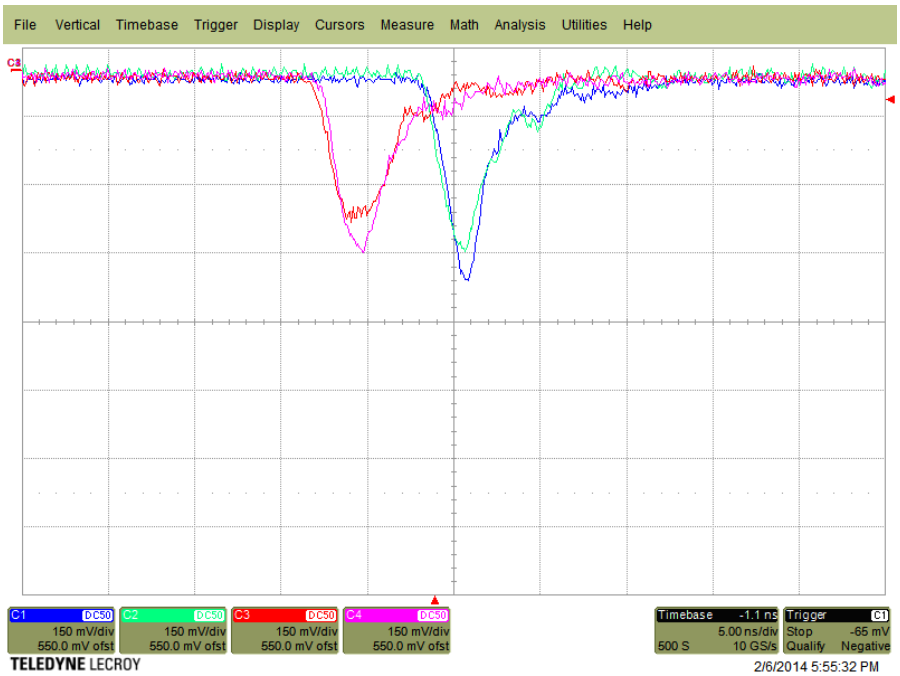

Figure 24: Screenshot of the SDA screen with four signals obtained using the coincidence triggering condition. The source was irradiating the center of the 5x19x300 mm^3 modules (see Fig. 17). Each such event has been saved as an ASCII file to the SDA drive. The cables length used to readout from one scintillator was longer than from the other by $\sim$ 1 m.

In Fig. 24 a screenshot of signals from gamma quanta hitting the center of the scintillator is presented for 5x19x300 mm^3 modules. To acquisit a signal a coincidence of signals from two photomultipliers, each from a different scintillator, was required.

11

EXPERIMENTAL SETUP

The final version of the experimental setup consisted of:

- a pair of EJ230 scintillators with dimensions given in Tab. 6, wrapped in vikuiti foil for the reflection of light and kapton foil for light tightness;
- two pairs of R9800 photomutlipliers, connected at each end of the scintillator via optical gel;
- SDA6000 oscilloscope for signal probing;
- lead collimator which could house either a ^{22}Na or a ^{68}Ge source and a styrofoam stand for the placement of point like sources;
- a mechanical structure, with a rail for the possibilty of precise and automatic collimator movement;

In order to test the two module prototype of the J-PET scanner, three different types of measurements were performed:

1. a voltage scan at the central position of irradiation - in order to determine optimal operating voltage;
2. a scan with small, 3 mm steps along the strips with the source inside the collimator - in order to determine time and energy calibration as well as time and energy resolution as a function of the interaction position;
3. bare source measurement at different positions - to estimate PSF and CRT parameters and compare them with state of the art scanners and to check if image reconstruction algorithms are working correctly;

Results from tests on a two module setup, can be extrapolated to the whole scanners performance, since each pair of detector modules is supposed to behave in the same manner.

In Fig. 17 (diagram) and 25 (photo) a setup used for irradiating only selected parts of scintillators is presented. Note that only two axes are needed for representing the experimental setup formed from the two module prototype.

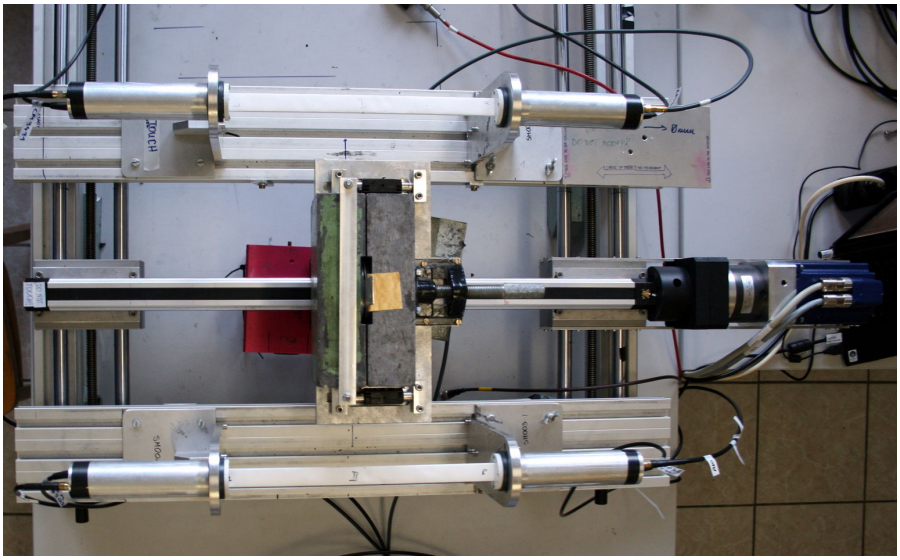

Figure 25: A photo of a two strip setup used for scan at different irradiation positions along both strips. Photomultipliers are placed in metal mountings. To each photomultiplier a SMA cable is connected to collect signals by oscilloscope and a SHV cable to provide power supply. Scintillators are wrapped in reflective and light tight foils (white in the picture). Collimator body can be moved by means of a step motor seen on the right edge of setup, its slit size could be manually adjusted to select the desired beam profile. A radioactive source is placed inside the collimator. The whole setup is placed on aluminium profiles, one module is stationary while the second one could be moved relative to the first one.

In case of a bare source measurement a different stand was prepared to study how well one can reconstruct the source position (see Fig. 26). This construction allowed measurements at the central position between the scitillators as well as 10 cm off the center along the Y and Z axes and thus made studies of the image reconstruction algorithm possible. In Tab. 6 a summary of performed measurements is presented.

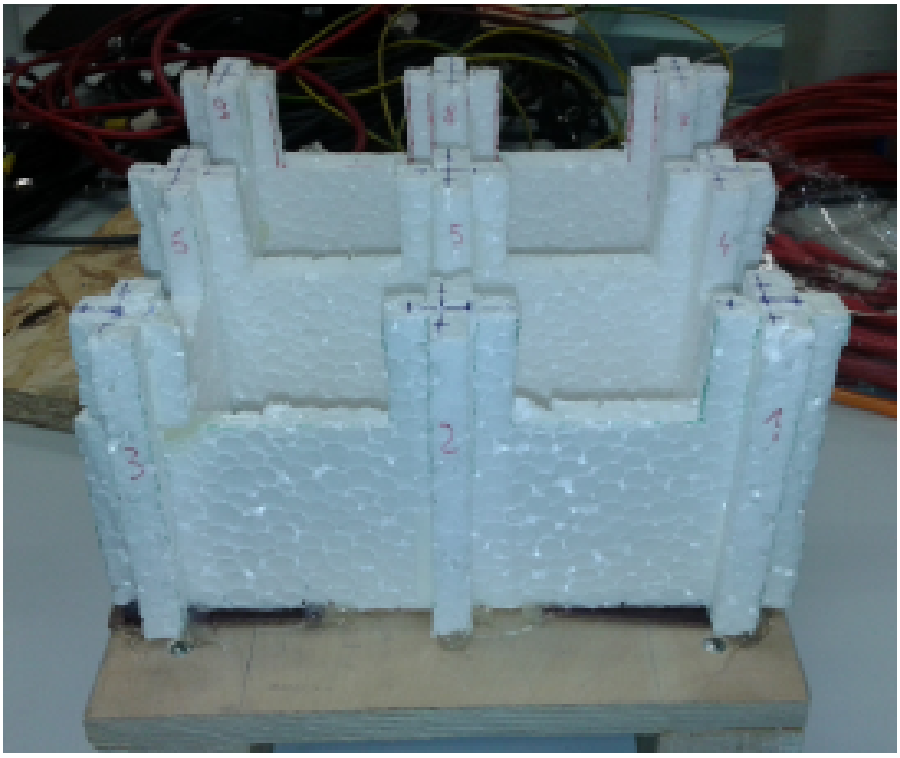

Figure 26: A stand prepared for source placement in bare sources measurements. A styrofoam skeleton was placed on a wooden stand for stability. The central pillar corresponded to the central position of the experimental setup and the distance between the pillars, along both axes, was equal to 10 cm.

Table 6: Measurements performed on a two strip prototype in the scope of this work.

Scintillator dimensions [cm]	Type of mesurement
2 x 1.4 x 1.4 cm^3	voltage scan
0.5 x 1.9 x 30 cm^3	scan along strips
0.5 x 1.9 x 30 cm^3	bare source
0.7 x 1.9 x 50 cm^3	scan along strips

12

J-PET FRAMEWORK SOFTWARE

The data gathered in this work by the SDA needs to be processed in order to produce useful information for the development and tests of low-level and image reconstruction algorithms. These algorithms will be used in the full version of the J-PET scanner. In case of the J-PET scanner a dedicated analysis framework, the J-PET Framework has been developed [18]. Its main concept is to decompose the analysis chain into seperate blocks. Each block is responsible for a certain processing task (see Fig. 27). The initial data from J-PET detector is generated by a dedicated DAQ system. The system is providing data in binary (raw) format. Then step two of the reconstruction (the low level one) is applied to the data. The goal of this step is to calculate positions, times and energy loss of gamma quanta within the scintillators. At the final stage high level iterative image reconstruction algorithms are used. Chapters 13 - 18 and 24 - 28 contain a description of modules used to analyse data on the low reconstruction level. Chapters 29 and 30 contain a description of studies on high level reconstruction.

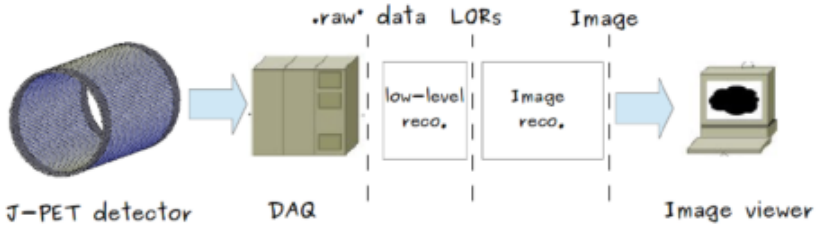

Figure 27: Sample workflow diagram for data processing in J-PET Framework [18].

The Framework was developed mainly in C++11 with addition of ROOT and Boost libraries.

In the course of this work several proccessing blocks in the Framework were developed in order to analyse the data.

Part IV

DATA ANALYSIS

13

PEDESTAL VALUE CALCULATION

In this Chapter an algorithm for calculating the signal pedestal value is presented.

Each signal acquisited by the SDA unit may be shifted from 0 on the amplitude axis by a small value (see Fig. 28). This value will be further on called the pedestal. Since the pedestal is different than 0 one would need to take it into account when calculating signal parameters such as time at threshold or area under the signal curve. To solve this problem one can calculate the pedestal and then shift the whole signal according to its value, so that its noise line will be placed at 0.

To properly calculate the pedestal one needs a signal acquisited in a time window larger than the signal width and preceeding the rising flank. Next the first twenty points of such acquisited signals are used to estimate the mean noise value ($\bar{x}$) and standard deviation (σ) of the noise distribution. A region of $\bar{x} \pm 3\sigma$ will be further referred to as the noise level (see Fig. 29).

The next task is to find the beginning of the signal. In order to achieve this, first the lowest point in the signal (which is equal to its amplitude) is taken. Next moving point by point to the left from the lowest point, the value of voltage is checked and compared with the noise level. When the point enters the noise level the iteration is stopped and the position of the point is marked as the beggining of the signal (see Fig. 29).

All points before this point are considered as noise originating from the SDA and the photomultiplier and can now be used to estimate the pedestal value. Since noise points are gaussian distributed one can calculate the pedestal as an arithemtic mean of their voltage values. This procedure has to be repeated for each signal, since the pedestal value is not necessarily constant and can vary from signal to signal.

In Fig. 30 exemplary histograms of noise distribution for four different input channels from the SDA are presented. The mean values of these distributions are used to estimate the pedestals.

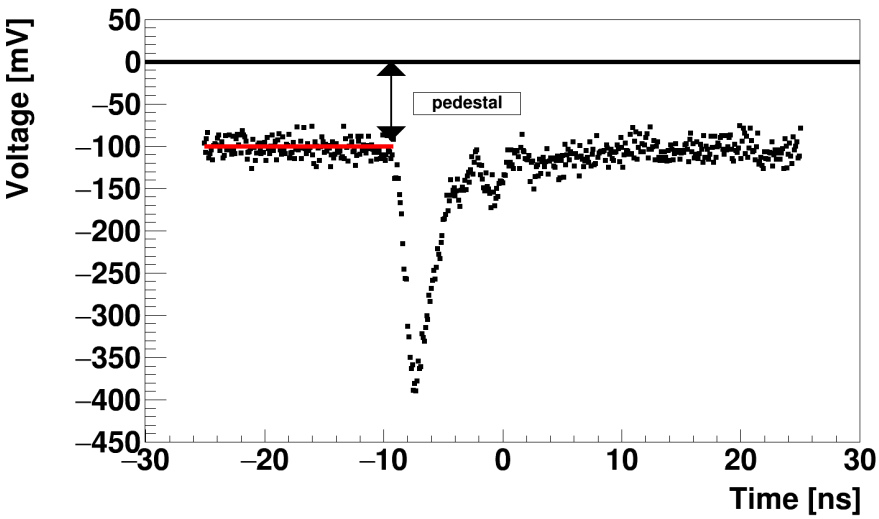

Figure 28: Signal from a R9800 photomultiplier collected using the SDA unit. For the better visualisation and definition an additional -100 mV pedestal was added to the signal. Note that this shift is added only in this figure in order to illustrate the definition. Next figures show the real signal pedestal.

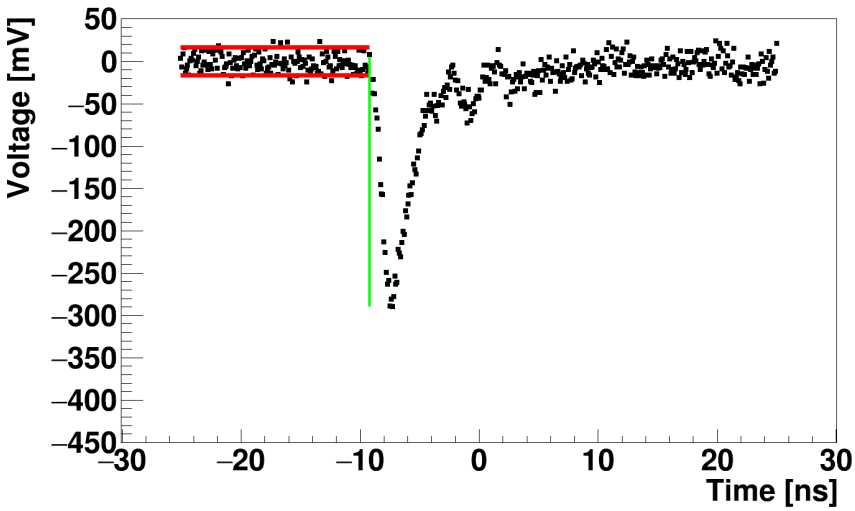

Figure 29: Signal from the SDA unit without pedestal correction. The region between the two red lines is considered to be the noise level ($\bar{x} \pm 3\sigma$ calculated based on first 20 noise points of the acquisited signal). The green vertical line indicates the time of the first point that is considered a part of the signal.

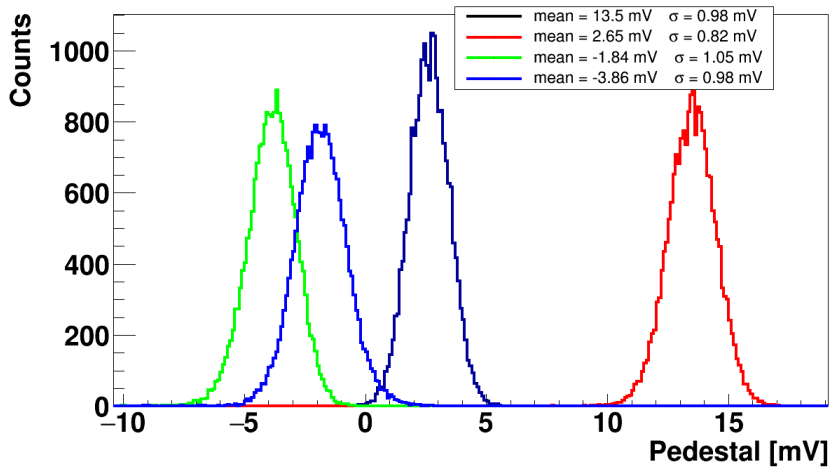

Figure 30: Noise spectra for four detection channels. The mean value and the standard deviation of the gaussian function fit to each spectrum is shown in the plot legend. Note that each channel has a different pedestal value as well as spread.

14

CHARGE CALCULATION

To calculate the charge gathered in a signal from a photomultiplier, first the signal is corrected for the pedestal value and next a Riemann integral is performed:

$$Q = \int \frac{V(t)}{R} dt, \tag{13}$$

where $V(t)$ is a voltage observed by the scope as a function of time and R is the resistance at the input, which is equal to 50Ω. The analytical form of function $V(t)$ is not known, only function values at certain time stamps are measured. Therefore one expresses the integral as sum from the first to the last point of the signal as:

$$Q = \sum_{\text{first point}}^{\text{last point}} V(t_i)(t_{i+1} - t_i) \tag{14}$$

Since the starting point of the signal is known (see Chapter 13), the sum starts from this point and ends at the last acquisited signal point.

An example charge spectrum gathered at a single irradiated position along the scintillating strip is presented in Fig. 31. As predicted by Klein-Nishima formula in Eq. 8 the observed spectrum possesses a Compton spectrum shape. The experimental Compton spectrum is influenced by the setup resolution, which is reflected in the smearing of the Compton edge.

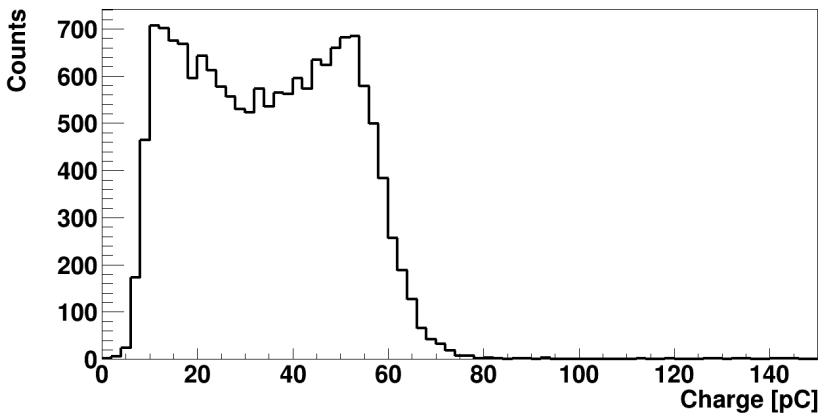

Figure 31: Example charge spectrum collected at a single irradiated position along the scintillating strip. Note that the shape results from the convolution of the Klein-Nishima equation and the experimental resolution. The spectrum is cut at the left side at the value of around 10 pC due to the threshold set at the SDA unit.

15

ENERGY DEPOSITION

The charge Q of the measured signal is proportional to the number of photoelectrons, which is proportional to the number of photons reaching the photocathode, which in turn is proportional to the energy deposited by the gamma quantum in the scintillator. Thus in general:

$$Q = C_1 N_{phe} = C_2 E_{deposited} f(x), \tag{15}$$

where $f(x)$ denotes the probability that a photon emitted at the distance of x from the photomultiplier will reach the photocathode, and the C_1 and C_2 constants are subject to calibration. For the long scintillator strips, excluding the regions close to the photomultipliers, $f(x)$ can be roughly approximated as $e^{-\lambda x}$, where λ denotes the effective absorption length of the light signal and x is the distance from interaction point to the photomultipliers photocathode. Therefore, in case of measurements at two ends of the strip the geometrical mean of the charge of signals measured at the left and right sides should be proportional to the deposited energy independently of the position of irradiation:

$$\sqrt{Q_L Q_R} = \sqrt{C_L C_R E^2_{deposited} e^{-\lambda x} e^{-\lambda(L-x)}} = \sqrt{C_L C_R} E_{deposited} e^{\frac{-\lambda L}{2}} = C E_{deposited}. \tag{16}$$

However in practice effects such as the rapid change of the solid angle with the distance to the photomultiplier and the dependence of the attenuation constant λ on the wavelength of emitted photons, deteriorate this dependence and the simple averages (as geometrical or arithmetic) depend both on the energy and position. The parameter C varies with the position x and needs to be established for each detection module as a function of x.

The energy resolution depends predominantly on the number of photoelectrons produced at the photocathodes of both photomultipliers. The larger this number, the better the energy resolution because the statistical fluctuation of the number of signal carriers decreases. Thus in the first approximation energy resolution is proportional to the square root of the number of photoelectrons released from the photocathodes of both photomultipliers. Therefore, for the consideration of the energy resolutions it is more natural to express the energy

deposition in terms of the number of photoelectrons instead of the signal charges and to use an arithmetic mean as measure of $E_{deposited}$. In such case:

$$E_{deposited} = A\frac{N_L + N_R}{2}, \tag{17}$$

where A denotes an energy calibration factor. If the errors of N_L and N_R were uncorrelated then the fractional energy resolution would read:

$$\frac{\sigma(E_{deposited})}{E_{deposited}} = \frac{1}{\sqrt{N_L + N_R}} = \frac{\sqrt{\frac{A}{2}}}{\sqrt{E_{deposited}}}. \tag{18}$$

Therefore, the energy resolution as a function of the deposited energy may be approximately parametrized as:

$$\frac{\sigma(E_{deposited})}{E_{deposited}} = \frac{\beta}{\sqrt{E_{deposited}}}, \tag{19}$$

where β is an effective proportionality constant. Since the charge produced by a photomultiplier is proportional to the amount of photoelectrons which hit the photocathode, one can expect that:

$$\frac{1}{\sqrt{N_L + N_R}} = \frac{1}{\sqrt{C_L Q_L + C_R Q_R}} = C\frac{1}{\sqrt{Q_L + Q_R}}, \tag{20}$$

where one assumes that $C_L = C_R$ which can be experimentally performed by matching the gains of photomultipliers.

The value of β can be obtained by compariing the experimental distribution of $\frac{Q_L+Q_R}{2}$ with the simulated histogram of the deposited energy.

The distribution of energy deposition of the annihilation quanta $N_{sim}(i, \alpha, \beta)$ was simulated based on the Klein-Nishina formula [46, 60], convoluted with the detector response with a resolution of $\frac{\sigma}{E}$ parametrized by Eq. 19. The i indicates the energy bin, α stands for the scaling parameter and β is defined in 19. The fit was perfomed in the range from 200 keV to 380 keV. The lower range of the spectrum was not taken into account since it is enhanced by signals originating from gamma quanta scattered in the collimator or the material surrounding the detector. While the upper part was neglected due to low statistics in that region and the secondary scatterings of gamma quanta in the scintillator.

In Fig. 32 the energy loss scaling parameter (α) is defined pictorially. In the fit α, β and the normalisation constant V were treated as a free parameters. A fit was conducted by constructing a Neyman χ^2 statistic [61] defined as follows:

$$\chi^2(\alpha, \beta, V) = \sum_i \frac{(VN_{sim}(i, \alpha, \beta) - N_{exp}(i))^2}{N_{exp}(i) + N_{sim}(i, \alpha, \beta)V} \tag{21}$$

where i denotes the i_{th} bin of histogram and N_{sim} is the simulated spectrum, but with its energy loss values rescaled by α.

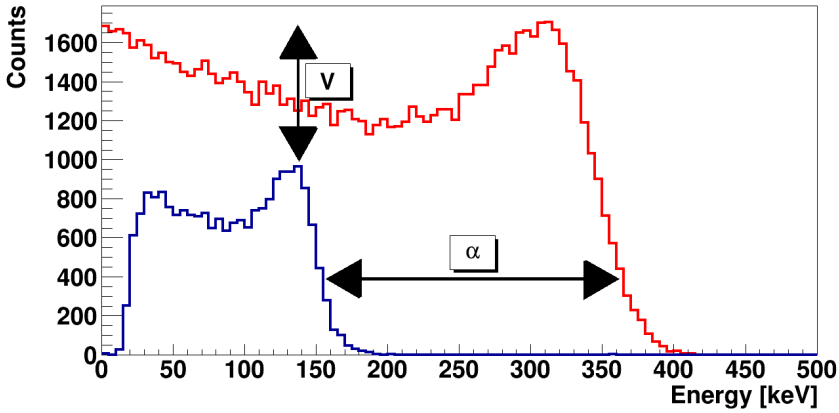

Figure 32: Experimental spectrum (blue) and simulated spectrum (red) before rescaling. Scaling in amplitude (factor V) and in energy scale (α) is indicated pictorially.

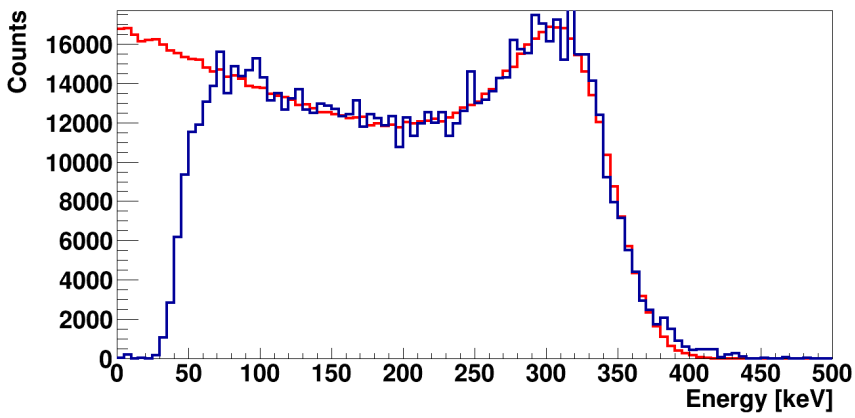

Figure 33: Experimental energy deposition spectrum (blue) resized to match simulated one (red). Note that only the region from 200 to 380 keV was taken into account when performing the fit.

The statistical uncertainities for each of the fit parameters were estimated according to reference [62].

As a next step a relationship between the interaction position along the strip and the value of α was determined. In practice a cut on a selected energy threshold requires knowledge of the energy callibration of the detector system. Gamma quanta when interacting with the scintillator matter produce light, which is converted into charge by the photomutliplier. Thus one has to know the proportionality fac-

tor between the charge generated by the photomutliplier and the energy deposited inside scintillator. An example of such a dependence is presented in Fig. 34 for a 5x19x300 mm^3 scintillator. As one can see this dependence is well described by second order polynomial.

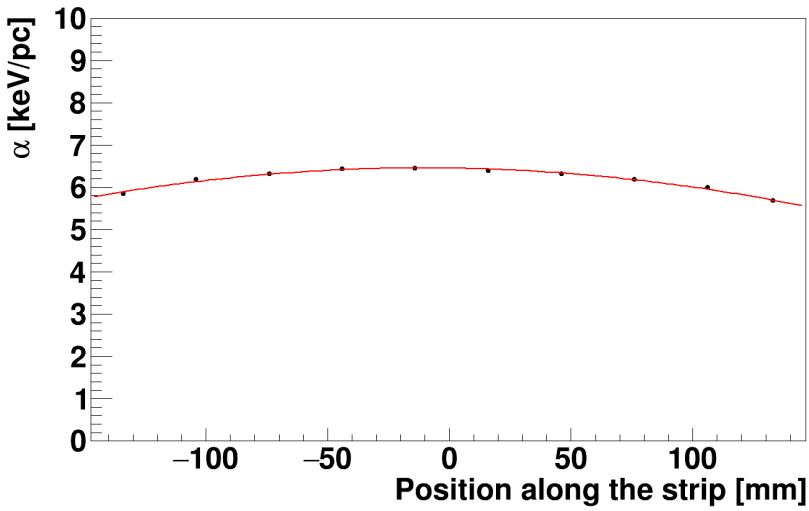

Figure 34: Scaling factor (α) between charge produced by photomutliplier and energy deposited in scintillator strip for 30 cm long strip.

It is so, due to the fact, that there are two contributions to the amount of light arriving at photomultipliers photocathode: attenuation of light inside scintillator and solid angle. The farther the scintillation position is from photomultiplier, the smaller the solid angle is and thus the fraction of light that reach photocathode without internal reflections inside scintillator. All other photons have to reflect multiple times and thus their path through scintillator is much longer than those which reach photomultiplier directly. For the long distances of interaction point from photomultiplier the attenuation contribution is dominant. When interaction position is very close to the photomultiplier window, solid angle for photons which can directly hit photocathode is much bigger and thus the contribution of solid angle dominates (see Fig. 35). This contribution strongly depends on interaction position which can be clearly seen in presented figure.

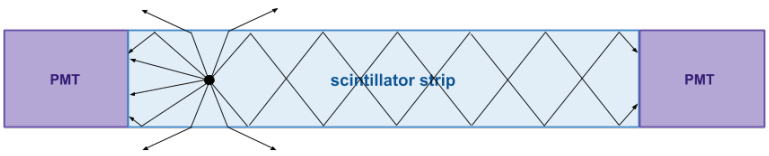

Figure 35: Pictorial representation of light transfer in the scintillator. The black dot represents the position of energy deposition inside the scintillator where photons are emitted from. Black arrows show a few exemplary paths of light inside. The closer to the photomultiplier the deposition occurs, the larger the solid angle seen by photons from the emission place.

To provide a calibration of energy needed for energy cut, a polynomial of second degree was fitted to each scintillator data. E.g. the red line in Fig. 34 follows equation:

$$\alpha = p_0 + p_1 * position + p_2 * position^2, \tag{22}$$

where $p_0 = (6.455 \pm 0.017)[\frac{keV}{pC}]$, $p_1 = (-7.78 \pm 1.3) * 10^{-4}[\frac{keV}{pC}/cm]$, $p_2 = (-3.69 \pm 0.18) * 10^{-5}[\frac{keV}{pC}/cm^2]$.

16

TIME AT THRESHOLD ESTIMATION

The method of calculating time at threshold is crucial in achieving a good time resolution. There are many solutions for finding the crossing of the signal curve with a certain voltage value. In case of signals acquired by the SDA unit, they are well probed and linear interpolation between points is enough to estimate the crossing of the signal with the threshold. Because the goal is to imitate a constant threshold or fraction discriminator, the first crossing of the threshold by the signal line is taken into account (see Fig. 36).

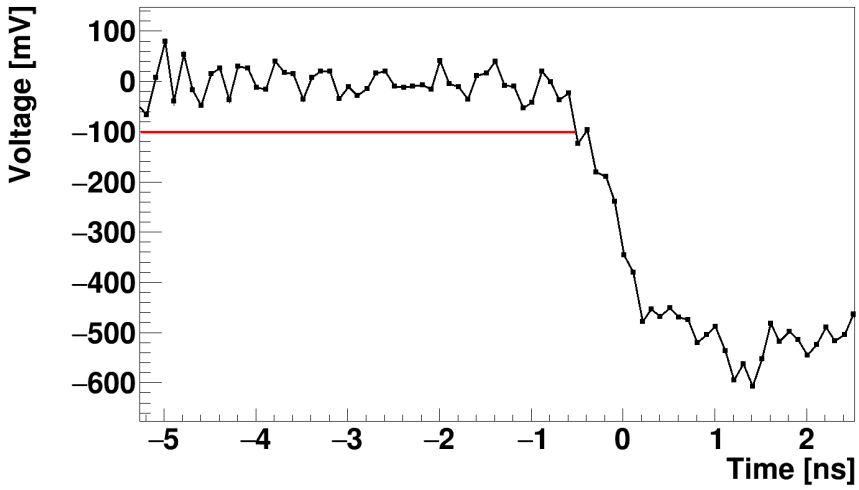

Figure 36: Example of how time at threshold is calculated. The red line shows the -100 mV threshold value and its point of crossing with the signal line, estimated as a linear interpolation between two points, is visible.

17

TIME OVER THRESHOLD

The J-PET scanner front end boards will not measure the charge generated by the photomultplier. The charge measurement is more time consuming than the measurement of signal crossing with the threshold, therefore in order to decrease the dead time of the J-PET, only the time will be measured. Hovewer it will be possible to estimate the charge of the signal by the measurement of its width. For this purpose a Time Over Threshold (TOT) technique is used [8]. In front-end boards, TOT will be measured at four, selectable, voltage levels. If those voltage levels are spaced evenly from each other, then one can estimate the charge by summing up all four TOT values (marked as an example in Fig. 37).

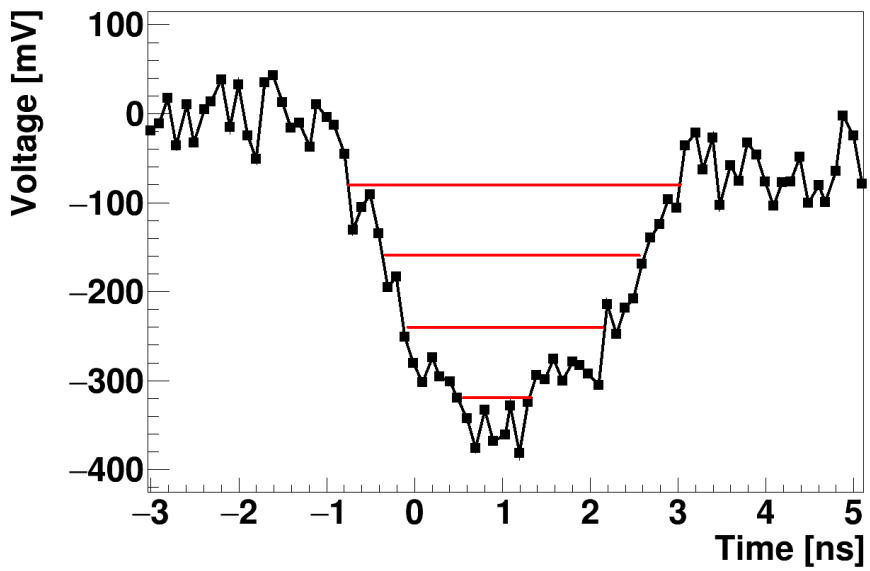

Figure 37: Example of measurement of four TOT values at one signal. Values at which measurement is performed are set at 80 mV, 160 mV, 240 mV and 320 mV.

The main concern is that the TOT dependence on charge is not linear and therefore, the TOT distribution is significantly different from the charge spectrum, as one can see by comparing Fig. 38 and Fig. 31.

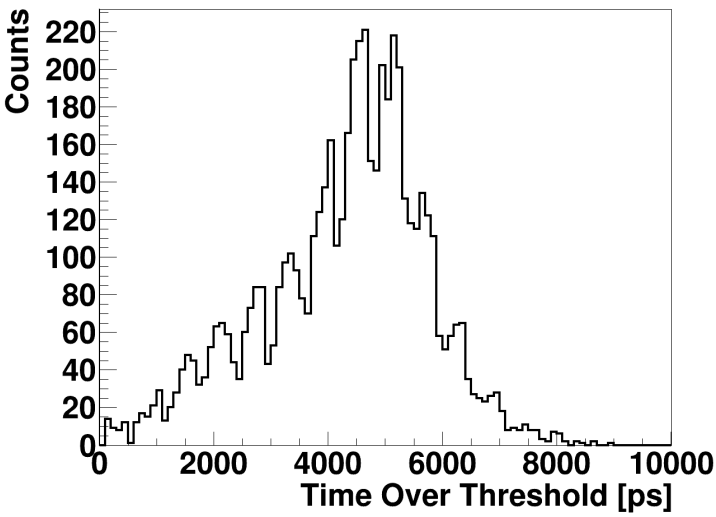

Figure 38: TOT spectrum obtained from experimental data. 5x19x300 mm^3 strips were irradiated at the central position. Measurement threshold was set to 80 mV. The maxima in the TOT spectrum correspond to the TOT values for signals when a given number of photoelectrons cross the measurement threshold.

To determine the TOT dependence on charge, a TOT distribution was calculated for small charge bins (see Fig. 39 and 40) and the mean value of the TOT distribution was taken for each charge bin.

The resulting dependence is presented for four photomultipliers, at the central position of irradiation, in Fig. 41. The dependence is, as expected, the same within uncertainity bars for all photomutipliers since the gains of the photomultipliers were matched, and same threshold was applied for the TOT calculation.

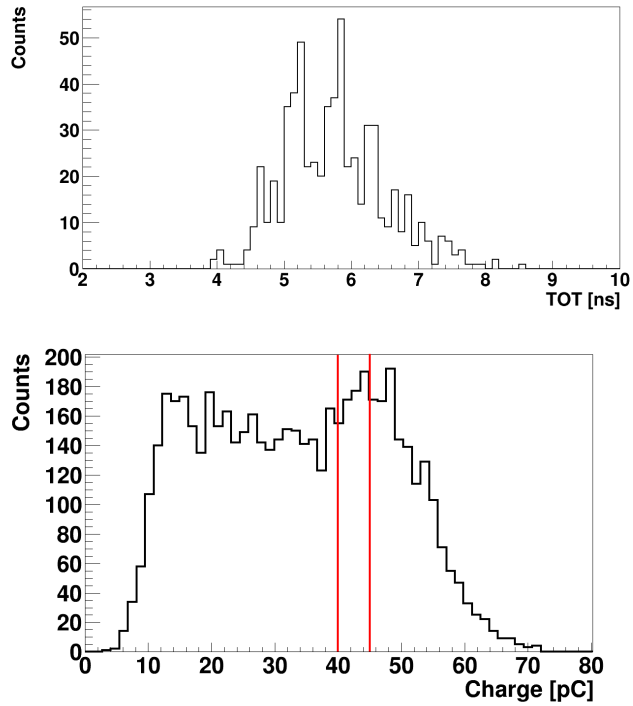

Figure 39: (top) TOT spectrum measured at 80 mV from 5x19x300 mm^3 scintillators for the charge bin shown in (bottom). (bottom) Charge spectrum for the central position of irradiation for 5x19x300 mm^3 scintillators.

The TOT dependence on charge was also investigated by the Authors of reference [63], but the proposed dependence of:

$$TOT = A + B * \sqrt{charge}, \tag{23}$$

is not followed by the points as shown in Fig. 42. The logarithmic function:

$$TOT = A + B * ln(charge), \tag{24}$$

results in a much better fit.

Fig. 43 shows the dependence of the TOT value as a function of the irradiation position and deposited energy. In case of high energy deposition (around 300 keV) the dependence is flat, while the lower the deposited energy the stronger the dependence becomes.

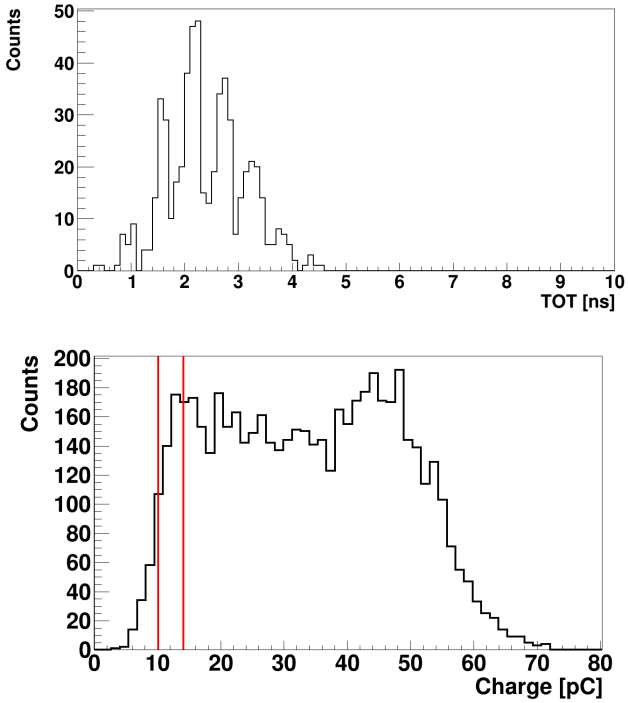

Figure 40: (top) TOT spectrum measured at 80 mV from 5x19x300 mm^3 scintillators for the charge bin shown in (bottom). (bottom) Charge spectrum for the central position of irradiation for 5x19x300 mm^3 scintillators.

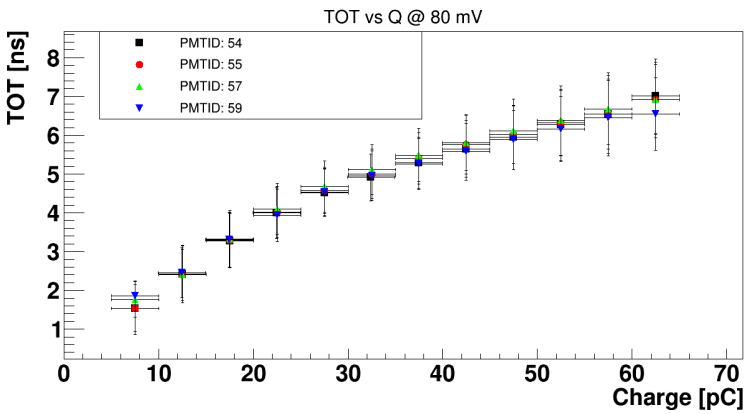

Figure 41: TOT measured at 80 mV for each of four tested photomultipliers with a 5x19x300 mm^3 scintillator. The photomultipliers had matched gains. The central position of the scintillator was irradiated.

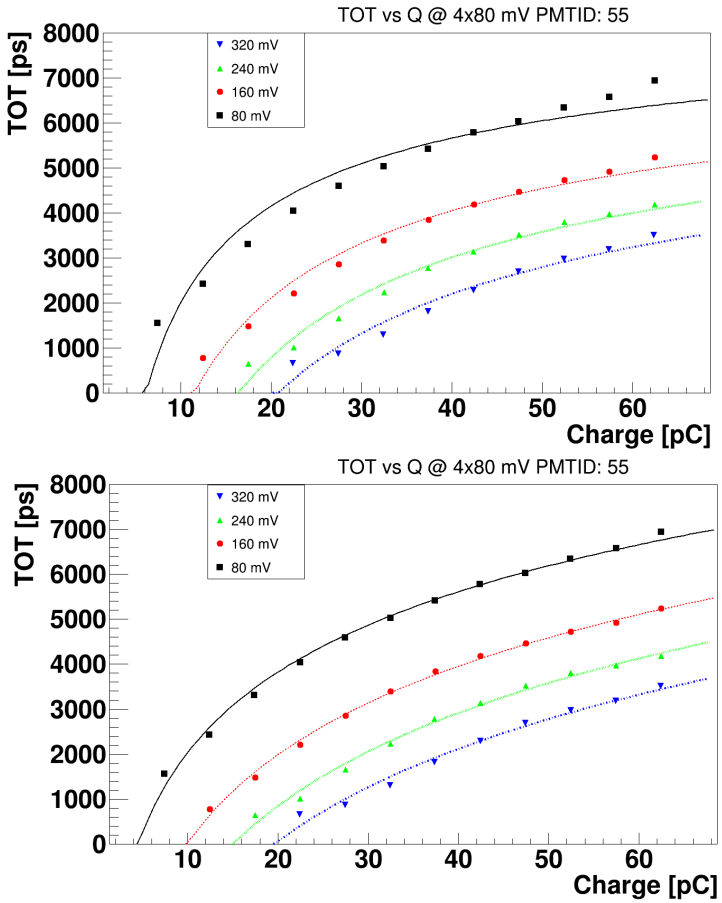

Figure 42: Comparison of fit using relation $TOT = A + B * \sqrt{charge}$ (top) and $TOT = A + B * ln(charge)$ (bottom) for four different thresholds. Logarithmic function describes the data points better.

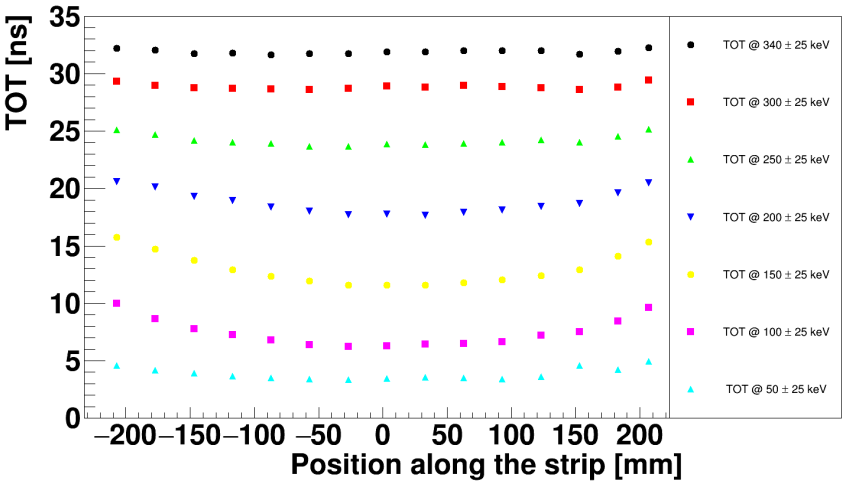

Figure 43: TOT calculated as sum from four thresholds and two photomultipliers from the same scintillator as a function of irradiation position. In the legend, markers for different deposited energy regions are noted.

18

CONVERSION FROM THE TIME TO THE VOLTAGE DOMAIN

Signals acquisited by the SDA unit are probed in the time domain (see Ch. 10) - the voltage of a signal is measured at selected time intervals (see Fig. 44 for a schematical explanation) and information about the time interval and voltage are saved in a file. Each annihilation event consists of two interactions of gamma quanta and each interaction produces signals at two photomultipliers connected to the scintillating strip. Since one signal contains roughly 500 points, then each event needs around 2000 points to be stored.

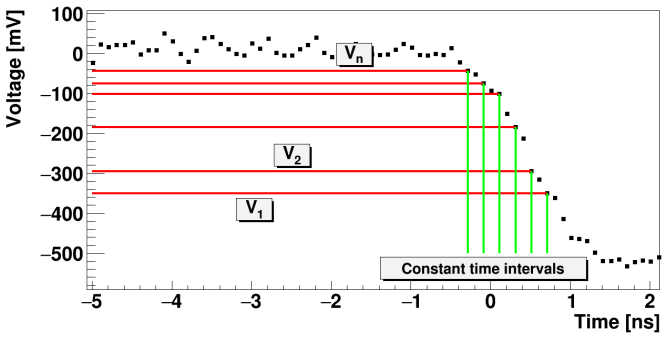

Figure 44: Pictorial representation of the time domain format. For better visibility only the region of leading flank of the signal is shown. At constant time intervals (green lines) a signal is probed and its voltage (V_1, ..., V_n) measured (red lines). For the clarity acquisition was designated only for a selected region and for every second point. Information about probing time and signal voltage at probing time is acquisited. Not only points corresponding to the signal are measured but also points that belong to the noise region before the signal rising flank will be acquired.

This format is not efficient to use, because most of the acquisited points belong to the noise region. Moreover such a measurement is not possible with Front End Electronic (FEE) boards, where only a few selected thresholds can be set, so any algorithms working with such data will not neccesarily be useful for signals measured with FEE.

To solve this problem a calculation of signal crossings with chosen constant threshold values was performed, mimicking a multi-level constant threshold discriminator. A more fine scan was done from 10 mV to 400 mV with a step of 10 mV while from 500 mV to 1000 mV a larger, 50 mV step was used (see Fig. 45).

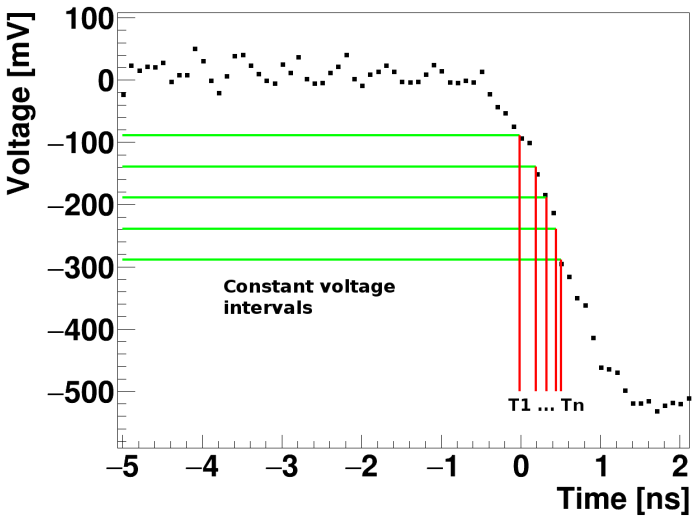

Figure 45: Pictorial representation of the voltage domain format. Using constant voltage intervals (green lines) the values of times when the signal crosses a particular threshold are measured (red lines). For clarity probing is indicated only for a selected region and for a few thresholds.

The application of probing in the voltage domain reduces the amount of points which hold potentially useful information from at least 500 (time domain) to 52 (voltage domain). To provide more information for the tests presented in this thesis not only selected times are saved, but also an information about the charge carried by the signals for each photomultiplier, energy depositions in modules and the modules energy resolutions. Data in the voltage domain is stored in the following format:

$$t_1^1, \cdots, t_N^1, t_1^2, \cdots, t_N^2, \cdots, t_N^4, \Delta E_1, \Delta E_2, Q_1, \cdots, Q_4, \alpha_1, \alpha_2, \beta_1, \beta_2, \quad (25)$$

where t_i^j denotes time determined for the j photomultiplier at the threshold V_i, which is calculated according to:

$$V_i = 10\text{mV} + i \cdot 10; \text{ for } 0 < i \leq 40, \quad (26)$$

$$V_i = 400\text{mV} + (i - 40) \cdot 50; \text{ for } 40 < i < 52,$$

ΔE_i and Q_i stand for the energy deposited in the $i - th$ scintillator and the charge from the $i - th$ photomultiplier, respectively, while α_i and β_i are fit constants described in Chapter 15.

Part V

TIME AND CHARGE MEASUREMENT METHODS

One of the goals of this work is to present the most optimal method for the measurement of 511 keV gamma quanta interaction time with the scintillator. Two potential solutions were investigated.

- constant multi-fraction board [J. Majewski, private comm (2013)];
- constant multi-threshold board [K. Lojek, M. Palka, private communication (2013-2015)];

The criteria which were taken into account were:

- best resolution of the time difference measured between two channels with the same settings;
- price per channel;
- power consumption ;
- size and ease of use;

The resolution of the time difference measurement between two channels of each board was studied by injecting a stable signal waveform from a signal generator, splitted passively into two channels at once.

Each of the boards was read by a Trigger Readout Board (TRB) [8, 64, 65] which are intended as a final step of signal proccesing in the J-PET scanner.

19

MULTI-LEVEL CONSTANT FRACTION BOARD PROTOTYPE

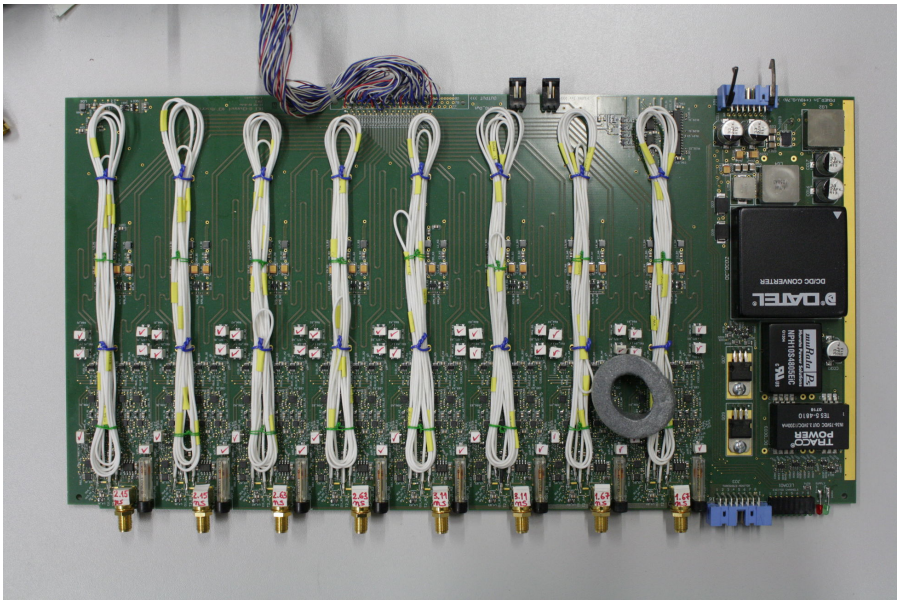

Figure 46: Multi-level constant fraction board picture, designed by J. Majewski. A single board has dimensions 190 x 365 mm^2 and four pairs of channels. For each pair a different constant fraction was set.

The multi-level constant fraction board possessed four pairs of input channels, each for a different set of fractions. Each input channel provided four outputs. The board allowed the measurement of signal time at a selected fraction for a pair of signals. Fraction level combinations could only be changed by the mechanical shortening of delay cables (white cable at Fig. 46). The investigated board worked well with the generated signals, achieving a 70 ps (σ) time resolution (see Fig. 47). It could be possibly used for experiments with different types of particles impinging the detector setup. Unfortunatelly the board was constructed from expensive components and its power usage was very high (about 2.76 W per channel), which would lead to higher costs of production as well as maintance costs.

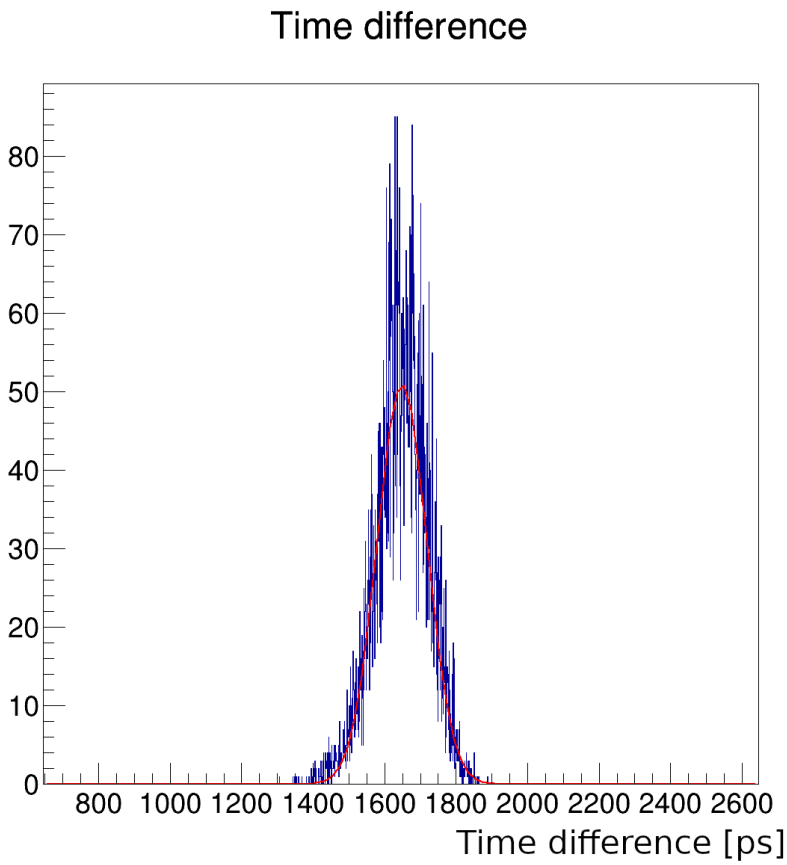

Figure 47: Time difference spectrum measured between two best channels in the board. Signals were generated by a signal generator and split passively to both channels. The superimposed line shows a Gaussian fit resulting in $\sigma = 70ps$.

Moreover, signals from the plastic scintillator strips consist of a small number of photoelectrons (about 280 [45]) and thus are ragged at the maximum and trailing flank, leading to the deterioration of the constant fraction determination and hence were worsening the time resolution. Due to the above disadvantages the possibility of using multi fraction board was rejected, although it could be used in other experiments with much smoother signal waveforms.

20

MULTI-LEVEL CONSTANT THRESHOLD BOARD PROTOTYPES

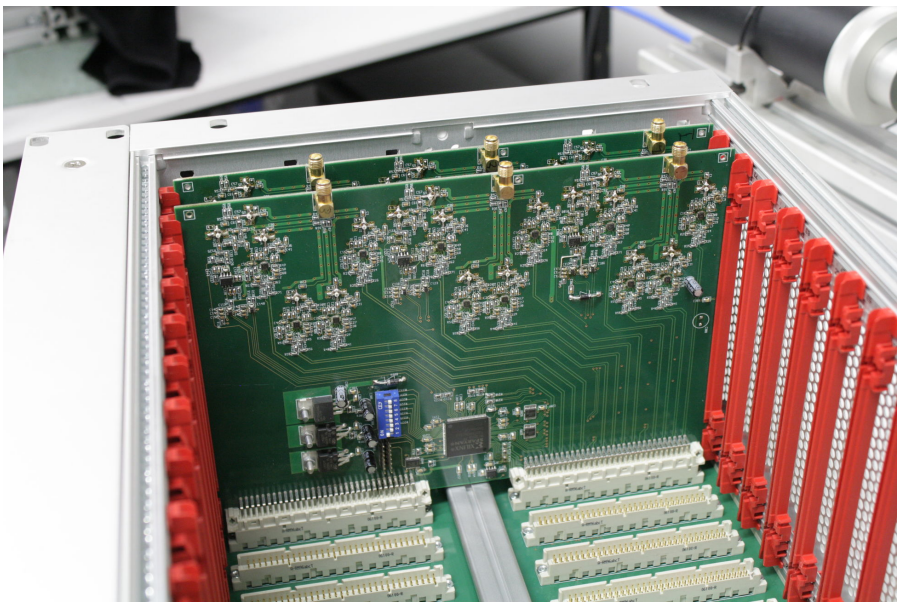

Figure 48: Multi-level constant threshold board picture placed inside the holder crate, design by K. Łojek. A single board has dimensions of 190 x 245 mm^2 and has 3 input channels. Each board had to be put inside a readout crate.

The multi-level constant threshold board provided three input channels and five outputs per each. Four of them measured time at set threshold level, while the last one was supplying charge information. All five thresholds could be changed by communication with the FPGA on the board. The time resolution measured with signals from the signal generator was better than 30 ps (σ) and tests with a two strip setup (30 cm long scintillators) revealed initial time difference resolution (σ) equal to 190 ps, as presented in Fig. 49.

This board was considered to be a step in the right direction, since it provided control over thresholds, information about the energy deposited in the scintillator in TOT form as well as the reduction of maintenance costs, size and an improvement of time resolution. Unfortunately the board components price and the power needed (about

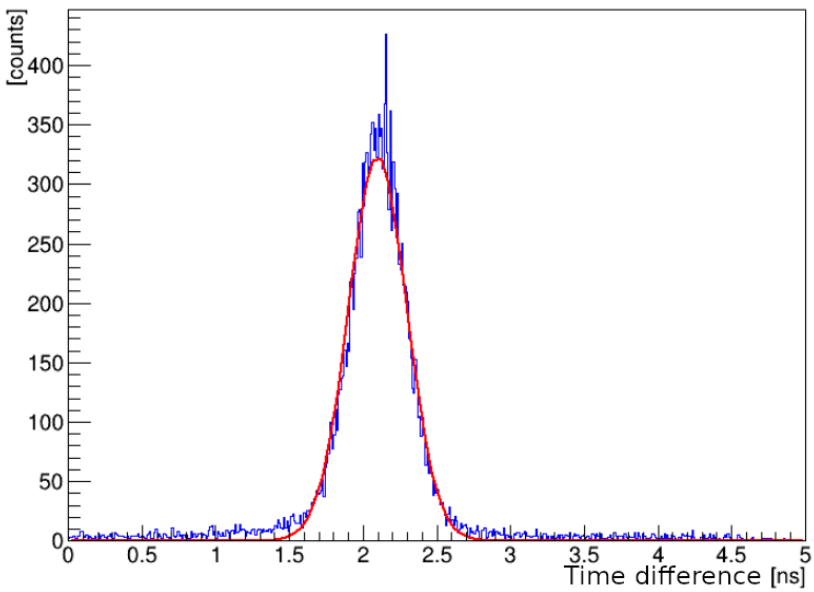

Figure 49: Time difference spectrum measured with a multi-level constant threshold board with signals originating from a 30 cm long two strip setup. No data preselection was performed and thus the result should be treated as the worst case scenario. The superimposed line shows a Gaussian fit resulting in $\sigma = 190ps$.

1.5 W per channel) to run it were also too high to consider it as a final front end board for the J-PET detector. Still, further investigations were performed to find a more cost effective solution.

The fact that previous board signals still needed to be digitized by a seperate device was not desired due to the amount of space needed by the front-end electronics. The next generation of boards (photo in Fig. 50) were developed in such a way that the board was a part of a digitizing setup and it was splitting the signals into four (see Fig. 51) and feeding the signal directly to the TRB, which performed a measurement of time at selected threshold [8, 66]. Such an approach saved not only space, but also power supply equipment needed, since the front-ends could draw power from their mother boards (in this case TRB).

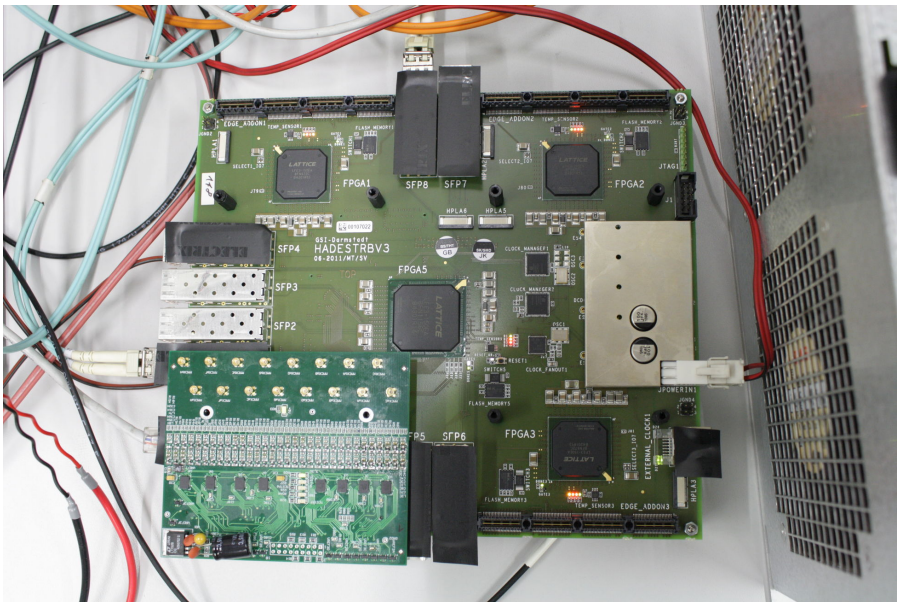

Figure 50: Next generation of multi-level constant threshold board placed on the TRB. Four of such boards could be connected to one mother board, design by M. Pałka. A single board has dimensions of 105 x 90 mm^2 and has 16 channels. Four of such boards can be connected to one TRB.

This generation of front-end boards has been successfully used in measuring signals from a small barrel prototype of the J-PET scanner [34]. The studies of time difference measurement resolution presented in Fig. 52 indicate that in case of fast signals from scintillators the board will have very good timing properties around 20 ps (σ). Additionally, the power needed to supply one channel was much smaller than for previous boards - about 0.25 W of power was needed per channel.

Due to the fact that studies of front end boards performed by the J-PET group concentrated on constant threshold time measurements, further on in this work only this approach will be studied.

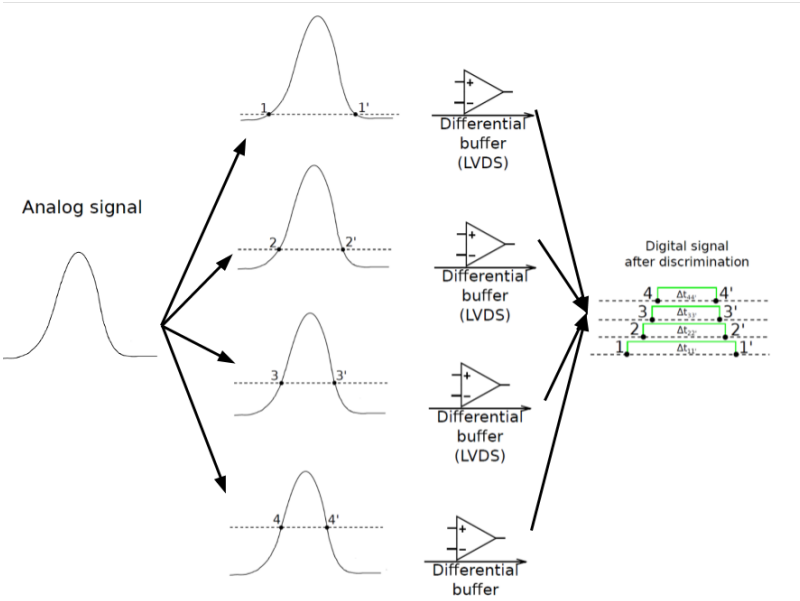

Figure 51: The graphical explanation of signal sampling. The signal is divided into four and piped to channels with different thresholds marked with numbers from 1 to 4 and digitized by a differential buffer. A rectangular signal is produced, its width is equal to the TOT on a selected threshold [8]. Numbers with apostrophes indicade the falling edge of the digitized signal, which appears when signal crosses the threshold again, towards lower values.

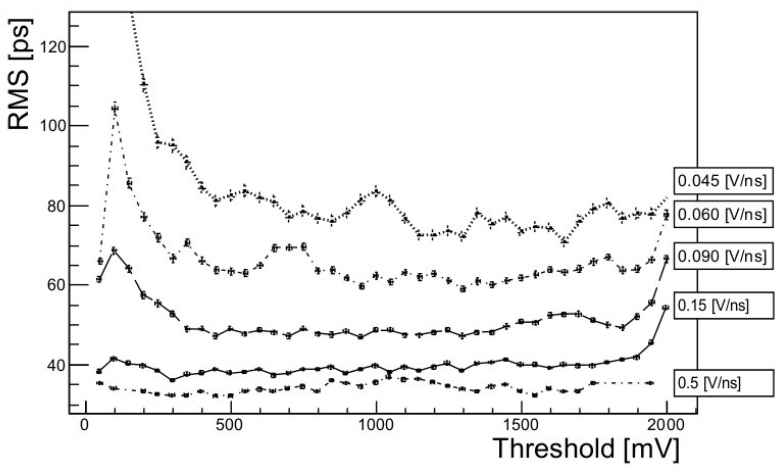

Figure 52: The Root Mean Square (RMS) of the time difference as a function of the threshold level, between the generated, passively split signal at two different channels of the board. Lines indicate different slope rates for the generated signals. Figure adapted from [8].

Part VI

OPTIMISATION OF THE J-PET PARAMETERS

21

THRESHOLD OPTIMISATION AT THE CENTER POSITION

To optimise the threshold value, at which the signal arrival time is measured, a scan from 10 mV up to 1000 mV was performed on signals originating from the irradiation at the center of the scintillator. For each threshold, the time difference distribution was determined. Then to each time difference distribution a Gaussian function was fitted and its sigma value extracted, which is further considered to be a measure of the time resolution of a given detection module.

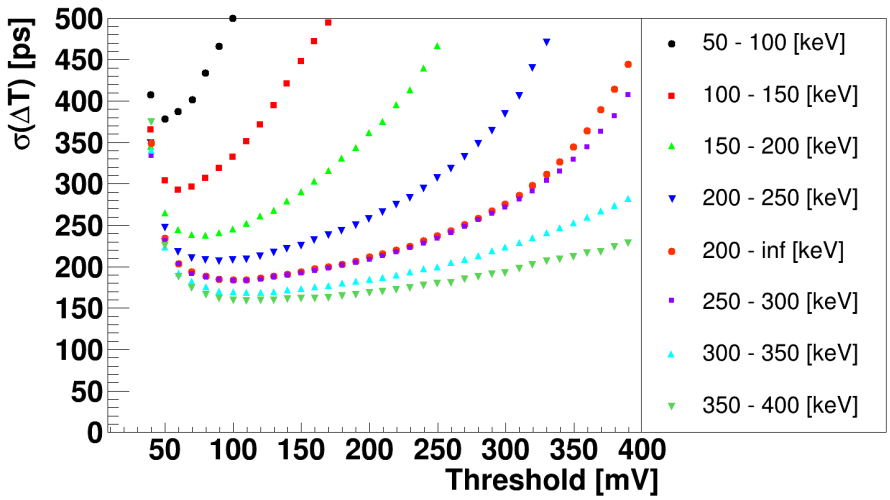

Figure 53: The time resolution as a function of the threshold applied to signals generated by the photomutlipliers from the J-PET detection module (30 cm long). Different markers represent different deposited energy regions as noted in the legend. Additionally results for energy losses larger than 200 keV (200 – inf [keV]) are presented.

As can be seen in Fig. 53 time resolution has a minimum as a function of the threshold used for time measurement. The shape of the dependence and the sharpness of the minimum depends on the energy region and best achievable time resolution is improving with increasing energy deposition. The threshold which is needed to obtain such a resolution is also rising with higher energies. This comes from the fact that each signal is built out of single photoelectron sig-

nals and its rising flank shape is improving when the photoelectron statistics is large. Large statistics of photoelectrons can occur when higher energy depositions will take place and therefore more light is produced in the scintillators.

The time resolution obtained for an energy cut at 200 keV (red cirles) has almost the same values as the time resolutions at 200-250 keV energy region (purple squares). The optimal threshold for time measurement is further estimated as the minimum of the function in Fig. 53 for the case of energy cut at 200 keV. This approach can be redone for each detection module. The time measurement at this point does not contain any calibrations since they are not influencing the resolution outcome (they only shift the time difference distribution mean). Time measurement corrections, such as the walk-effect correction, could improve resolution, but they should not change the optimum threshold value, and because of that an optimum threshold for each scintillator will be applied in next Chapters.

22

OPTIMISATION OF SUPPLY VOLTAGE

To determine the optimal working voltage for photomultipliers a series of measurements was performed on a 14x14x20 mm^3 scintillator. Short scintillators were used in order to neglect the influence on time resolution originating from the effects of light transportation in the scintillator strip. The voltage was set to values from 1200 V to 1600 V with a 50 V step on one of the photomultipliers while the other one was matched to have the same gain. The middle of the scintillator was irradiated with a sodium source placed inside the collimator. For each voltage an optimal threshold was extracted as the one for which the best time resolution is achieved with a cut on the deposited energy set to 200 keV.

The optimal threshold for each voltage is shown in Fig. 54. As expected optimal threshold value is higher for higher voltage values since amplitude of signals is rising.

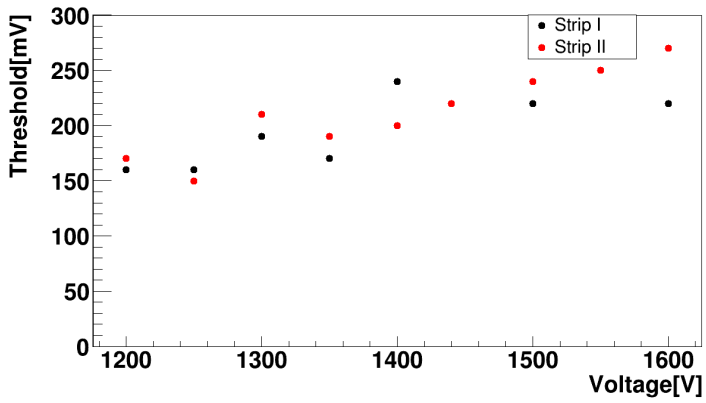

Figure 54: Dependence of optimal threshold on the voltage supplied to the photomultiplier. Note that second photomultiplier connected to the strip was set to the same gain according to its gain curve. An energy cut at 200 keV was applied to the data. Since the signal amplitude is larger for larger voltage values, the optimal threshold is also larger.

To decide on the optimal voltage value one has to consider two parameters of each detection module - its time and energy resolutions. In Fig. 55 a dependence of time resolution at the optimal threshold

for different supply voltages is presented. As can be seen with higher voltage the time resolution improves up to around 1440 V and reaches a value of about 100 ps.

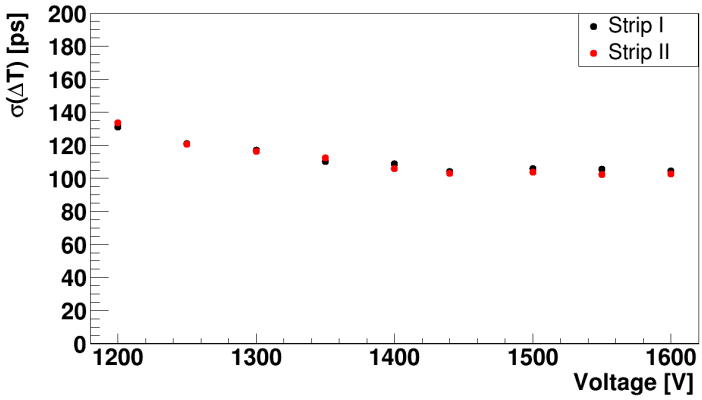

Figure 55: Time resolution at optimal threshold as a function of voltage supplied to the photomultiplier.

Since the energy resolution does not depend on the voltage applied to the photomutlipliers as presented in Fig. 56 it allows one to chose an optimal supply voltage solely based on time resolution behaviour. Thus a voltage of 1440V is further selected as the optimal one and in each measurement its value will be set on one photomultiplier while all three other will be matched with gain by means of their respective gain curves.

Such an approach can be used to optimise voltages for each detection module in the J-PET scanner prototype by performing simultanoeus voltage scans with a radioactive source placed inside the collimator.

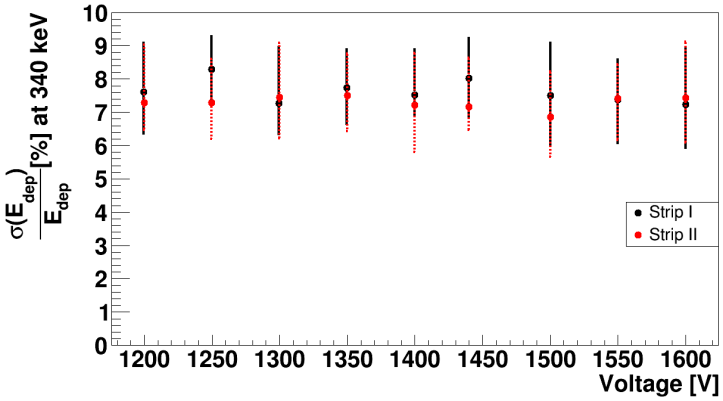

Figure 56: Dependence of the energy resolution (from Eq. 19) at 340 keV energy loss on the voltage supplied to photomultipliers. Points and errors on the plot were calculated according to description in Chapter 15.

23

IMPACT OF ENERGY DEPOSITION ON TIME RESOLUTION

As proved in previous chapters the time resolution depends on the threshold applied to signals and the voltage which supplies photomultipliers. Another factor that will influence time resolution is deposition of energy inside scintillator. In Fig. 57 the dependence of optimal threshold on the selected energy region is presented. For each energy region the optimal threshold was found out as described in Chapter 21. It appears that the optimal threshold changes proportionally with the rise of the deposited energy. This is to be expected since with rising energy deposition more light is produced in the scintillators thus signals generated by the photomultipliers will be higher.

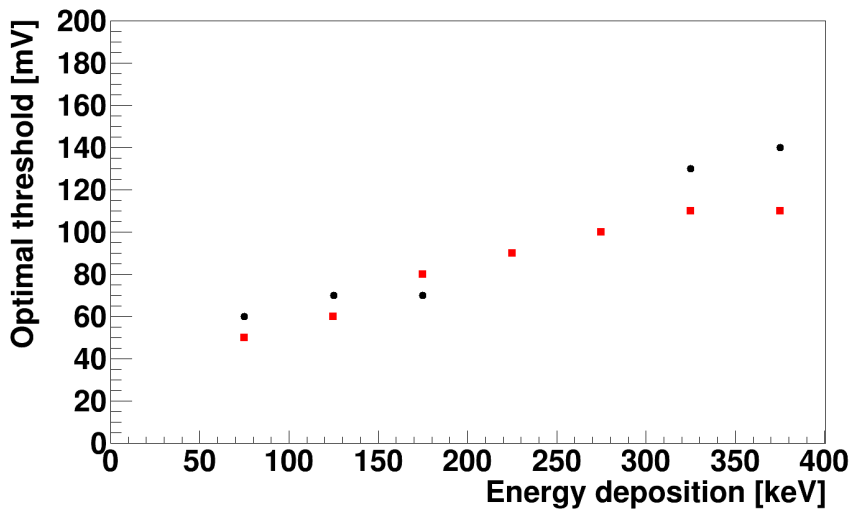

Figure 57: Example dependence of optimal threshold on energy deposition for a 5x19x300 mm^3 strip for the central position of interaction. Points indicate results obtained for 50 keV intervals (e.g. first point corresponds to energy loss range 50 - 100 keV). The two marker types correspond to results from both investigated strips.

Thus with the increase of energy loss the number of photoelectrons in the signal is increasing and it improves the time resolution as can be seen in Fig. 58.

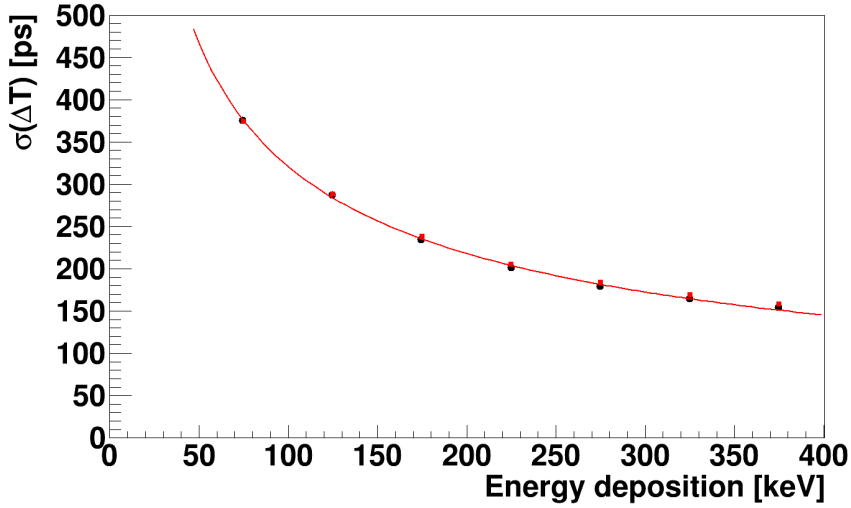

Figure 58: Example dependence of the time resolution of the single module for a 5x19x300 mm^3 strip for the central position of interaction. Points indicate results obtained for 50 keV intervals (e.g. first point corresponds to energy loss range 50 - 100 keV). The two marker types correspond to results from both investigated strips, note that the points are almost in the same places. Then the time resolution was calculated at the optimal threshold. Both strips from the two module prototype were investigated. The red line indicates fitted function to points originating from one of the tested scintillattors: $y = \frac{a}{\sqrt{x}} + b$, where $a = 3512 \pm 47\text{ps}\sqrt{keV}$ $b = -30.3 \pm 3.6$ ps.

Part VII

TIME CALIBRATION

24

TIME OFFSET

The time measured at selected thresholds contains offsets due to delays of signals in cables and electronics. In order to determine these offsets one can collect data for irradiation of scintillator at its center.

The difference between times of signals measured at opposite ends of the strip should be constant and may be expressed as:

$$t_A - t_B = t_{offsetAB}. \tag{27}$$

In order to correct for this offset the following change of times can be performed:

$$t_A^{'} = t_A, \tag{28}$$

$$t_B^{'} = t_B + t_{offsetAB}. \tag{29}$$

This adjustment will produce time differences at zero value if the interaction took place at the center of the strip, because:

$$t_A^{'} - t_B^{'} = t_A - t_B - t_{offssetAB} = 0. \tag{30}$$

As mentioned before, one can determine the $t_{offsetAB}$ value by irradiating the center of the strip. The mean value of the $t_A - t_B$ spectrum will be equal to $t_{offssetAB}$.

25

TOF OFFSET

The next correction is needed in order to account for the TOF offset, called further $T_{toffset}$. The difference between the time of interactions in different strips is defined as:

$$TOF = T'_{AB} - T'_{CD}, \tag{31}$$

where T'_{AB} stands for the time of interaction in a strip with photomultipliers A and B and similarly T'_{CD} stands for time of interaction for a strip with photomultipliers C and D (see Fig. 59).

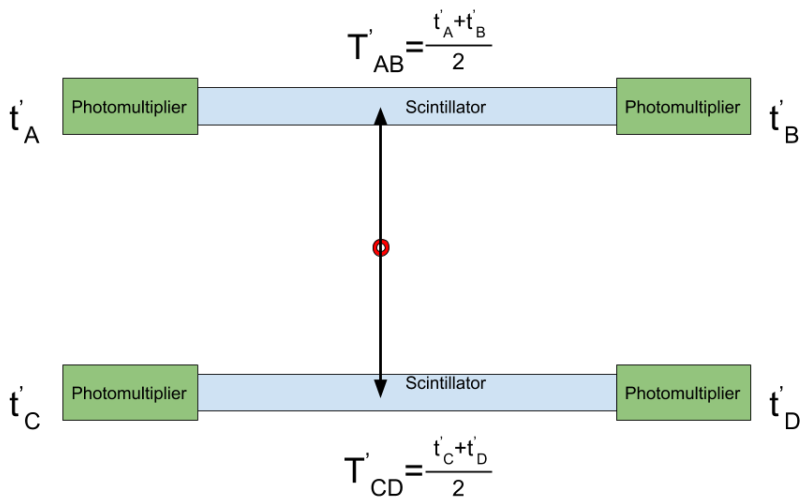

Figure 59: Pictorial illustration of times of signal arrival measured by the photomultipiers and interaction times of gamma quanta with the scintillators.

If the annihilation took place in the middle, between two detection modules, TOF should be equal to zero. Again, due to delays induced by electronic devices one observes that TOF can be different from zero:

$$T'_{AB} - T'_{CD} = T_{toffset}. \tag{32}$$

As before one can perform the following correction:

$$T''_{AB} = T'_{AB}, \tag{33}$$

$$T''_{CD} = T'_{CD} + T_{toffset}. \tag{34}$$

Further, the time of interaction can be expressed as:

$$T''_{CD} = \frac{t''_C + t''_D}{2}, \tag{35}$$

which leads to a correction of t_C and t_D:

$$t''_C = t_C + T_{toffset}, \tag{36}$$

$$t''_D = t_D + T_{toffset} + t_{offsetCD}. \tag{37}$$

Applying all three corrections together one should perform the following adjustments to the calculated times at thresholds:

$$t''_A = t_A, \tag{38}$$

$$t''_B = t_B + t_{offsetAB}, \tag{39}$$

$$t''_C = t_C + T_{toffset}, \tag{40}$$

$$t''_D = t_D + t_{offsetCD} + T_{toffset}. \tag{41}$$

Using variables t''_A, t''_B, t''_C and t''_D one will obtain for the measurement at the source placed in the center:

$$t''_A - t''_B = 0, \tag{42}$$

$$t''_C - t''_D = 0, \tag{43}$$

$$T''_{AB} - t''_{CD} = 0. \tag{44}$$

Further on in the analysis of the data values, times t''_A, t''_B, t''_C and t''_D are used. The TOF still needs to be corrected for the walk effect.

26

WALK EFFECT

26.1 TIME WALK CORRECTION BASED ON CHARGE

While measuring time at constant threshold, signals with higher amplitude will cross the threshold earlier than those with a smaller one, even if they originate from the same moment of time. Such a deviation of measured time, dependent on signal height, is called the walk effect.

In case of the J-PET, where the Compton spectrum is wide and so is the spectrum of signal amplitudes, one expects the deterioration of the time resolution of detection modules due to this effect. Therefore the walk effect influence was studied for a pair of strips. Data were collected by irradiating the center of the strips using a collimated source placed at the center between strips. Data set was first filtered with an energy cut at 200 keV (see Chapter 15 for details on energy calculation) and the optimal threshold was used.

Generally, one expects that the time measured at a selected threshold can be expressed as [67]:

$$t = t^{'} + \frac{\alpha}{\sqrt{Q}} \tag{45}$$

where t is the time measured at threshold by constant threshold board, $t^{'}$ is the time without walk influence, Q is the charge of the measured signal and α is a coefficient which can be determined.

The difference Δt between the times of arrival of the signal from the left t_L and the right t_R photomultiplier measured at a selected threshold can be expressed as:

$$\Delta t = t_L - t_R = t_L^{'} - t_R^{'} + \alpha(1/\sqrt{Q_L} - 1/\sqrt{Q_R}), \tag{46}$$

where $t_L^{'}$ and $t_R^{'}$ denote those times without walk effect influence, α is a constant parameter and Q_L and Q_R denote the charge at the left and the right photomultiplier signal, respectively.

Analogically TOF is equal to:

$$TOF = (t_{L1} + t_{R1})/2 - (t_{L2} + t_{R2})/2 = \\ (t'_{L1} + t'_{R1})/2 - (t'_{L2} + t'_{R2})/2 \\ + \frac{\alpha}{2}(1/\sqrt{Q_{L1}} + 1/\sqrt{Q_{R1}} - 1/\sqrt{Q_{L2}} - 1/\sqrt{Q_{R2}}) \quad (47)$$

where indices 1 and 2 denote the strip number. In Fig. 60 a dependence for TOF values is presented before and after walk correction. One can see that the tilt of the TOF distribution is removed after application of time walk correction.

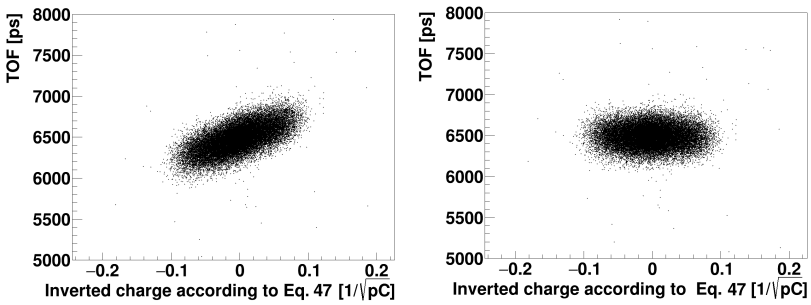

Figure 60: TOF dependence on the inverted square of the charges (see Eq. 47) before (left) and after (right) walk correction.

In Fig. 61 an application of walk correction to the time difference spectrum from one of the scinitllator strips is presented. The σ value of measured spectrum improves from 185 ps to 175 ps. In Fig. 62 the effect of this correction on the TOF spectrum is presented. An improvement from $163ps$ to $126ps$ is observed. In order to improve the scanner resolution one needs to apply the walk correction to the measured time difference and TOF seperately. The α coefficients from Eq. 47 and 46 were determined for the central position only and then applied to quantities measured from whole scintillator.

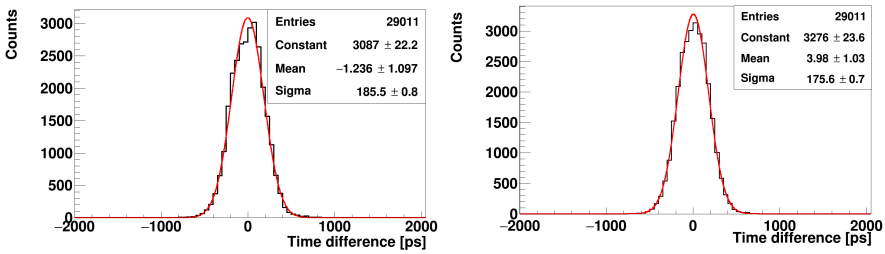

Figure 61: Time difference spectra before (left) and after (right) walk correction. A Gaussian function was fitted to each distribution.

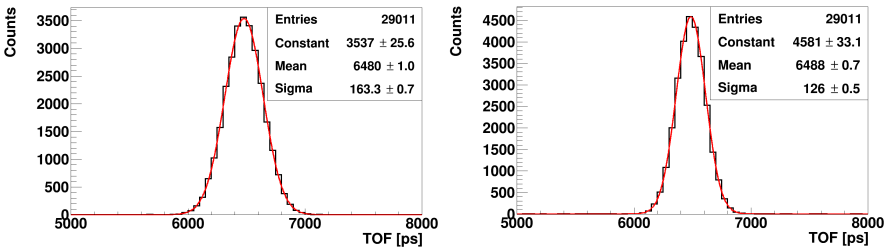

Figure 62: TOF spectra before (left) and after (right) walk correction. A Gaussian function was fitted to each distribution.

26.2 TIME WALK CORRECTION BASED ON TOT

Since it will be impossible to measure the charge by J-PET electronics, a test of the walk correction based on TOT was neccessary. Two hypotheses were tested: correction based on $1/TOT$ and $1/\sqrt{TOT}$. Where TOT is calculated as:

$$TOT = \sum_{side=A,B} \sum_{thr=1}^{4} TOT_{side,thr} \tag{48}$$

where, A, B denote the left and the right photomultipier and subscript thr enumerates the selected threshold.

In the left panels of Figs. 63 and 64 a TOF spectrum as a function of $\frac{1}{TOT}$ and $\frac{1}{\sqrt{TOT}}$ is presented. In the right panels the TOF spectrum after the application of the walk correction based on the respective dependence is shown. No significant difference is observed between the two utilised approaches, in both cases an improvement from 163 ps to 130 ps is achieved. Which is only a few ps worse than the result obtained when the correction based on charge is applied.

In the end the resolution obtained by applying the walk correction either based on charge or on TOT provides nearly the same result. This means, that the J-PET scanner can successfully use TOT method to make a correction for walk effect.

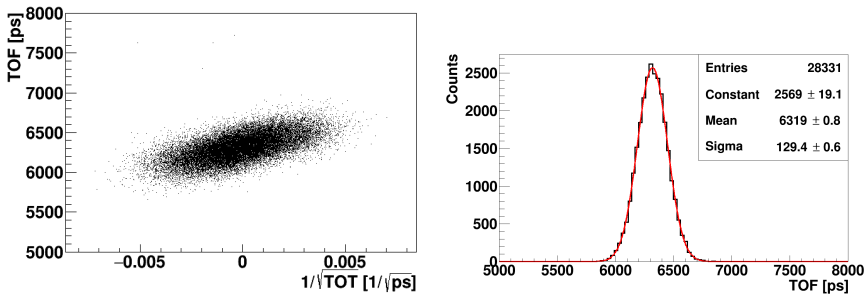

Figure 63: (left) TOF dependence on inverted square root of TOT before correction. (right) TOF spectrum after applying the correction to walk based on inverted square root of TOT.

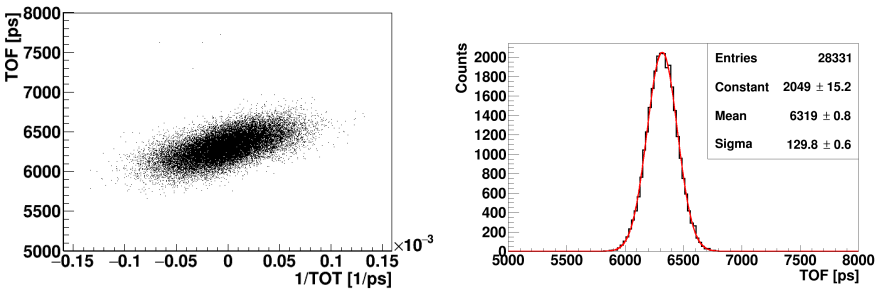

Figure 64: (left) TOF dependence on inverted TOT before correction. (right) TOF spectrum after applying the correction to walk based on inverted TOT.

Part VIII

IMAGE RECONSTRUCTION

27

HIT POSITION ESTIMATION

A hit position (point of gamma quantum interaction) along the scintillator strip may be approximately determined based on the time difference of light signal arrival to the left and right photomultipliers using the following formula:

$$z = \frac{\Delta t \cdot v_{eff}}{2}, \tag{49}$$

which may be derived from the relation:

$$\Delta t = (t_R - t_L) = t_{hit} + \frac{L - z}{v_{eff}} - t_{hit} - \frac{z}{v_{eff}} = \frac{-2z}{v_{eff}} + C, \tag{50}$$

where z is the hit position along the scintillator (see Fig. 65 for a pictorial representation), Δt is the time difference between signal arrival to the right t_R and left t_L side of the scintillator, L denotes its length, v_{eff} stands for the effective velocity of light inside scintillator and C is a constant.

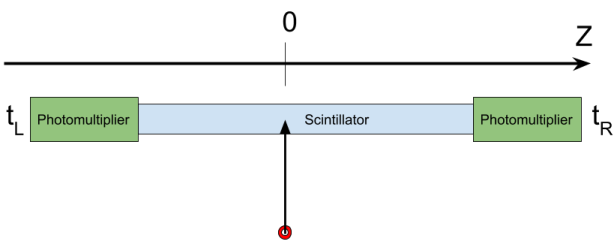

Figure 65: Pictorial representation of velocity determination. The source placed in a lead collimator was irradiating the scintillator at different z values.

The effective light signal speed along a scintillator strip (v_{eff}) is smaller than the speed of light in the scintillator medium because most photons do not travel to the photomultipliers directly but rather undergo many internal reflections, and because the refractive index of the plastic scintillator is greater than 1 and equals to 1.58 [27]. In order to determine the effective light signals speed in the tested

Table 7: Effective velocity of light inside a 5x19x300 mm^3 strip for a few different values of thresholds used for time determination.

Threshold [mV]	Velocity [cm/ns]
80	11.80 ± 0.04
120	11.40 ± 0.04
160	11.06 ± 0.05
200	10.78 ± 0.05

scintillator the time difference Δt was determined as a function of the irradiation position z, and v_{eff} was extracted by fitting a straight line to the experimental points as shown in Fig. 66. Since the value of the effective velocity depends on applied threshold as presented in [52], velocity was estimated at optimal thresholds for each scintillator. In Tab. 7 values of effective velocity for different threshold values are gathered. The smaller is the applied threshold the higher the value of the effective velocity.

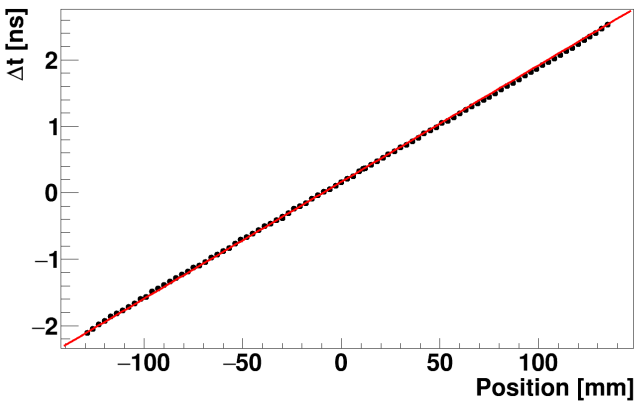

Figure 66: Dependence of the time difference spectrum mean value, obtained from a Gaussian fit, on the position of irradiation for a 5x19x300 mm^3 strip with the time measurement threshold set to 120 mV. A line ($y = p_0 + p_1 * x$) was fitted to the data, with $p_0 = 0.1657 \pm 0.0051$ ns and $p_1 = 0.01754 \pm 0.00006 \frac{ns}{cm}$. The velocity for this threshold is equal to $11.40 \pm 0.04 \frac{cm}{ns}$.

28

NAIVE RECONSTRUCTION

PET scanners use various image reconstruction algorithms to improve image quality [68, 69, 70] such as Filtered Back Projection (FBP) or Maximum Likelihood Expectation Maximization (MLEM), but since the J-PET scanner has a different geometrical arrangement, a new method for reconstruction was needed. In the following Chapters initial image information will be presented, then the reconstruction algorithm will be discussed and the images of the source placed in few different positions between the two strips will be evaluated and the spatial resolution of the obtained images will be determined.

A scatter plot of the annihilation points reconstructed initially by data analysis is called the Raw Image. The Raw Image is then used as input for reconstruction algorithms. In case of two strip prototype studied in this thesis all points are gathered in the 2D plane. In order to test the reconstruction capabilites of the J-PET scanner a radioactive source was placed in several positions between the two modules (see Chapter 11 for more details).

For each registered pair of gamma quanta, originating from an annihilation, three variables are determined: $z_u, z_d, \Delta l$, which denote hit position along the two strips (up and down) and the position of annihilation along the LOR line, respectively. From them one can reconstruct the emission position and angle ϕ defined in Fig. 67:

$$\tan\phi = \frac{z_u - z_d}{2R}, \tag{51}$$

$$y = -1\frac{\Delta l}{\sqrt{1+\tan^2\phi}}, \tag{52}$$

$$z = \frac{1}{2}(z_u + z_d + 2y\tan\phi), \tag{53}$$

where z, y are emission point coordinates, and the ϕ angle is measured from the Y axis as presented in Fig. 67.

To determine z_u, z_d one can use the time of arrival of light at the left and right end of the scintillator:

$$z_j = (t_{j_{left}} - t_{j_{right}})\frac{v_{eff}}{2}, \tag{54}$$

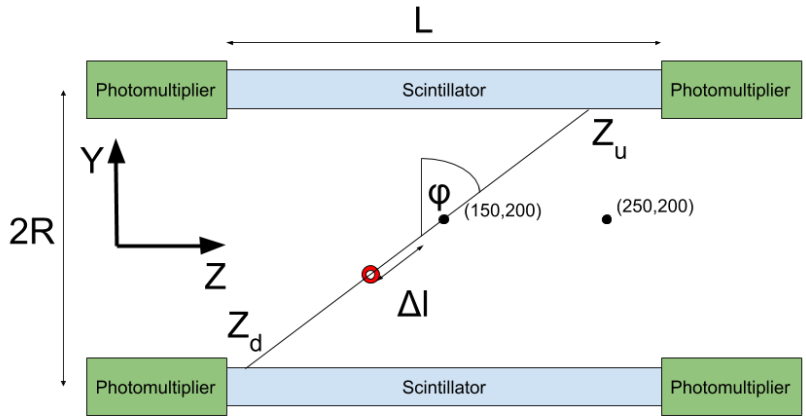

Figure 67: 2D-strip detector geometry. L denotes the length of the scintillator, $2R$ stands for the distance between two strip centers, ϕ denotes angle between LOR and Y axis, the red dot symbolises the annihilation point, Δl is distance of the annihilation point from the center of the LOR. Black dots with coordinates illustrate two positions for which annhilation points are presented in Figs. 68 and 69.

where z_j is the hit position for the jth strip (either up or down) while $t_{j_{left}}$ and $t_{j_{right}}$ denote the time of arrival of the signal at the left and the right end of jth scintillator strip respectively. v_{eff} denotes the effective speed of light in the scintillator strip with selected dimensions.

Calculation of Δl can be performed using TOF method:

$$\Delta l = TOF\frac{c}{2}, \tag{55}$$

where c denotes speed of light and TOF can be expressed as:

$$TOF = \frac{t_{u_{left}} + t_{u_{right}}}{2} - \frac{t_{d_{left}} + t_{d_{right}}}{2}, \tag{56}$$

where $t_{u_{left}}$, $t_{u_{right}}$ denote time measured by the left and right photomultiplier of the upper scintillator respectively. Analogically $t_{d_{left}}$, $t_{d_{right}}$ denote time measurements for the lower scintillator.

Exemplary raw images are shown in Figs. 68 and 69.

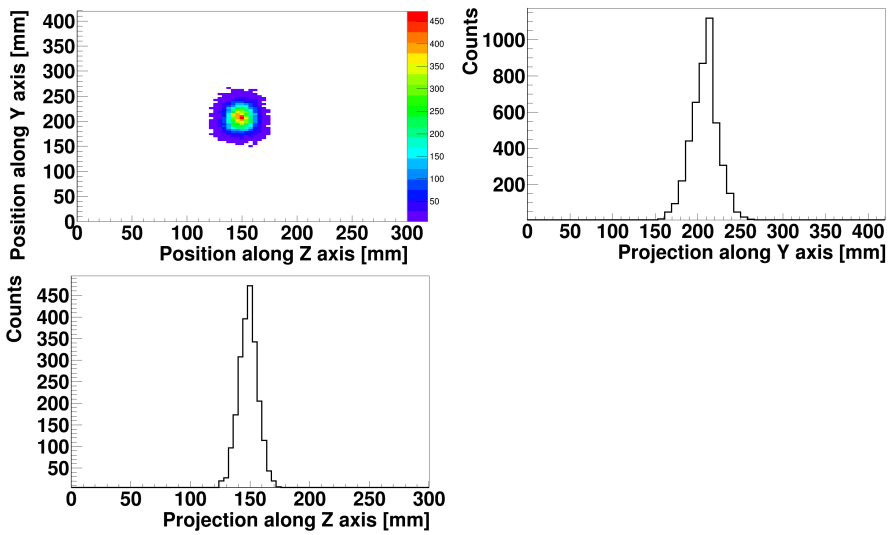

Figure 68: Raw image for the source placed in the central position between two 5x19x300 mm^3 modules.

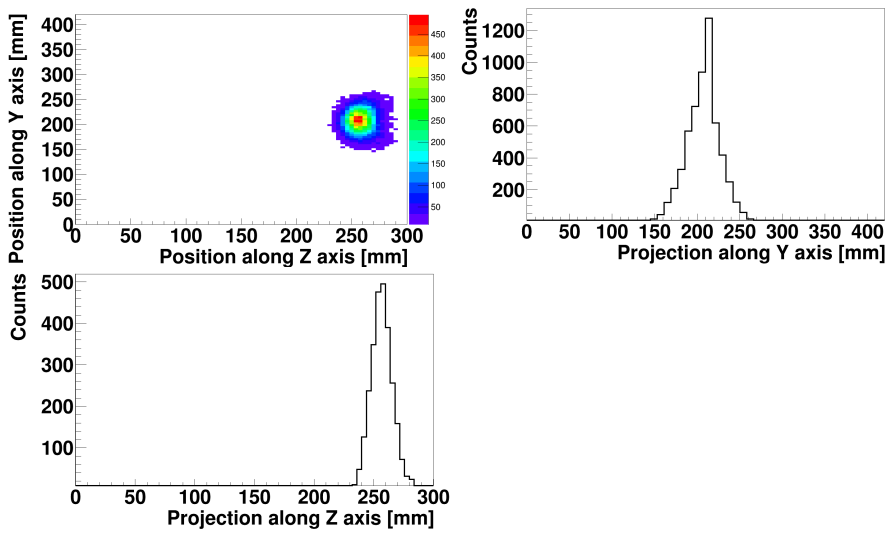

Figure 69: Raw image for the source placed 10 cm next to the central position for two 5x19x300 mm^3 modules.

PET scanner characteristics such as spatial resolution and procedure to measure them, are precisely described by The National Electrical Manufacturers Association (NEMA), the association of electrical equipment and medical imaging manufacturers in the United States, which determines and publishes standards for medical diagnostic imaging equipment. One of its standards is NEMA-NU-2 [71], which pertains to PET devices. It comprehensively defines the char-

acteristics of PET scanners such as the spatial resolution and makes a comparison between different kind of scanners possible [49].

According to NEMA regulations [71] one should estimate the resolution for PET scanners by using the Point Spread Function (PSF). This function is estimated as the width at half of maximum, of a reconstructed point distribution, along each axis. Interpolation between the bins in such an estimator is done by fitting a line between bin centers.

Such an approach was applied to check the initial PSF of distributions from single sources. Plot points are calculated according to Eq. 52 and 53. Each pixel in the picture was set to 1 mm x 1 mm. In Figs. 68 and 69 example raw images are presented in the top left part along with the projections on the Y and Z axis presented for heighest pixel for the source placed at the center and 10 cm off the center, respectively. The PSF amounts to 1.72 cm and 3.16 cm for Z and Y axes respectively for a source placed in the center - (150, 200) mm and 2.00 cm and 3.53 cm for a source placed in position (250, 200) mm.

29

MLEM ALGORITHM

In the previous chapter the PSF was calculated based on the image reconstruced as the density distribution of annihilation points. The obtained resolution may be improved by using more advanced image reconstruction algorithms. Here a List-Mode MLEM approach will be presented. In MLEM algorithm, in each iteration, the source emission density is calculated for each pixel $l = (x, y)$ as [68]:

$$\rho(l)^{t+1} = \sum_{j=1}^{N} \frac{P(e_j|l)\rho(l)^{(t)}}{\sum_{i=1}^{M} P(e_j|i)s(i)\rho(i)^{(t)}} \tag{57}$$

where $P(e_j|i)$ is a probability that an emission event e_j originating from pixel i will be detected as e_j, $s(i)$ is the probability that an event from pixel i will be detected at all, $\rho(i)^{(t)}$ is the density of emission from the ith pixel in iteration t. The sum over j runs over all registered annihilations, and sum over i runs over all pixels. After each iteration, a new source emission density is obtained, which should maximize the likelihood of observing a given set of annihilations.

Calculating the probability of an event originating from pixel i is beyond the scope of this work. Details of its calculation are described in reference [6].

In Figs. 70 - 72 an example of image reconstruction for two sources with different placement is presented for a selected number of performed iterations. One can clearly see that the algorithm is reducing experimental smearing with each iteration.

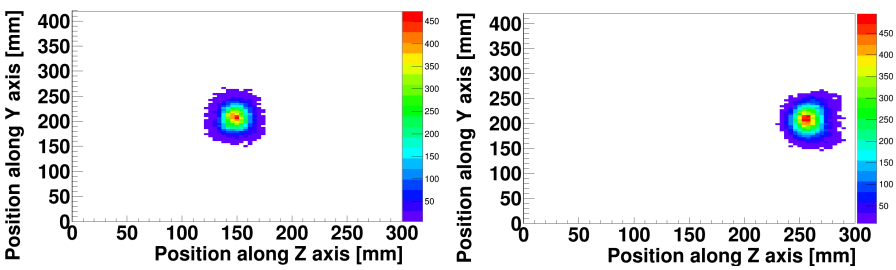

Figure 70: First iteration for a source in the center (left) and 10 cm next to the center (right.)

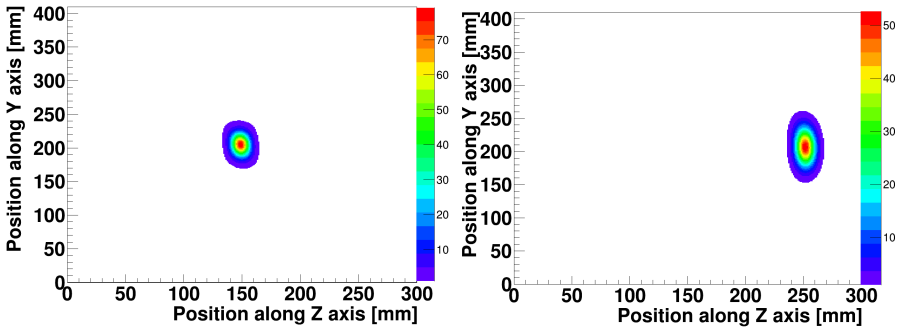

Figure 71: Tenth iteration for a source in the center (left) and 10 cm next to the center (right).

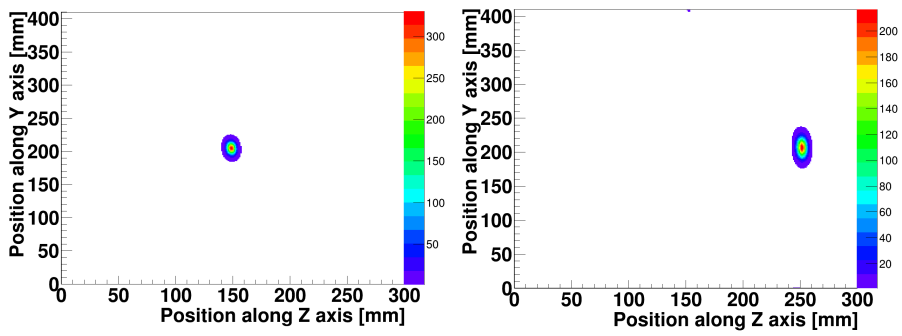

Figure 72: Fiftieth iteration for a source in the center (left) and 10 cm next to the center (right).

30

MLEM ITERATION STUDIES

In order to estimate the amount of iterations needed to be performed to saturate PSF values, for the case of point like sources, a scan of its values for two axes was performed. From Fig. 73 one can infer that after 100 iterations one does not observe any significant improvement. In Tab. 8 a comparison of PSF values for each axis is gathered after 10, 50, 100 and 200 iterations for each axis. As one can see within the first 20 iterations, the spatial resolution determined after reconstrution is improving very significantly for both axis. Note that the result asymptotically converges, but with an increasing number of iterations the amount of noise in the image is getting larger [68]. Note that the resolution along the Z axis is in general better than for the Y axis.

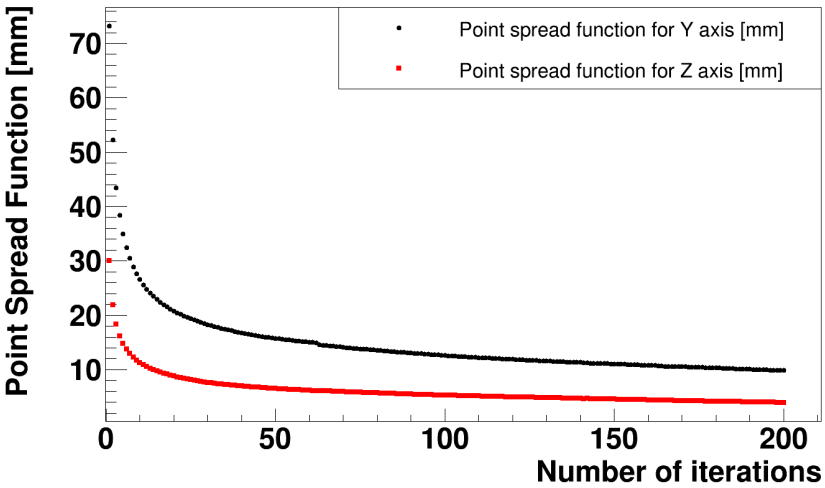

Figure 73: The PSF value as a function of the number of iterations for a 5x19x300 mm^3 module prototype. The source was placed at 1 cm off the center along the Z axis (Y = 200 mm , Z = 160 mm). The diameter of the active part of the source was around 3 mm. Results for the Y and Z axis are indicated with circles and squares, respectively.

Table 8: Point spread function values for the Y and Z axes for different number of iterations.

Number of iterations	PSF Y [mm]	PSF Z [mm]
10	27.4	11.3
50	15.7	6.5
100	12.6	5.3
200	9.8	3.9

In the next Chapters, when a comparison between results for different strip lengths and between other scanners will be made all J-PET PSF values will be extracted for 200 iterations.

Part IX

RESULTS FOR DIFFERENT SCINTILLATOR LENGTHS

Data originating from a few different lengths of scintillators (2 cm, 30 cm and 50 cm) were selected in order to study its influence on the energy and timing properties of the setup. For each data set following optimisation was performed:

- selection of optimal voltage - as in Chapter 22;
- selection of optimal threshold for time measurement as in Chapter 21;
- cut on deposited energy in the range 200 - 380 keV;
- time walk effect correction as in Chapter 26.1;

In case of 30 cm and 50 cm long strips a dependence of time and energy resolutions on position, was studied while for 2 cm long, only the central position was checked. Description of the experimental setup is gathered in Part iii. The method used for determination of energy resolution is presented in Chapter 15.

31

ENERGY RESOLUTION

The dependence of energy resolution on distance from the center of scintillator can be seen in Fig. 74. In case of both 30 cm and 50 cm long scintillators, energy resolution comes out to be about 9% at the Compton Edge for 511 keV gamma quanta. Additionally the energy resolution does not depend strongly on the position of irradiation, since the summed amount of light collected at both ends of the strip is nearly constant along the scintillator, and so is its resolution. On the borders of the 30 cm long scintillator a slight worsening can be observed, which is presumably caused by scattering of gamma quanta on the metal housing of photomultipliers.

In Tab. 9 the energy resolution for scintillators with different lengths is presented. The difference in energy resolution between 2 cm and 50 cm long scintillator differs only by a few percent.

Table 9: Energy resolution for scintillators with different lengths. Note that cross sections of 30 cm and 50 cm long strips are slightly different. Results are noted only for the central position of irradiation.

Strip dimensions [mm^3]	Energy resolution @ 340 keV
20 x 14 x 14	$7.2^{+0.7}_{-1.5}$
	$8.0^{+1.1}_{-1.2}$
300 x 5 x 19	$9.1^{+0.5}_{-0.3}$
	$9.0^{+0.4}_{-0.5}$
500 x 7 x 19	$9.3^{+0.4}_{-0.3}$
	$8.9^{+0.3}_{-0.3}$

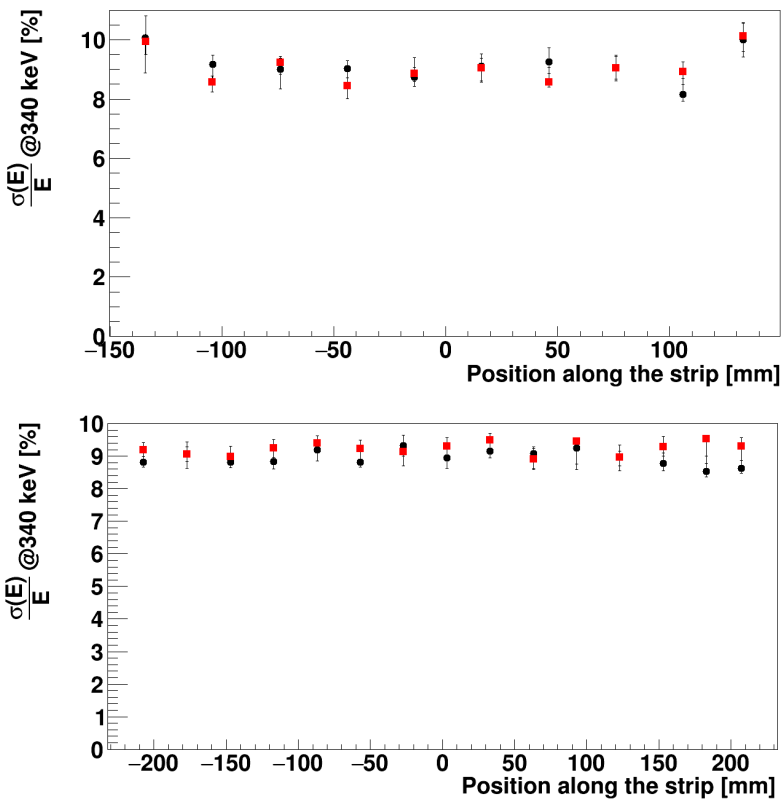

Figure 74: Energy resolution measured as a function of the distance from the center for 30 cm (top) and 50 cm (bottom) long scintillators. Square and circle points correspond to two tested scintillators.

32

COINCIDENCE RESOLVING TIME

The timing performance of the scanners is typically expressed by Coincidence Resolving Time (CRT) values. CRT is equal to the FWHM of the TOF resolution for a given scanner. CRT values along the scintillator strips are presented in Fig. 75. One can clearly see the worsening of CRT value when the distance from the center is rising. This effect is caused by attenuation of light in scintillator and resulting in smaller statistics of primary photo-electrons building each electric signal at one (more distant) photomultiplier.

The CRT value changes with the length of the scintillator. For 30 cm it is possible to achieve a resolution of about 300 ps at the center, for 50 cm only 350 ps resolution was obtained. In both cases, for the 30 cm and the 50 cm long strip, the CRT is not changing significantly when the interaction occurs at distance smaller than around 15 cm from the center of scintillator. The exact results for the central position for a few scintillator lengths are gathered in Tab. 10.

Table 10: CRT for different lengths of scintillators. Note that cross sections of 30 cm and 50 cm long strips are slightly different. Results are noted only for the central position of irradiation.

Strip dimensions [mm^3]	CRT [ps]
20 x 14 x 14	123.9 ± 5.3
300 x 5 x 19	280.2 ± 5.4
500 x 7 x 19	349.4 ± 3.5

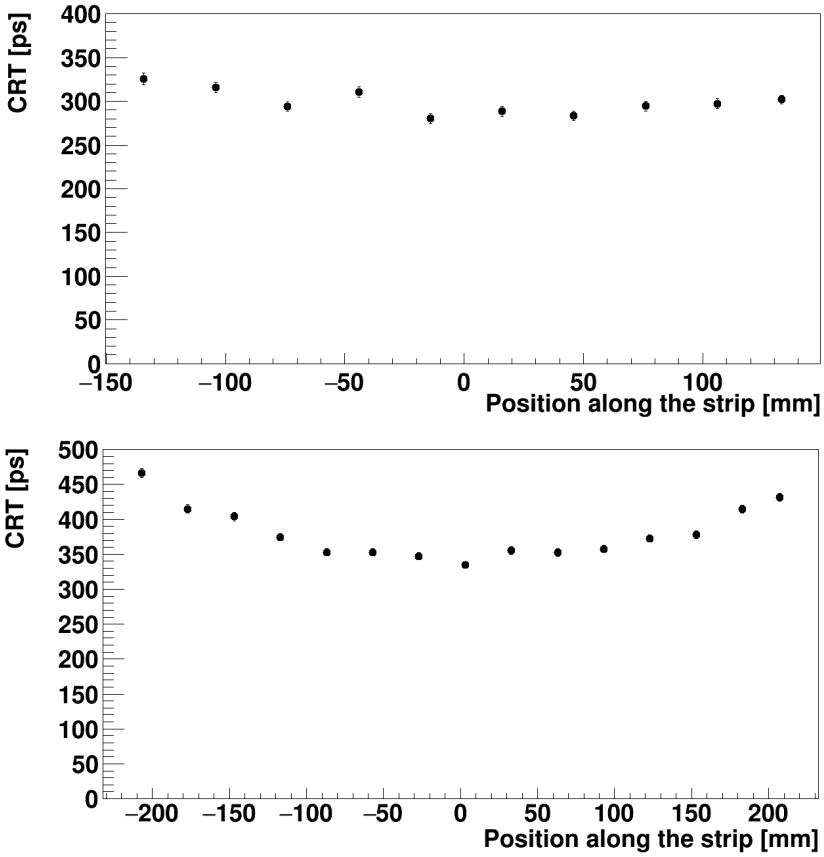

Figure 75: CRT measured as a function of the distance from the center for 30 cm (top) and 50 cm (bottom) long scintillators.

33

POINT SPREAD FUNCTION

In case of measurements performed for 30 cm long scintillators a single source was placed in 9 positions between the two modules (see Fig. 76). The Spatial resolution of a point source before and after reconstruction using the MLEM algorithm are presented in Tab. 11. The MLEM reconstruction is able to improve the initial results for raw images from about 30 mm to 10 mm on the Y axis and 15 mm to 6 mm on the Z axis. The resolution along the Z axis is better than for the Y roughly by a factor of two both when one compares the initial and reconstructed results. In case of both axes, the resolution is smaller than 1 cm.

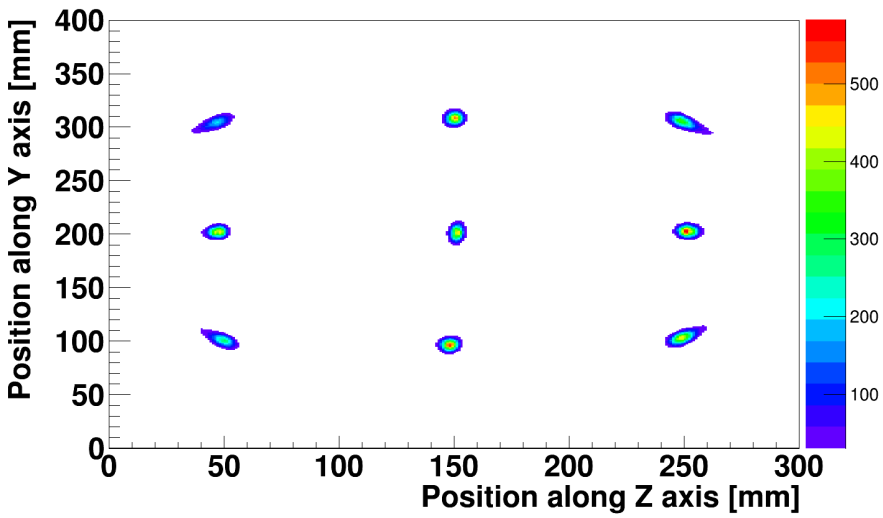

Figure 76: Image for the same source placed in 9 positions between the two modules after MLEM reconstruction using 200 iterations. Source positions are noted in Tab. 11.

Table 11: Point spread function values calculated for different source positions between the two detector modules. The table shows results for raw data (as presented in Chapter 28) and 200 iterations using the MLEM algorithm.

Position of source (Y,Z) [cm]	PSF Y [mm] (raw)	PSF Y [mm] (MLEM)
(0,1)	35	9.8
(10,0)	27	8.3
(-10,0)	37	8.9
(0,10)	34	7.8
(0,-10)	34	8.1
(10,10)	34	8.3
(10,-10)	32	8.4
(-10,10)	31	8.8
(-10,-10)	29	8.4
Position of source (Y,Z) [cm]	PSF Z [mm] (raw)	PSF Z [mm] (MLEM)
(0,1)	13.6	6.7
(10,0)	14.3	5.3
(-10,0)	12.0	5.3
(0,10)	15.3	6.2
(0,-10)	15.2	6.5
(10,10)	19.2	6.9
(10,-10)	14.9	6.7
(-10,10)	16.6	7.0
(-10, -10)	9.85	7.7

Part X

COMPARISON TO COMMERCIAL SCANNERS

A general comparison between commercial scanners and the J-PET prototype is presented in Tab. 12. One should note that the results for J-PET originate from the two module prototype, while the system composed of many modules should be in principle, more precise due to the geometrical influence of module positions on the reconstructed image. Hence in case of the system composed of only two modules reconstruction algorithm will produce worse results. This fact is visible when comapring transaxial resolutions. With the arrangement of scintillators in the cylinder as shown in Fig. 7, the uncertainty in the localization of the annihilation point in the transaxial direction will be largely reduced as one will have more LOR lines measured by many independent pairs of scintillators positioned at various Y-positions. The TOF resolution which is achieved with a two strip prototype is almost twice better than other scanners, which should improve signal to noise ratio [32]. For the full version of the J-PET scanner, based on SiPM and Wavelength Shifter [72] readout and 100 cm long scintillators, expected CRT is about 400 ps and the PSF along the Z and Y axis about 6 mm and 3 mm, respectively [49]. The AFOV of J-PET is about 1.5 times larger than in presented commercial scanners and can be easily enlarged in a cost effective way.

Table 12: Comparison of J-PET parameters with a few commercial scanners [24, 73, 74, 75]. The last column contains results from a 30 cm long two module prototype version of the J-PET scanner. Spatial resolution results are after 200 iterations using the dedicated MLEM algorithm.

Feature	Philips Ingenuity TF	GE Discovery 710	Siemens Biograph mCT Flow	J-PET
Detector material	LYSO	LYSO	LSO	BC420
Transaxial resolution				
at 1 cm (mm)	4.7	4.9	4.4	9.8
at 10 cm (mm)	5.2	5.5	4.9	7.8
Axial resolution				
at 1 cm (mm)	4.7	5.6	4.5	6.7
at 10 cm (mm)	5.2	6.3	5.9	6.2
TOF resolution (ps)	550	544	540	280
TOF localisation (cm)	8.9	8.2	8.1	4.2
Energy resolution FWHM (%)	12	12	NA	21
Energy window [kev]	460-665	425-650	435-650	200-380
AFOV (cm)	18	15.7	21.8	30

34

SUMMARY AND PERSPECTIVES

The aim of this work was to construct and perform tests of a PET scanner prototype consisting of two detection modules. Each module consisted of a long plastic scintillator strip and was readout from both sides by fast vacuum tube photomultipliers. Two dimensions of strips were tested: 5 x 19 x 300 mm^3 and 7 x 19 x 500 mm^3. It was shown, that one can successfully utilise plastic scintillators for 511 keV gamma quanta registration and the determination of the annihilation position of e^+e^- decay.

In the first part of the thesis, a description of the state of the art scanners was provided, as well as a comparison between plastic and crystal scintillators.

In second part the general concept of J-PET scanner was introduced, with a thorough explanation of how to determine the energy threshold for gamma quanta originating from the annihilation of e^+e^-. The energy deposition cut for gamma quanta on 200 keV is selected.

In the third part the experimental setup used for the test of the two module prototype was described: including the selection of scintillators, photomultipliers and radioactive sources used for tests. This part also contains the description of the collimator used to irradiate selected parts of the tested modules and oscilloscope for signal acquisition. R9800 hamamatsu photomutlipliers and EJ230 / BC420 scintillators are used to build the two strip prototype.

In the fourth part a low level data analysis performed on the acquisited signals was presented. It starts from determination of signal pedestal values, progresses to the determination of energy deposition inside scintillators by means of charge and TOT measurements.

The fifth part gives the answer to which kind of time measurement one can use in practise when faced with very fast rise times of signals produced by the detection module. The constant thresold time measurement is chosen and the final version of the board which uses LVDS buffers is selected.

The sixth part provides optimal values for the time measurement thresholds and the photomultipliers power supply.

The seventh part describes time calibration procedures and explores the possibility to use TOT as a tool to perform walk corrections instead of charge.

In the eight part an image reconstricton based on MLEM algorithm was studied. First the effective velocity was determined for an optimal threshold, then raw images and amount of MLEM iterations for the reconstruction was determined.

In two last parts a comparison of energy, time and spatial resolutions was performed first for different length of modules and then between a J-PET based on 30 cm long scintillators and three other state of the art scanners. The energy resolution and CRT are increasing with an increase of module length, which is to be expected since amount of light reaching the end of scintillators is decreasing for longer modules. The energy resolution for 30 cm is determined as about 9% at 340 keV - which is equal to the Compton edge for 511 keV gamma quanta. The CRT is determined as 280 ps and the PSF at 1 cm off the center of the tested prototype was equal to 9.8 mm and 6.7 mm for transaxial and axial resolutions, respectively.

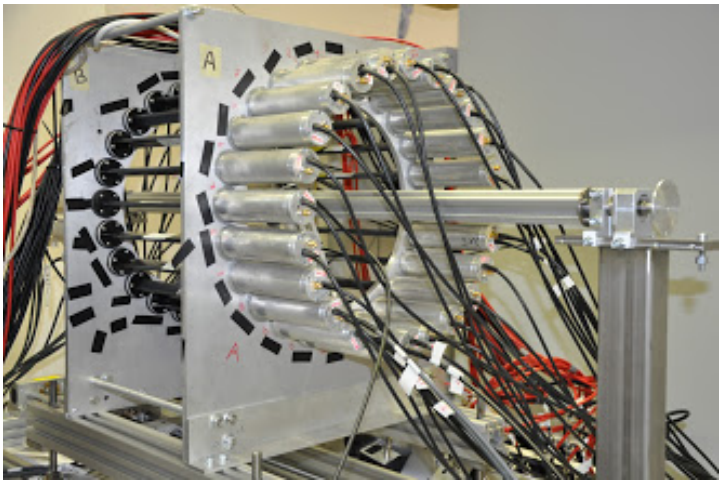

Figure 77: Small prototype composed of 24 detection modules. Each module consists of 30 cm long scintillators and two fast photomultipliers.

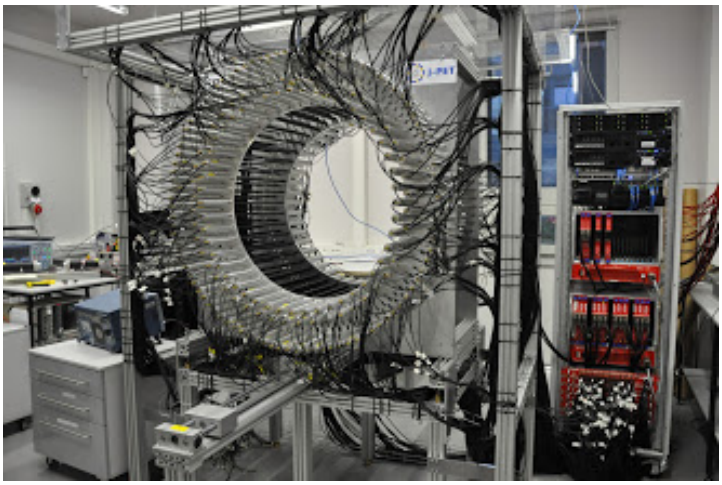

Figure 78: Full body prototype composed of 192 detection modules. Each module consists of 50 cm long scintillators and two fast photomultipliers.

The results of this thesis were also used to determine the front-end read-out board type for small and full body versions of J-PET detector (see Fig. 77 and 78). The author of this thesis was taking part in costruction of the total-body prototype from the stage of mechanical assembly to the assistance in performing measurements similiar to the ones described in the thesis. The total-body prototype consists of 192 detection modules, with the same dimensions as 50 cm long scintillators investigated in this thesis. Six experimental data taking runs were performed on the prototype which provided results not only connected to the PET tomography [76] but also to the fundamental physics studies such as the positronium life-time [10, 77], the discrete symmetries breaking [78, 79] and the polarization of photons [80, 81]. Moreover a possibility of performing a real-time data processing using FPGA based readout is currently investigated [19]. The results achieved with total-body prototype provide very good PSF for transaxial axis ($\sim$4 mm [76]), but the axial resolution still needs improvement (as at the moment of finalizing this thesis it is in the order of 1 cm).

To improve axial resolution, as a first step an exchange of vacuum tube photomultipliers to SiPM will be done, which should improve CRT of the scanner [45]. The construction of next version of the prototype based on SiPM readout is under construction at the time of finalising the thesis - see Fig. 79.

After testing new type of readout, as a second stage of improvement of axial resolution, application of WLS and plastic scintillator readout are intended based on the initial studies described in [72].

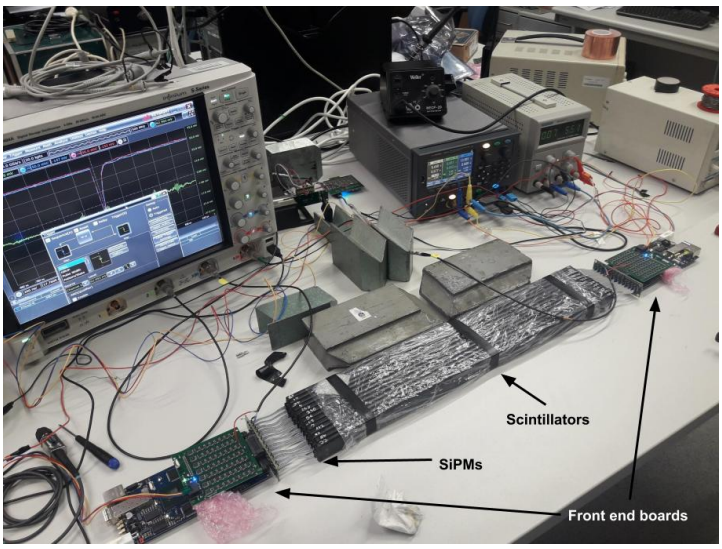

Figure 79: Photo of thirteen 50 cm long scintillators read out by four SiPM from both sides.

BIBLIOGRAPHY

[1] Ter-Pogossian M. M. et al. A positron-emission transaxial tomograph for nuclear imaging (pett). *Radiology*, 114:89–98, January 1975.

[2] Phelps M. E. et al. Application of annihilation coincidence detection to transaxial reconstruction tomography. *Journal of Nuclear Medicine*, 16(3):210–224, March 1975.

[3] Olesen O. V. et al. Spatial resolution of the hrrt pet scanner using 3d-osem psf reconstruction. *IEEE Nuclear Science Symposium Conference Record*, pages 3789–3790, 2009.

[4] Karp J. S. et al. Benefit of time-of-flight in pet: Experimental and clinical results. *The Journal of Nuclear Medicine*, 49(3):462–470, March 2008.

[5] Parra L. et al. List-mode likelihood: Em algorithm and image quality estimation demonstrated on 2-d pet. *IEEE Transactions on Medical Imaging*, 17(2):228–235, April 1998.

[6] Białas P. ... and Niedźwiecki Sz. et. al. List-mode reconstruction in 2d strip pet. *Bio-Algorithms and Med-Systems*, 10:9–12, 2014.

[7] Niknejad T. et al. Validation of a highly integrated sipm readout system with a tof-pet demonstrator. *Journal of Instrumentation*, 11:P12003, December 2016.

[8] Pałka M., ..., and Niedźwiecki Sz. et al. Multichannel fpga based mvt system for high precision time (20 ps rms) and charge measurement. *Journal of Instrumentation*, 12:P08001, August 2017.

[9] Alva-Sánchez H. et al. Positron range in tissue-equivalent materials: experimental micropet studies. *Physics in Medicine & Biology*, 61:6307–6321, August 2016.

[10] Moskal P., ..., and Niedźwiecki Sz. et al. Feasibility study of the positronium imaging with the j-pet tomograph. *ArXiv e-prints:1805.11696*, May 2019. In print, Physics in Medicine & Biology 2019.

[11] Weber W.A. Use of pet for monitoring cancer therapy and for predicting outcome. *Journal of Nuclear Medicine*, 46:983–995, June 2005.

[12] Cherry S. R. et al. Total-body pet: Maximizing sensitivity to create new opportunities for clinical research and patient care. *Journal of Nuclear Medicine*, 59:3–12, January 2018.

[13] Cherry S. R. et al. Total-body imaging: Transforming the role of positron emission tomography. *Science Translational Medicine*, 9, March 2017.

[14] Blanco A. et al. Rpc-pet: A new very high resolution pet technology. *IEEE Transactions on Nuclear Science*, 53:2489–2494, October 2006.

[15] Sun L. et al. A positron emission mammography system based on 4 mm straw detectors. *IEEE Nuclear Science Symposium Conference Record*, 5:3337–3344, January 2007.

[16] Shehad N. N. et al. Novel lead-walled straw pet detector for specialized imaging applications. *IEEE Nuclear Science Symposium Conference Record*, 5:2895–2898, February 2005.

[17] Moskal P. Strip device and the method for the determination of the place and response time of the gamma quanta and the application of the device for the positron emission thomography, patents: P 388 555 [wipo st 10/c pl388555], pct/pl2010/00062, wo2011008119, us2012112079, pl388555, jp2012533734, ep2454612, 2009/2010.

[18] Krzemień W., ..., and Niedźwiecki Sz. et al. Analysis framework for the j-pet scanner. *Acta Physica Polonica B*, 127(5):1491–1494, 2015.

[19] Korcyl. G, ..., and Niedźwiecki Sz. et al. Evaluation of single-chip, real-time tomographic data processing on fpga - soc devices. *IEEE Transactions on Medical Imaging*, 37(11):2526–2535, May 2018.

[20] Delbeke D. Oncological applications of fdg pet imaging: Brain tumors, colorectal cancer lymphoma and melanoma. *Journal of Nuclear Medicine*, 40:591–603, April 1999.

[21] Papathanassiou D. et al. Positron emission tomography in oncology: Present and future of pet and pet/ct. *Critical Reviews in Oncology/Hematology*, 72:239–254, 2009.

[22] P. Sharma et al. Newer positron emission tomography radiopharmaceuticals for radiotherapy planning: an overview. *Annals of Translational Medicine*, 4(3):53, December 2016.

[23] Saha G. B. *Basics of PET imaging*. Springer, 2 edition, 2010.

[24] Slomka P. J. et al. Recent advances and future progress in pet instrumentation. *Seminars in Nuclear Medicine*, 46:5–19, January 2016.

[25] Vandenberghe S. et al. Recent developments in time-of-flight pet. *European Journal of Nuclear Medicine and Molecular Imaging Physics*, 3:3, February 2016.

[26] *Lanthanum Bromide properties*. `https://www.crystals.saint-gobain.com/products/standard-and-enhanced-lanthanum-bromide`.

[27] *Saint Gobain plastic scintillators data sheet*. `https://www.crystals.saint-gobain.com/sites/imdf.crystals.com/files/documents/bc400-404-408-412-416-data-sheet.pdf` `https://www.crystals.saint-gobain.com/sites/imdf.crystals.com/files/documents/bc418-420-422-data-sheet.pdf`.

[28] Van Dam H. T. et al. Optical absorption length, scattering length, and refractive index of labr3:ce3+. *IEEE Transactions on Nuclear Science*, 59(3):656–664, June 2012.

[29] Schaart D. R. et al. Labr3:ce and sipms for time-of-flight pet: Achieving 100 ps coincidence resolving time. *Physics in medicine and biology*, 55:N179–89, 04 2010.

[30] Brahme A. and Budinger T. F. *Comprehensive Biomedical Physics*, volume 1. Elsevier, 2014.

[31] Phelps M. E. *PET: Physics, Instrumentation, and Scanners*. Springer, 2006.

[32] Surti S. Update on time-of-flight pet imaging. *Journal of Nuclear Medicine*, 56(1):98–105, January 2015.

[33] Conti M. State of the art and challenges of time-of-flight pet. *Physica Medica*, 25:1–11, December 2009.

[34] Bednarski T. *Kalibracja energetyczna i synchronizacja czasowa modularnego scyntylacyjnego systemu detekcyjnego do tomografii TOF-PET*. PhD thesis, 2016.

[35] Wieczorek A. *Development of novel plastic scintillators based on polyvinyltoluene for the hybrid J-PET/MR tomograph*. PhD thesis, 2017.

[36] R. Mao et al. Optical and scintillation properties of inorganic scintillators in high energy physics. *IEEE Transactions on Nuclear Science*, 55(4):2425–2431, Aug 2008.

[37] *Scintillation Detectors*. `https://www.ge.infn.it/~batta/Lect1-scint.pdf`.

[38] Niedzwiecki Sz. et al. J-pet: A new technology for the whole-body pet imaging. *Acta Physica Polonica B*, 48(10):1567–1576, October 2017.

[39] Schaart D. R. et al. $Labr_3$:ce and sipms for time-of-flight pet: achieving 100 ps coincidence resolving time". *Physics in Medicine & Biology*, 55:N178–89, April 2010.

[40] Brauksiepe S. et al. Cosy-11, an internal experimental facility for threshold measurements. *Nuclear Instruments and Methods in Physics Research A*, 376:397–410, July 1996.

[41] Moskal P., ..., and Niedźwiecki Sz. et al. Strip-pet: a novel detector concept for the tof-pet scanner. *Nuclear Medicine Review*, 15, Supplement C:C68–C69, 2012.

[42] Raczyński L., ..., and Niedźwiecki Sz. et al. Compressive sensing of signals generated in plastic scintillators in a novel j-pet instrument. *Nuclear Instruments and Methods in Physics Research A*, 786:105–112, June 2015.

[43] Raczyński L., ..., and Niedźwiecki Sz. et al. Calculation of the time resolution of the j-pet tomograph using kernel density estimation. *Physics in Medicine & Biology*, 62:5076–5097, May 2017.

[44] Białas P., ..., and Niedźwiecki Sz. et al. Gpu accelerated image reconstruction in a two-strip j-pet tomograph. *Acta Physica Polonica A*, 127:1500–1504, September 2015.

[45] Moskal P., ..., and Niedźwiecki Sz. et. al. Time resolution of the plastic scintillator strips with matrix photomultiplier readout for j-pet tomograph. *Physics in Medicine & Biology*, 61:2025–2047, February 2016.

[46] Klein O. and Nishina Y. Über die streuung von strahlung durch freie elektronen nach der neuen relativistischen quantendynamik von dirac. *Zeitschrift für Physik*, 52:853–868, November 1929.

[47] Teras M. et al. Performance of the new generation of whole-body pet/ct scanners: Discovery ste and discovery vct. *European Journal of Nuclear Medicine and Molecular Imaging*, 34:1683–1692, 2007.

[48] Reynés-Llompart G. et al. Performance characteristics of the whole-body discovery iq pet/ct system. *Journal of Nuclear Medicine*, 58:1155–1161, 2017.

[49] Kowalski P., ..., and Niedźwiecki Sz. et al. Estimating the nema characteristics of the j-pet tomograph using the gate package. *Physics in Medicine & Biology*, 63:165008, August 2018.

[50] Tarantola G. et al. Pet instrumentation and reconstruction algorithms in whole-body applications. *Journal of Nuclear Medicine*, 44:756–769, April 2003.

[51] Eijk C. W. E. Inorganic scintillators in medical imaging. *Physics in Medicine and Biology*, 47:R85–R106, April 2002.

[52] Moskal P. and Niedźwiecki Sz. et. al. Test of a single module of the j-pet scanner based on plastic scintillators. *Nuclear Instruments and Methods in Physics Research A*, 764:317–321, November 2014.

[53] *SDA 6000A datasheet*. `https://www.testequipmentconnection.com/36780/Teledyne_LeCroy_SDA_6000A.php`.

[54] Strzałkowski A. *Wstęp do Fizyki Jądra Atomowego*. Państwowe Wydawnictwo Naukowe, 1969.

[55] *Eljen plastic scintillators data sheet*. `https://eljentechnology.com/images/products/data_sheets/EJ-228_EJ-230.pdf`.

[56] *Vikuiti ESR data sheet*. `https://www.digikey.com/en/pdf/3/3m/3m-vikuiti-enhanced-specular-reflector-esr`.

[57] *Kapton 100B data sheet*. `http://www.dupont.com/content/dam/dupont/products-and-services/membranes-and-films/polyimde-films/documents/DEC-Kapton-B-datasheet.pdf`.

[58] *R4998 and R9800 data sheet*. `https://www.hamamatsu.com/resources/pdf/etd/High_energy_PMT_TPMZ0003E.pdf`.

[59] Kubicz E., ..., and Niedźwiecki Sz. et al. Beam profile investigation of the new collimator system for the j-pet detector. *Acta Physica Polonica B*, 47(2):537–548, February 2016.

[60] Niedźwiecki Sz. *Studies of detection of gamma radiation with use of organic scintillator detectors in view of positron emission tomography*. Master thesis, 2011.

[61] Eadie W.T., Drijard D., James F.E., Roos M., and Sadoulet B. *Statistical Methods in Experimental Physics*. North-Holland, 1971.

[62] James F. Interpretation of the shape of the likelihood function around its minimum. *Computer Physics Communications*, 20:29–35, September 1980.

[63] Wu Jin-Jie and et al. A study of time over threshold (tot) technique for plastic scintillator counter. *Chinese Physics C*, 32:186–190, March 2008.

[64] Traxler M. et al. A compact system for high precision time measurements (< 14 ps rms) and integrated data acquisition for a large number of channels. *Journal of Instrumentation*, 6:C12004, December 2011.

[65] Neiser A. et al. Trb3: a 264 channel high precision tdc platform and its applications. *Journal of Instrumentation*, 8:C12043, December 2013.

[66] Pałka M., ..., and Niedźwiecki Sz. et al. A novel method based solely on fpga units enabling measurement of time and charge of analog signals in positron emission tomography. *Bio-Algorithms and Med-Systems*, 10:41–45, 2014.

[67] Moskal P. *Response function of the trigger scintillation detector for the COSY-11 installation*. Master thesis, 1993.

[68] Strzelecki A. *Image reconstruction and simulation of strip Positron Emission Tomography scanner using computational accelerators*. 2016.

[69] Matej S. et al. Evaluation of task-oriented performance of severalfully 3d pet reconstruction algorithms. *Physics in Medicine and Biology*, 39:355, October 1993.

[70] Qi J et al. Iterative reconstruction techniques in emission computed tomography. *Physics in Medicine and Biology*, 51:R541–78, August 2006.

[71] National Electrical Manufacturers Association. *NEMA NU 2-2012, Performance Measurements of Positron Emission Tomographs*.

[72] Smyrski J, ..., and Niedźwiecki Sz. et al. Measurement of gamma quantum interaction point in plastic scintillator with wls strips. *Nuclear Instruments and Methods in Physics Research A*, 851:39–42, April 2017.

[73] Zaidi H. et al. Design and performance evaluation of a whole-body ingenuity tf pet–mri system. *Physics in Medicine & Biology*, 56:3091–3106, April 2011.

[74] Bettinardi V. et al. Physical performance of the new hybrid pet=ct discovery-690. *Medical Physics*, 38(10):5394–5411, October 2011.

[75] Rausch I. et al. Performance evaluation of the biograph mct flow pet/ct system according to the nema nu2-2012 standard. *European Journal of Nuclear Medicine and Molecular Imaging*, 2(26), December 2015.

[76] Pawlik-Niedźwiecka M., ..., and Niedźwiecki Sz. et al. Preliminary studies of j-pet detector spatial resolution. *Acta Physica Polonica A*, 132(5):1645–1648, 2017.

[77] Dulski K., ..., and Niedźwiecki Sz. et al. Commissioning of the j-pet detector in view of the positron annihilation lifetime spectroscopy. *Hyperfine Interactions*, 239(1):40, Sep 2018.

[78] Moskal P., ..., and Niedźwiecki Sz. et al. Potential of the j-pet detector for studies of discrete symmetries in decays of positronium atom - a purely leptonic system. *Acta Physica Polonica B*, 47(2):509–535, 2016.

[79] Czerwiński E., ..., and Niedźwiecki Sz. et al. Studies of discrete symmetries in decays of positronium atoms. *European Physical Journal Web of Conferences*, 181, 2018.

[80] Moskal P., ..., and Niedźwiecki Sz. et al. Feasibility studies of the polarization of photons beyond the optical wavelength regime with the j-pet detector. *European Physical Journal C*, 78(11), November 2018.

[81] Mohammed M., ..., and Niedźwiecki Sz. et al. A method to produce linearly polarized positrons and positronium atoms with the j-pet detector. *Acta Physica Polonica A*, 132(5):1486–1489, 2017.